

ACOUSTICAL WAVE-PHENOMENA: ENHANCED
TRANSMISSION, GUIDING, ATTENUATION AND
FOCUSING

Johan Christensen, BSc, MSc

A DISSERTATION

Submitted to the

Universidad Autonoma de Madrid
Departamento de Fisica Teorica de la Materia Condensada

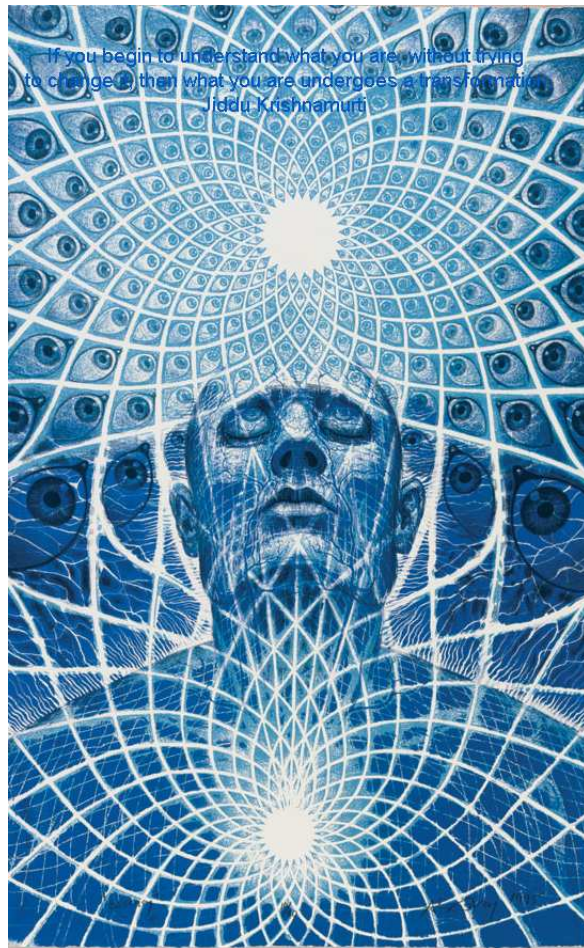
1st April, 2010

Supervisor of Dissertation, Prof. F. J. Garcia-Vidal

Long live the King!



In dedication to Ani.
So, Ani are you ok?



Acknowledgements

I am grateful to my supervisor Francisco J. Garcia-Vidal for having been his student and for his support in the physical and mathematical development of our work. In that respect I would also like to express my gratitude to the Nanophotonics group at UAM, who always had a door open for discussions and helping me. Without the help from Juan Antonio and Antonio I would have drowned in Spanish paper work. Francisco also taught me things that went beyond the scope of modelling: writing articles, cooperating with others, presenting a good talk, etc. I specially thank him for the freedom for self-consistent work. Maybe it was also a consequence of doing acoustics in a nanophotonics group.

Furthermore, the interest and support from leaders on physical acoustics around the world has been a strong motivation: Nico F. Declercq, Jensen Li (shouldn't it be Li Jensen I always wonder...), Xiang Zhang and John H. Page. Financial support from a Marie-Curie EDSVS fellowship (though for 2006 in Berlin, which motivated me to continue on acoustics), Plasmo-Nano-Devices, an assistant professorship at the department of theoretical physics of condensed matter, UAM and the Carlsberg Foundation (during the last writing up) is acknowledged.

ABSTRACT

ACOUSTICAL WAVE-PHENOMENA: ENHANCED TRANSMISSION, GUIDING, ATTENUATION AND FOCUSING

Supervisor: Prof. F. J. Garcia-Vidal

English

This thesis deals with a theoretical study on the interaction of air-borne sound with metallic structures. The discovery of the phenomenon of extraordinary optical transmission through a two-dimensional array of subwavelength holes in a metallic film has opened a new line of research within optics, whereupon the acoustical analogy is being employed from first principles. The structures under study are described and modelled by means of a mode matching technique, and assumed to fulfil a perfect rigid body approximation, which is a valid approach for steel or brass plates under acoustic load. In this framework we present transmission analysis for various periodic and finite configurations that are in good agreement with experiments found in the literature. Guiding and focusing of sound with an axial guide is being taken under investigation: a sound-hard wire decorated with milled rings, is examined for its sound confining capabilities. It is shown how acoustic surface waves can be engineered with their propagation properties controlled entirely by geometrical means. These highly localized acoustic surface waves give rise to strong acoustical field confinement along the wire, and what is believed to be a promising feature of these low-loss propagation properties, is the ability to tune sensing and screening applications with good transducer coupling.

Metamaterials are functional composites, gaining their wave properties from geometrical parameters. The theoretical formalism developed has been employed to address the capability of a holey metamaterial to act as a high resolution imaging

device for sub-diffraction limited objects, applicable for medical and industrial ultrasound instruments. An effective medium approach such as a full modal expansion, predict imaging for complex objects 50 times smaller than the operating wavelength, that additionally has been observed by means of measurements. Sound attenuation for noise free environments has been developed by a double-fishnet structure. This structure which consist of two adjacent holey plates, has been described by a modified single plate formalism, in which a negative effective bulk modulus is found. This resonance which can be tailored by, e.g., the plate separation exhibits broadband sound blockage with weak dispersion.

Español

Esta disertación doctoral aborda un estudio teórico sobre la interacción del sonido con estructuras metálicas. El descubrimiento de la transmisión extraordinaria de luz a través de un array bidimensional de agujeros con dimensiones inferiores a la longitud de onda en una lámina metálica inició una nueva línea de investigación en óptica, la cual se extendió desde el principio a fenómenos acústicos. Las estructuras estudiadas son descritas y modeladas mediante la técnica de expansión modal con la aproximación de un cuerpo rígido perfecto, aproximación que es válida para acero o plata en interacción con ondas acústicas. En este orden de ideas se presenta un análisis de transmisión para diferentes configuraciones de estructuras periódicas finitas que está en buena correlación con los resultados experimentales encontrados en la literatura. El guiado y enfoque de sonido con una guía axial es objeto de investigación: una guía o alambre rígido estructurado con anillos son estudiados para conocer su capacidad de confinamiento del sonido. Se muestra como ondas acústicas superficiales con sus propiedades de propagación pueden ser controladas por los parámetros geométricos del medio. La alta localizabilidad de las ondas acústicas superficiales permiten un gran incremento del confinamiento del campo acústico a lo largo del alambre. Esta promete ser una característica de baja pérdida en las propiedades de transmisión y ofrece la posibilidad de ajustar las aplicaciones de detección y selección con un buen acoplamiento.

Los metamateriales son estructuras funcionales que permiten optimizar las propiedades ondulatorias a partir del ajuste de los parámetros geométricos del sistema. El formalismo teórico desarrollado ha sido usado en el estudio de la capacidad de un metamaterial agujereado para actuar como un dispositivo de alta resolución de obtención de imágenes de objetos limitados por difracción. Un medio efectivo aproximado por la técnica de expansión modal predice imágenes para objetos de formas complejas de tamaños 50 veces más pequeños que la longitud de onda utilizada, que adicionalmente, se ha observado por medio de mediciones experimentales. La

atenuación de sonido para espacios libres de ruido ha sido desarrollada por una estructura double-fishnet. Esta estructura que consiste de dos láminas agujereadas adyacentes ha sido descrita modificando el formalismo para una sola lámina, en la cual un módulo de compresibilidad negativo efectivo es encontrado. Esta resonancia, la cual puede ser modificada por, un ejemplo: la separación de las placas, produce bloqueo de sonido por ensanchamiento de banda con una dispersión débil.

List of acronyms

This is a list of the acronyms used in the text:

- **ADF** Acoustic double-fishnet
- **ASW** Acoustic surface wave
- **DNG** Double negative
- **EAT** Extraordinary acoustical transmission
- **EM** Electromagnetic
- **EMA** Effective medium approach
- **ENG** Epsilon negative
- **EOT** Extraordinary optical transmission
- **FP** Fabry-Perot
- **FEM** Finite element method
- **KHz** kilohertz
- **LHM** Left-handed material
- **LPM** Lumped parameter model
- **MHz** Megahertz
- **ME** Modal expansion
- **MNG** Mu negative
- **PEC** Perfect electric conducting

- **PRB** Perfect rigid body
- **SNG** Single negative
- **SRR** Split-ring resonator
- **SPPs** Surface plasmon polaritons
- **TE** Transverse electric
- **TM** Transverse magnetic
- **THz** Terahertz
- **UV** Ultraviolet

Contents

1	Introduction	1
1.1	Background	2
1.2	Motivation	11
1.3	Problem Statements	12
2	Enhanced acoustical transmission and basics	16
2.1	Air-borne sound	17
2.2	Structure-borne sound	18
2.3	Mode matching technique	19
2.4	Transmission through a single slit	27
2.5	Transmission through a single hole	33
2.6	Transmission through a slit array	36
2.7	Transmission through a hole array	45
2.8	Transmission through a single slit surrounded by corrugations	55
2.9	Direct comparison to the optical counterpart	65
2.10	Summary and future work	66
3	Confining acoustic surface waves along a wire	68
3.1	Theoretical description of a corrugated metawire	69
3.2	Geometrically tunable surface states	75
3.3	Applying the slowing effect for superfocusing sound	78

3.4	Confining light along a corrugated perfect conducting wire	80
3.5	Conclusion and further directions	82
4	A holey structured metamaterial for acoustic deep subwavelength imaging	83
4.1	Theoretical development	84
4.2	Subwavelength imaging by means of a slit array and a hole array . . .	91
4.3	Experimental verification	98
4.4	Summary and outlook	103
5	Broadband all-angle blockage of sound by a double-fishnet structure	105
5.1	Modal expanding the acoustic double-fishnet structure	107
5.2	Transmission study	111
5.3	Negative effective bulk modulus and its angular sensitivity	115
5.4	Fano resonance interpretation	120
5.5	Conclusion and future work	122
6	Conclusion	124
6.1	Summary	124
6.2	List of Publications	130
A		131
A.1	Overlap functions for a slit array	131
A.2	Overlap functions for a hole array	132
A.3	Overlap and Greens functions for isolated apertures containing inden- tations	132
A.4	Expansion coefficients	133
B		134

B.1	Transmission coefficient for a holey metamaterial	134
-----	-------------------------------------------------------------	-----

List of Figures

1.1	Lycurgus Cup from the British Museum	4
1.2	Transmission spectra together with SEM image	5
1.3	Planar THz metamaterial creating artificial magnetism	8
1.4	Unit cell and crystal of rubber coated metal spheres	10
1.5	Growth comparison between plasmonics and acoustics based on surface phenomena	12
2.1	Periodic array of slits	19
2.2	Sketch of a single slit	28
2.3	Transmittance spectrum for a single slit and the locations of the non-trivial solutions.	29
2.4	Transmittance spectra for single slits of three different geometries. . .	31
2.5	Modulus of the complex pressure field plotted for a single isolated slit.	32
2.6	Sketch of a single isolated hole	33
2.7	Transmittance spectrum for a single hole and the locations of the non-trivial solutions.	35
2.8	Transmittance spectra for single holes of three different geometries. .	36
2.9	Convergence study with a normalized-to-unit cell transmittance spectrum for a slit array	37
2.10	Convergence study with a dispersion relation plot for a groove grating	40
2.11	Normalized-to-unit-cell transmittance spectra as a function of the wave number and a dispersion relation of the acoustic guided modes.	43

2.12	Normalized-to-unit-cell transmittance spectra and the associated pressure fields in the unit-cell	45
2.13	Periodic array of holes	46
2.14	Convergence study of normalized-to-unit cell transmittance spectra for a hole array	50
2.15	Transmittance spectra for an array of holes and the locations of the non-trivial solutions.	51
2.16	Spectral transmittance contour for an array of holes as a function of the metal thickness	52
2.17	Pressure field maps for a hole array	53
2.18	Sketch of a single slit surrounded by corrugations	55
2.19	Normalized-to-area transmittance contour for the optimization of a single single slit surrounded by corrugations	59
2.20	Influence on the transmittance spectra dependent on the location and numbers of surface corrugations	61
2.21	Near-field pressure on a plate with a single slit surrounded by corrugations	62
2.22	Far-field representation of sound funnelled through slit flanked by corrugations	63
2.23	Off-axis pressure field mapping of sound	64
2.24	Tabular representation of the similarities between EOT and EAT	66
3.1	Schematics of the metawire	70
3.2	Convergence study with a dispersion relation plot for a metawire	73
3.3	Dispersion relation of the metawire	75
3.4	Pressure field in the ring unit cell of the metawire	76
3.5	Pressure field of a truncated wire	77
3.6	Wave slowing for different depths	78
3.7	Cone pressure field	79

3.8	Spoof SPPs versus ASWs	81
4.1	Concept of negativity in acoustics	86
4.2	Periodic array of holes as a lens	88
4.3	Properties of the Fabry Perot resonance	90
4.4	Spatial image plot with the slit array metamaterial	92
4.5	Resolution limit of the acoustic metamaterial	94
4.6	Sound lensing by means of a hole array	96
4.7	Band diagram of the holey structure	97
4.8	Photo of the acoustic metamaterial	98
4.9	Experimental and theoretical results of two subwavelength dots . . .	100
4.10	Experimental and theoretical results of a subwavelength ($\lambda/37$) "E" .	101
4.11	Experimental and theoretical results of a subwavelength ($\lambda/50$) "E" .	102
4.12	Holey metamaterial and perfect lensing	104
5.1	Schematics of the acoustic fishnet structure	108
5.2	Spectral contour transmittance for varying metal thickness	112
5.3	Isolated gap mode solution	115
5.4	Effective bulk modulus for different geometries	117
5.5	Transmittance contour dispersion relation	118
5.6	Dispersion relation	119
5.7	Transmission spectra with determinant and Fano interpretation . . .	120

Chapter 1

Introduction

One might think about the fight between Goliath against David from the old testament, irrespective of the outcome of this battle, when comparing the size of the implication and impact, modern optical research compared to its acoustical counterpart has created. The modern optical fields in question are ranging from photonic crystals, nanoplasmonic devices and general metamaterials for exotic properties of light. To this, the study on physical acoustics, has always been the follower, striving to find novel analogies based on e.g. phononic crystals, subwavelength guides and locally resonant structures. One might ask, why there is such a huge gap in the interest between those fields, bearing in mind that Lord Rayleigh, who was interested in both acoustics and the study of light, published his first works on sound [1]. In the following we will try to answer this question, and also highlight the background and motivation regarding the study on novel acoustical wave phenomena, that has been the objective for this doctoral thesis.

1.1 Background

The field of acoustics is broadly subdivided into different branches, such as acoustical engineering (architectural, environmental, transduction, etc.), biological acoustics (speech communication, psychological acoustics and physiological acoustics) and physical acoustics. Physical acoustics also contains several subcategories such as aeroacoustics, nonlinear acoustics or under water sound, but the more fundamental aspects regarding quantum mechanical and optical analogies, is still a young member of the big acoustical family. Phononic crystals and locally resonant structures, which can exhibit novel effects like creating forbidden frequency regions of sound propagation or negative refraction, are fields devoted to the main objectives on physical acoustics inspired and motivated by optical analogies: sound focusing, imaging and shielding [2, 3]. Shielding sound is of paramount importance, when it comes to environmental design and architecture work for halls, offices, train stations and highways as disturbing ambient noise is wished to be kept at a minimum. This is where acousticians envision the importance of the role of periodic structures with huge attenuation bands. Acoustics in medicine, for the detection and imaging of early stage tumours by means of ultrasound scanning, is driving the research regarding the advantages and capabilities on focusing and negative refraction, associated to novel structure properties. HIFU (high intensity focused ultrasound) which is a high-intensity focused ultrasound medical device to heat and destroy pathogenic tissue rapidly, is another candidate which could obtain further improvements by, e.g., a quasi unlimited size of the sound spot, gained by the properties of an exotic material [4]. This could also easily be applied to ultrasound non-destructive testing applications, for powerplants and tanks in the search for fine material fatigue such as cracks [5, 6].

Nanophotonics today, is driven by enormous and rapid developments in telecommunication technology, computers and interconnects. A rather new, or correctly

said: renewed theme in the field of nonanophotonics, provides new challenges and possible routes to improve the named concepts and creating new novel material phenomena, *Surface Plasmon Nanophotonics*. Surface plasmon polaritons (SPPs) are of interest to a wide spectrum of scientists, ranging from physicists, chemists and materials scientists to biologists. A renewed interest into this field stems from recent advances, which allow metals to be structured and characterized on the nanometer scale. It is so far believed that the study of SPPs has the potential to revolutionize the telecommunications industry by providing low-power, high-speed interference-free devices such as electro-optic and all-optical switches on a chip. Data storage, microscopy, solar cells and sensors for detecting biologically interesting molecules are just a few other concepts, acquiring advantages from the guiding and focusing schemes, associated to SPPs [7–9].

In the following we shall give a brief review on the fundamentals regarding SPPs and highlight two themes, which will be devoted to the acoustical analogy: Extraordinary optical transmission and guiding of SPPs. Surface plasmons, or generally speaking, surface electromagnetic (EM) waves were seriously taken under examination in 1899 by A. Sommerfeld who studied the problem of axial currents along a straight wire where the solutions of Maxwells equations decayed off with growing distance from the wire [10]. Only eight years later, theoretically the so-called Zenneck surface waves were discovered, after J. Zenneck, in connection with Marconi's trans-oceanic radio waves [11]. Localized SPPs are found on rough surfaces and engineered nanostructures as we will see below. Nano particles as one example, which can be embedded into glass have tunable plasmon resonances, determined by the shape and size. One famous example, is Lycurgus Cup as can be seen in Fig. 1.1. This ancient plasmonic structure supports the oscillation of free electrons in those metallic nanoparticles, embedded inside the glass of the structure. With the right shape and size of the metallic particles, the localized SPPs resonance determines the degree of the colouration of the cup [12]. In a less classical, but physically at least



Figure 1.1: Lycurgus Cup from the British Museum, which is made out of ruby glass. When views in e.g. daylight, it appears green, but when light is shone into the cup and transmitted through, it appears to be red.

equally important context, in 1902 Wood measured the appearance of "anomalous" intensity minima, when white light was shone on the surface of a groove grating, backed with a mirror [13]. Physical interpretation was initiated by Lord Rayleigh [14], and further refined by Fano [15], but based on work about the electron energy losses in thin metal film, in 1957 Ritchie showed that plasmon modes can exist near the surface of metals [16]. However, a complete explanation of the phenomenon regarding the light interaction with a groove grating, was given in 1968, when Otto [17] and in the same year Kretschmann and Raether [18] reported on the excitation of surface plasmons.

In 1989, almost a decade before publication, Ebbesen and coworkers discovered an extraordinary large optical transmission efficiency through a square periodic lattice of holes in a thin metallic film, see Fig. 1.2. The holes were much smaller than

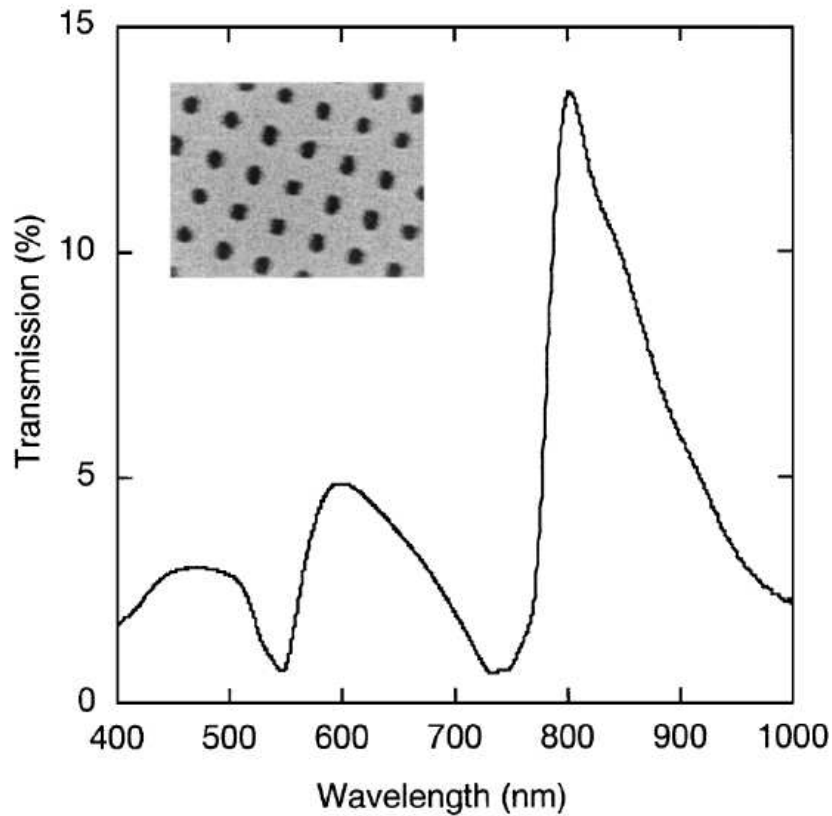


Figure 1.2: Experimental zero-order power transmittance, at normal incidence for a square array of holes in a freestanding Ag film. Taken from: L. Martin-Moreno et al. *Phys. Rev. Lett.*, **86**, 1114, 2001.

the wavelength of the incident light, though at certain wavelengths, the transmission could even exceed unity, when normalized to the geometrical fraction on the surface occupied by the holes [19]. According to classic diffraction theory [20, 21], the enhanced transparency, dubbed "extraordinary optical transmission" (EOT) would be of magnitudes higher as previously predicted. For one individual subwavelength hole in a screen of zero thickness, the transmission would rapidly drop off at a rate $(r/\lambda)^4$ above cutoff, but in the particular periodic configuration by Ebbesen, it was shown that this constraint was overcome, implying that even the light impinging on the metal between the holes would be transmitted through the film. Although there

has been a great deal of debate and controversy behind the mechanism of EOT, it is now widely accepted and supported by a wide variety of experimental observations and theoretical predictions, that a resonant excitation of SPPs on and through the structure, gives rise to the observation of enhanced transmission. In the process of exploring the actors, responsible for the EOT, a vast amount of work has been dedicated to understand this phenomena of light transmission through slit arrays, holey perfect electric conductors (PEC) and isolated apertures among others. For an extensive progress review, describing both theoretical and experimental aspects of this subject, one is to address the following report [22]. In particular, the discovery of EOT, spectrally below the optical regime at MHz and THz frequencies where bound surface modes in the form of plasmons only are located weak, led to the consideration of the sustainability of artificially SPPs in PEC materials [23–27]. By perforating the surface of a good conducting metal with an array of subwavelength holes, it is possible to produce a designer top-layer which effectively allows the field to penetrate by means of evanescent fields, associated with the lowest-order guided modes, below cutoff. This theoretical prediction was recently confirmed in the microwave regime, underlining the concept of designer or spoof SPPs [28, 29]. Moreover, spoof SPPs has been extended to other geometries such as a cylindrical structure, where it also was found that these artificially, man-made surface mode could be used to guide EM radiation, much in the same way as conventional SPPs [30]. To this theme, we can count plasmonic waveguides such as metallic strips [31], metal-insulator-metal guides [32], nanowires [33], nanoparticle arrays [34] such as channel and wedge guides[35, 36], all concepts driven by the goal to merge photonics and electronics at nanoscale dimensions [37]. For some of those structures, the term "plasmonic metamaterial" is considered, as they gain their properties from their topological buildup. E.g., the attributes of spoof SPPs such as the degree of field confinement is controlled by geometrical parameters, hence by texturing metallic systems, the properties are gained from the structure rather than their chemical

composition.

Tailoring man-made optical properties in order to obtain astonishing phenomena such as artificial magnetism, plasmas, backward travelling waves, negative refraction and perfect lensing, can all be summarized in the context of metamaterials. Here follows a brief review on this theme, because artificial man-made acoustical structures is another objective within this thesis. It is difficult, precisely to say, when those materials first saw the day of light. It is clear, that for example H. Lamb, firstly reported on vibrational motion in bars giving rise to displacements of negative group velocity [38]. A vast amount of papers from the Russian electrical engineering community, already in the middle of the last century, had the knowledge on the consequences regarding left-handed material (LHM) with both negative permittivity ε and permeability μ [39]. Victor Veselago, published in 1967 his seminal work on the hypothesis that a material with a negative refractive index could exist without violating any of the laws of physics. Veselago predicted that this remarkable material would exhibit a wide variety of new optical phenomena, from reversed geometrical optics to reversed Doppler shifts [40]. At that time, extensive studies were already in progress on artificial dielectrics regarding beam shaping elements in lens antenna applications [41]. Later Kock introduced several experimental models for artificial dielectric lenses, that constituted spherical arrays [42]. Cohn took this concept one step further by introducing a strip array as a delay medium, which could be described as transmission line low pass filters to control the refraction index [43, 44]. But the definite breakthrough came in 1962 by Rotman, who came up with the first prescription on tailoring an artificial plasmon, out of a so-called rodged media [45]. It was already known from a textbook in the 50's, that the split-ring could act as an artificial magnetic particle [46]. An extended version of this structure, came about the late 70's and early 80's in the form of a slotted tube resonator and a high Q resonator respectively [47, 48]. It was however in the late 90's, when Pendry revived

those electric and magnetic concepts from theoretical first principles [49, 50], Veselago's prediction became true by the experimental verification on negative refraction measured by Smith et al. This milestone discovery was the birth of left-handed materials (LHMs) at the beginning of the new century [51, 52]. Those LHMs were a

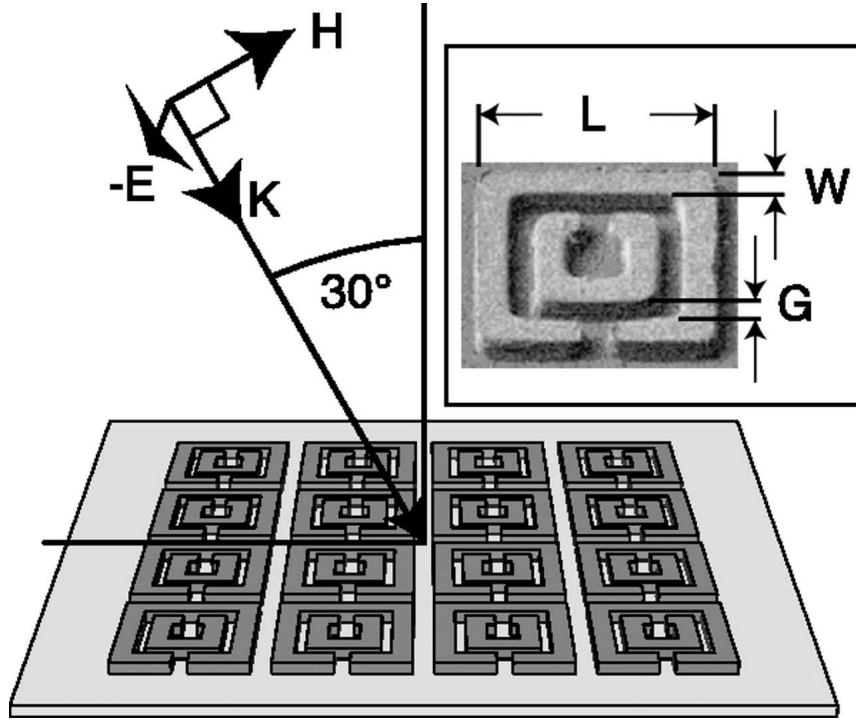


Figure 1.3: Planar structure composed of nonmagnetic conductive resonant elements, for magnetic metamaterial response at THz frequencies. (Inset) Ion-beam microscopy image of the fundamental structure. Taken from: T. J. Yen et al. *Science*, **303**, 1494, 2004.

composition of a wire-medium array and split ring resonators (SRRs). Simultaneous with the measured negative index of refraction Pendry envisioned that a LHM slab could constitute a perfect lens, such that not only travelling waves associated with an object but all the evanescent waves containing all fine near-field details could be retained in an image [53]. Since this moment, EM metamaterials has been a field of intense interest, where a huge amount of scientific outcome was produced like

THz artificial magnetism (Fig. 1.3) [54], the so-called fishnet structure for negative refraction [55] and electro-static optical negative refraction [56], etc.

The topics "extraordinary acoustical transmission" (EAT), acoustic metamaterial and acoustical phenomenon associated to surface waves are new and flourishing themes in the context of physical acoustics. Up to date, since the discovery of EAT for sound traversing through small apertures such as slits or holes, a large amount of progress has further examined the concept both from theoretical and experimental points of view [57]. However already in 2005, acoustic resonant transmission through subwavelength spaced sphere-arrays has been analysed [58]. Also a rather mathematical treatment of the problem regarding sound transmission through circular holes was presented [59]. In the next chapter a complete theoretical survey on this topic will be given, followed up by a conclusion where we highlight the progress made so far, and compare to our models where it is possible.

Metamaterials, particularly acoustics are still in the stage of infancy. However, as this broad field is quite a few years older than EAT, we intend to start out with a brief review on this topic. Acoustic metamaterials are being explored theoretically, but there has been little headway on the experimental front. In the same year, when Smith et al. demonstrated that the composition of magnetic resonators with a wire media would exhibit negative refraction, Z. Liu et al. published the first work ever on acoustic metamaterials [3]. By coating heavy spheres with soft silicon rubber and encasing the coated spheres in epoxy, an elastic inertial metamaterial was created with an effective negative mass-density. Fig. 1.4 illustrates this concept, which easily can be characterized as a mass-spring system, where the core is the mass and the rubber acts as a spring. Excited at the natural frequency of the resonator, the core oscillates strongly out of phase with the driving force, giving rise to transmission dips, due to a negative real part in the effective mass density. Other variations, such as an array of rubber spheres relying on Mie resonances, or the composition of two

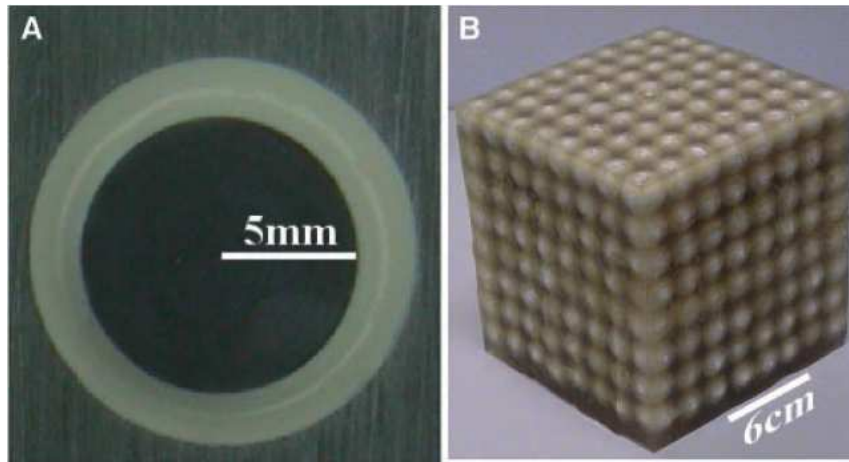


Figure 1.4: Cross section of a coated lead sphere that forms the basic structure of a 8×8 sonic crystal. Taken from: Z. Liu et al. *Science*, **289**, 1734, 2000.

face-centred arrays of fluidic and elastic resonators, have shown to be metamaterials, yielding a negative effective mass-density and bulk modulus [60, 61]. Another sonic metamaterial structure is the 1D array of Helmholtz resonators, known for the capability to act as a stopband filter [62, 63]. Fang et al. showed in 2006 that when this resonator is tuned to a frequency where the airy motion in the neck, in correspondence with the compressibility in the main cavity, is moving out of phase with the excited sonic compression and rarefaction, a negative bulk modulus is the cause. As of this single-negativity, acoustic waves of antiparallel group- and phasevelocity is conveyed.

Basic research has and will motivate the study of novel wave phenomena regarding acoustics and optics. But certainly the technological progresses for telecommunication, computers and data storage, such as medical and biological use make a clear statement on the dominance regarding the leading character of optics, compared to acoustical investigations. However the ability to focus, guide and in general to manipulate the natural properties of acoustic waves remains a subject of growing interest [64–66]. In the following section we therefore wish to motivate the reader

on the prominence regarding physical acoustics. Able to control sound at a sub-wavelength scale is the driving force for improvements and further developments for acoustical scanning, spectroscopy, medical ultrasound instrumentation, and imaging.

1.2 Motivation

As we have declared above, surface phenomena in nanophotonics and physical acoustics play an important role in modern studies related to metamaterials, enhanced transmission or field localization and guiding. The growth of the field of plasmonics is clearly reflected in the scientific literature. In the upper histogram of Fig. 1.5 we have graphed the annual number of publications, containing the phrase "surface plasmon" in the title or the abstract. The exponential growth is marked with a few temporal milestone achievements and discoveries, which we have announced in the latter section. The comparison with sound waves is an unambiguous interpretation of stepping into somebody's large footsteps, as the scientific outcome on "acoustic surface waves" (ASW) only is a tiny fraction of the plasmonic forerunner. Nevertheless, through half a century, the study on ASWs and plasmonics partially walked hand in hand, but already in this progress, acousticians have shown their independence, making the research on sound far more than a study of analogies. This is clearly demonstrated by the early emergence of commercialized SAW-devices in the 60s for telecommunication and filter components, 25 years before the first commercialized SPP bio-sensor (Fig. 1.5) [67, 68]. The degree of flexibility and applicability regarding ASWs was reported in 1996, where a group of experimentalists studied the interaction of 1D ballistic electrons with electrostatic waves induced by ASWs [69]. Thus it is fair to say, despite of the enormous need for optical devices in computers, DVD players and interconnects which clearly boost the scientific interest on nanoplasmonics, there is still a lot of room to study the effects and the properties associated with ASWs and acoustical metamaterials. Air-borne sound does

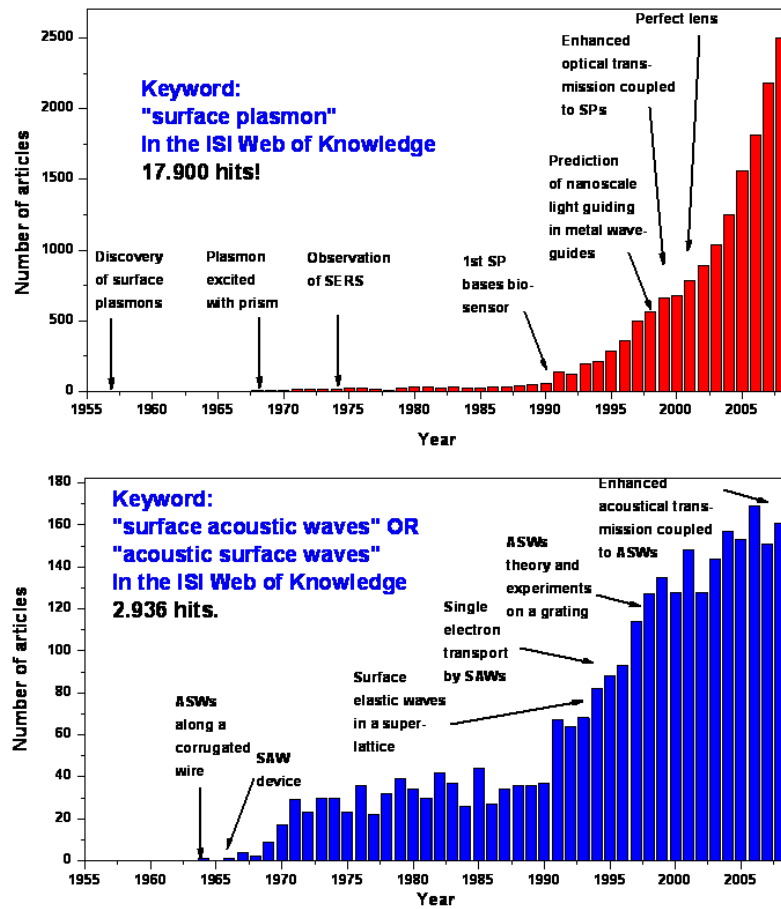


Figure 1.5: The growth of the fields, regarding surface waves for sound and light are compared by the number of scientific articles published in the years indicated. The search phrases illustrated, have been used in the ISI Web of Knowledge.

not polarize, and can resonantly interact with solid materials. Hence despite some similarities, intrinsic differences is giving rise to colourful behaviour of perforated or structured sonic systems.

1.3 Problem Statements

The research theme, defined by the latter review on nanoplasmonic achievements and their acoustical counterpart is clear. At first, a theoretical analysis is devoted

to the acoustical analogy of the EOT. By means of mathematical modelling analysis, sound waves are studied which are traversing through apertures in 1D and 2D that are smaller compared to the wavelength of incident sound. Second: a new waveguiding scheme is investigated, which is a study regarding the guiding and confinement of ASWs along the grooves, milled into a sound-hard wire. Third: an acoustical metamaterial based on a holey steel block is demonstrated to act as a quasi-perfect near-field imaging device, capable to capture ultrasonic objects by all its sub-diffraction limited component. Fourth: we are designing the acoustical equivalence of a double-fishnet structure, known in the context of negative refraction for EM metamaterials. However in its acoustical case, we predict that this system can act as an all-angle attenuator for sound waves, due to an effective negative bulk modulus.

For more details, we present the organisation of the thesis:

Chapter 2

In this initial part of the thesis, the basic linearised Eulers equations comprising small acoustical perturbation and a complete elastic equation of motion are derived. As a solution for a simple wave equation comprising the motion of air-borne sound, we employ the mode matching technique, which is decomposing a scattered-based problem, into the individual modal regions. By this we show how a metal plate perforated by an infinite array of slits can be modelled by this modal expansion technique and be integrated into a linear system of equations. Similarly for an array of holes, or individually isolated apertures such as a slit or a hole, we apply this modal expansion technique and perform detailed transmission studies for all cases. We are clarifying the responsible mechanism for an enhanced transmission, both for the periodic and the finite cases by means of linear algebra which results in dispersion relations, pressure field plots and effective medium approaches (long wavelength limit). We are concluding all findings and compare these results with the phenomena

associated to EOT.

Chapter 3

This 3rd chapter is devoted to the study of confining ASWs along a soundhard wire, that are supported by milling rings into it. This analogy of the spoof SPPs along a PEC wire, demonstrates the capability of the mode matching technique, also to function well for cylindrical geometries as the wire. From this technique we obtain a dispersion relation that is entirely controlled by the geometrical parameters constituting a corrugated wire, capable to support the propagation of surface waves - a *Metawire*. With this dispersion relation and pressure field plots in the unit cell, we give a clear account on the degree of the controllability of the designer ASWs, supported by the metawire. Based on these results, we analyse a modification leading to a corrugated cone and show how this new geometry can serve as a device for superfocusing sound beyond the diffraction limit. Also here we are concluding this chapter by a quantified comparison with the bands associated to slow light along a PEC wire.

Chapter 4

A brief highlight on EM and acoustic metamaterials is presented and we give a tutorial explanation on the basic principles regarding single and double negativity for engineered sonic materials. A basic holey structure is being taken under investigation, and we make a first-principle theoretical analysis to elucidate its properties for robust imaging. By means of both slit- and hole arrays, acting as holey metamaterials, we show how a deep subwavelength sonic object can be recovered by all its near-field component at an image plane. In the same context we are seeking to declare the resolution limit, with which an image can be resolved by the use of this mentioned system. This theoretical prediction is verified by experimental measurements, which concludes the investigation on sonic imaging for this chapter.

Chapter 5

In this chapter we start out with a modal expansion on the acoustical equivalence of a double-fishnet structure, where it clearly throughout this formalism is demonstrated that this structure can be treated as stack of two hole arrays. From the linear problem we are seeking symmetric and asymmetric solutions, which will form the basis to create understanding on the mechanism involved for sound interacting with the metallic structure and the gap. At the same time, we predict how the resonances involved also can be interpreted as a Fano-type resonance, which yields a negative effective bulk modulus. The properties of the single-negativity, responsible for the complete suppression of sound transmission, are investigated in such a way that the angle-dependence of incidence sound is given by means of a dispersion relation.

Chapter 6

The main results in this thesis are summarized and a overall conclusion is drawn herefrom.

Chapter 2

Enhanced acoustical transmission and basics

As already outlined in the introductory part of this thesis, a decade of intense work devoted to the EOT, which has sparked considerable fundamental but also technological interest, has become a milestone theme within the field of optics. As of this great implication, it is truly surprising that the acoustical analogy to this topic, first would see the light of day ten years later. In this chapter, we will go through the very fundamental aspects of modelling acoustic sound waves penetrating through small apertures compared to the wavelength of incident sound and by this demonstrating how the acoustical diffraction limit can be efficiently beaten. As this chapter provides first-principles theory of physical acoustics, it also serves as a tutorial backbone for the subsequent chapters, containing other objectives, though with equal fundamental character. In what follows, we are introducing the so-called mode-matching technique which is a flexible modelling tool, suitable to gather analytical insight into the physics involved. This technique can be used to solve a variety of problems such as the Schrödinger equation, Maxwell's equations and the linearised Euler's equations (LEEs) as will be shown here. To this, for all kind of geometrical structures presented, we do a convergence study in order to present full accurate solutions.

2.1 Air-borne sound

In this section we take a look into the derivation of the acoustical wave equation that will form the very basis of the entire scope within this thesis. Linear acoustics comprises small pressure fluctuations, that form a travelling wave of low intensity. Consider an invicid (lossless) fluid (liquid or gas) that is at rest. To connect the motion of the fluid with its compression or expansion, a relationship between the particle velocity \mathbf{v} and the mass density ρ is to be deduced. Regarding the forces, one has to apply Newton's second law and relating the sum of the forces acting on an element of fluid to its acceleration or rate of change of momentum. These two constituents are the foundations to describe acoustic waves of small disturbances in the absence of viscosity (constant entropy), that are gathered within the LEEs:

$$\frac{\partial \rho}{\partial t} + \nabla \cdot (\rho \mathbf{v}) = 0, \quad \frac{\partial \mathbf{v}}{\partial t} + (\mathbf{v} \cdot \nabla) \mathbf{v} = -\frac{\nabla p}{\rho}. \quad (2.1)$$

In the Eqs. (2.1), energy terms are disregarded and will not be part due to the absence of thermal gradients. For the pressure p , velocity \mathbf{v} and density ρ , one can write: $p = p_0 + p'$, $\mathbf{v} = \mathbf{v}_0 + \mathbf{v}'$, and $\rho = \rho_0 + \rho'$ where the terms p_0 , \mathbf{v}_0 and ρ_0 denote the background pressure, velocity ($\mathbf{v}_0 = 0$) and density in an undisturbed medium, respectively. The primed quantities p' , \mathbf{v}' and ρ' describe the variation in the corresponding magnitudes due to the presence of a low-amplitude acoustic field in the medium. If one now substitutes those quantities into Eqs. (2.1) and only linear terms in the primed quantities are taken into account while all higher-order terms are neglected, one obtains two simple equations:

$$\nabla \mathbf{v}' - \frac{i\omega}{c_0^2 \rho_0} p' = 0, \quad \nabla p' - i\omega \rho_0 \mathbf{v}' = 0, \quad (2.2)$$

that after straightforward algebra yields a simple wave-equation for linear sound propagation in fluids. Here, use has been made of monochromatic radiation and the isentropic relation $p' = \left(\frac{\partial p}{\partial \rho}\right)_s \rho' = c^2 \rho'$ upon assuming adiabatic and reversible conditions. For more details regarding this derivation one should refer to [70, 71].

2.2 Structure-borne sound

Air-borne or Fluid-borne sound as thoroughly has been characterised in the latter section, describes wave motion of scalar pressure fluctuations, which in its fundamental view is a longitudinal wave, propagating parallel to the axis of the displacement of adjacent fluid elements. Generally what is known about structure-borne sound (or elastic waves), is that the description of wave motion is to be treated as a vector, comprising longitudinal and transversal displacements of infinitesimal structure segments, in relation to the propagation direction. The wave motion of a non-piezoelectric, isotropic elastic material is governed by the general lossless equation of motion:

$$\rho \frac{\partial^2 u_i}{\partial t^2} = \frac{\partial \sigma_{ij}}{\partial x_j} \quad (2.3)$$

with solid material mass density ρ , the stress σ_{ij} and strain ε_{ij} tensors, comprising Cartesian components $i, j = x, y, z$, given as follows:

$$\sigma_{ij} = \lambda \delta_{ij} \varepsilon_{kk} + 2\mu \varepsilon_{ij}, \quad \varepsilon_{ij} = \frac{1}{2} \left(\frac{\partial u_i}{\partial x_j} + \frac{\partial u_j}{\partial x_i} \right). \quad (2.4)$$

λ , μ and u_i are the modulus of incompressibility (first Lamé coefficient), modulus of rigidity (second Lamé coefficient) and the i -th component of the displacement u respectively. This given, one obtains the complete elastic wave equation comprising longitudinal (compressional) and transversal (shearing) motion which for the sake of simplicity, as in Eq. (2.2), is given in vector notation:

$$\rho \frac{\partial^2 \mathbf{u}}{\partial t^2} = (\lambda + 2\mu) \nabla (\nabla \cdot \mathbf{u}) - \mu \nabla \times \nabla \times \mathbf{u}. \quad (2.5)$$

There to it can now be assumed that the field is purely transversal, thus applying the curl ($\nabla \times \mathbf{u}$) on the displacement vector in Eq. (2.5), all longitudinal terms vanish, which yields a wave equation

$$\frac{\partial^2 \mathbf{u}_t}{\partial t^2} = \frac{\mu}{\rho} \nabla^2 \mathbf{u}_t \quad (2.6)$$

with phase velocity $c_t = \sqrt{\frac{\mu}{\rho}}$ and transverse displacement vector \mathbf{u}_t [72].

2.3 Mode matching technique

The mode matching technique or the modal expansion (ME) formalism is a very general method for solving linear differential equations describing physical systems of very different nature. It is a very useful tool in current research in a broad range of fields such as acoustics, quantum mechanics or electromagnetics [73, 74]. In this section, we present a theoretical formalism for solving the above given equations in complex structures based on this technique. Special emphasis is given to the fluid part in section 2.1 as has been elucidated in the introductory part. Again, a great interest lies in the control of fluid-borne sound for, e.g., medical use and also the setups for experiments are greatly eased compared to the study of elastic waves. The study of acoustic transmission through subwavelength apertures, is in its simple form accomplished through an even and smooth surface (wall), which significantly eases the modelling by means of modal expansions. Taking the most general structure into

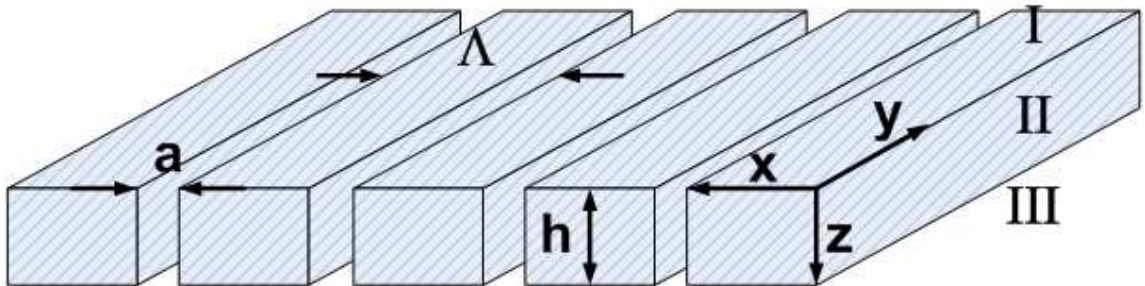


Figure 2.1: Schematics of a periodic array of slits, made out of a perfect rigid body, impenetrable for air-borne sound waves impinging on the structure.

account as Fig. 2.1 depicts, reduces the problem into a mode matching procedure containing three interfaces. The ME technique is based on the decomposition of sound- or elastic waves into eigenmodes and planewaves of the LEEs or equation of motion, within the various regions comprising the complex structure under study. Therefore,

by imposing the appropriate continuity conditions at the region boundaries (interfaces), the problem can be solved in all the space. Through out this chapter we will examine various structures of various dimensions. Initially, we start looking at the basic slit array arrangement, Fig. 2.1, as the understanding of this easily transfers to hole arrays and other geometries. A good assumption studying air-borne sound radiation on rigid materials such as concrete, steel or brass, is the *perfect rigid body* approximation (PRB). When air-borne sound is impinging on a thick steel plate for example, the wave will entirely be reflected. In other words, in the field of environmental, technical, and building acoustics, the PRB approximation has throughout the years shown to be a valid approach, treating the acoustics statically, such that the externally applied energy is vanishing into the rigid body [75, 76]. Let us make this clear with the given example of a slit array. Through out this work we are describing the waves as plane waves with wave vector \mathbf{k} traversing a given medium. Before initiating the example, we need to define an acoustical index of refraction, in order to define an appropriate wave number for a given medium. Following the basic prescription from optics [77], easily transferable to acoustics [60] with an index of refraction $n = c_0/c_p$ which is nothing but $\sqrt{K_0/\rho_0}\sqrt{\rho_p/K_p}$, with c , K , ρ representing the phase velocity (thermodynamic speed of sound), the bulk modulus and density respectively, where the *zero* and *p* indices refers to a reference medium (such as air) and phase (any arbitrary medium) respectively. Consequently it is convenient to rewrite $n = \sqrt{\rho_r/K_r}$ into relative terms, which gives a unity refraction index for air. Following Fig. 2.1, we start deducing a wave description in region *I*. In this particular periodic case, we expand the wave into Bloch states by means of a reciprocal lattice vector. Note, as of translational invariance along the y-axis of the structure, it is sufficient to regard the sagittal (xz) plane. Also, only the z-component, v'_z , of the velocity vector will be taking into account, because v'_z is employed for the matching technique and in order to simplify the notations, we choose to reject the primes in p' and v'_z as given in Eqs. (2.2), though it is clear that acoustical quantities

are considered. The acoustical field associated with the incident and the resulting reflected wave, ($z < 0$), represented as a sum of plane-waves weighted with their corresponding reflection coefficients R_γ , is:

$$\begin{aligned} |p^I(z)\rangle &= Y_{k_z^0}^I |k_x^0\rangle e^{ik_z^0 z} + \sum_{\gamma=-\infty}^{\infty} R_\gamma Y_{k_z^\gamma}^I |k_x^\gamma\rangle e^{-ik_z^\gamma z} \\ |v_z^I(z)\rangle &= |k_x^0\rangle e^{ik_z^0 z} - \sum_{\gamma=-\infty}^{\infty} R_\gamma |k_x^\gamma\rangle e^{-ik_z^\gamma z}. \end{aligned} \quad (2.7)$$

Here the free space plane waves $\langle x|k_x^\gamma\rangle = \frac{e^{ik_x^\gamma x}}{\sqrt{\Lambda}}$, incident wave vector $\mathbf{k}_0 = (k_x^0, k_z^0)$ and the scatterer components $\mathbf{k}_\gamma = (k_x^\gamma, -k_z^\gamma)$ containing discrete diffraction order γ in the range $\gamma = -\infty, \dots, \infty$ comprising in-plane scattering where $k_x^\gamma = k_x^0 + \frac{2\pi}{\Lambda}\gamma$ and $k_z^\gamma = \sqrt{(n_I k_0)^2 - (k_x^\gamma)^2}$ with $\frac{2\pi}{\Lambda}\gamma$ representing the reciprocal lattice vector in the primitive unit-cell of constant Λ . When employing the PRB approach, the same scattering properties are obtained in different frequency regimes by scaling all the geometrical parameters with the same factor. Due to that, in our calculations, we will use Λ as the unit length defining the structure. Y_k is the so called admittance that governs the relationship between pressure and the velocity, derived from the momentum equation in Eqs. (2.2) which for the reflected wave in particular is nothing but $Y_{k_z^\gamma}^I = c_0 \rho_p^I \frac{k_0}{k_z^\gamma}$. With $\lambda = \frac{2\pi}{k_0}$ we define the angle of incidence with respect to the normal of the surface as ϕ , so with no loss of generality, $k_z^\gamma = k_0 \sqrt{n_I^2 - (\sin\phi + \gamma \frac{\lambda}{\Lambda})^2}$. If $\eta_\gamma = \sin\phi + \gamma \frac{\lambda}{\Lambda}$ we reach to the final simplifications of $k_z^\gamma = k_0 \sqrt{n_I^2 - \eta_\gamma^2}$ and henceforth $Y_{k_z^\gamma}^I = \frac{c_0 \rho_p^I}{\sqrt{n_I^2 - \eta_\gamma^2}}$.

Region *II* ($0 \leq z \leq h$) can be modelled as cavities with perfect rigid walls. Within this PRB-approximation no sonic energy is penetrating into the material, which is valid for a broad range of frequencies for e.g. steel, brass or concrete. Thus the boundary conditions in the apertures are as follows: $\frac{\partial p}{\partial \mathbf{n}} = 0$ at $x = \pm \frac{a}{2}$, which is nothing but a vanishing normal component of the particle velocity v_x with respect to the adjacent faces within the slit in an unit cell. This statement complies with v_z to be zero at top and bottom interfaces corresponding to $z = 0$ and $z = h$. The

normalized modes of the cavity waveguide are given as $\langle x|m\rangle = \sqrt{\frac{2-\delta_{0m}}{a}} \cos q_x^m (x + \frac{a}{2})$ where the m^{th} slit waveguide mode is in the range ($m = 0, 1, 2, \dots, \infty$) and $q_x^m = \frac{m\pi}{a}$. The entire eigenvalue expression for the field inside the slit, is the following:

$$\begin{aligned} |p^{II}(z)\rangle &= \sum_m Y_{q_z^m}^{II} (A_m e^{iq_z^m z} + B_m e^{-iq_z^m z}) |m\rangle \\ |v_z^{II}(z)\rangle &= \sum_m (A_m e^{iq_z^m z} - B_m e^{-iq_z^m z}) |m\rangle, \end{aligned} \quad (2.8)$$

with wave vector and admittance as $q_z^m = \sqrt{(n_{II} k_0)^2 - (\frac{m\pi}{a})^2}$, $Y_{q_z^m}^{II} = c_0 \rho_p^{II} \frac{k_0}{q_z^m} = \frac{c_0 \rho_p^{II}}{\sqrt{n_{II}^2 - \alpha_m^2}}$ respectively while $\alpha_m = \frac{m\lambda}{2a}$. A_m and B_m are the expanded wave amplitudes that are to be solved for in the matching procedure.

In the lowest region (*III*) ($z > h$) the acoustic waves emerge and the fields, as in Eqs. (2.7), are expanded out in linear diffracted Bloch waves with T_γ being the transmission coefficient:

$$\begin{aligned} |p^{III}(z)\rangle &= \sum_{\gamma=-\infty}^{\infty} Y_{k_z^\gamma}^{III} T_\gamma |k_x^\gamma\rangle e^{ik_z^\gamma(z-h)} \\ |v_z^{III}(z)\rangle &= \sum_{\gamma=-\infty}^{\infty} T_\gamma |k_x^\gamma\rangle e^{ik_z^\gamma(z-h)}. \end{aligned} \quad (2.9)$$

Clearly Eqs. (2.9) is a solution for waves travelling only in one direction, towards increasing values for z . Before the mode matching procedure on air-borne sound through a slit array continues, it will now become clear, how Eqs. (2.7-2.9) can be exercised for an equivalent study, regarding elastic waves in solids, when transmission properties are sought through an array of subwavelength plates. To illustrate this, it is convenient regarding Fig. 2.1 simply by interchanging the fluid regions with a solid material and vice versa. Now we assume that the elastic wave is purely transversal with a displacement $(0, u_y, 0)$ along the y -axis, that is, the elastic wave is shear horizontally (SH) polarized and is described by Eq. (2.6). Furthermore, it is assumed that no body forces are acting on the free surfaces, hence for an incoming SH-wave (propagating in the xz -plane and displacing orthogonal to this plane), shear-stresses will vanish on all free faces: $\frac{\partial u_y}{\partial x} = \sigma_{xy} = 0$ regarding the plates (combs)

and $\frac{\partial u_y}{\partial z} = \sigma_{zy} = 0$ depicting vanishing displacement divergence at the adjacent half-space planes ($z = 0, h$) that are separated by the plates. The transverse vibration will thus be incident to the free surface and subsequently been guided through the plates. When applying the mode matching technique, u_y and σ_{zy} are to be applied and arranged similar as Eqs. (2.7-2.9) as these terms are continuous at all interfaces. As one now may observe is that the formalism constituting either fluid-borne or SH waves, will remain equivalent, hence the resulting physical behaviour are of similar nature.

Going back to the fluid case, the matching conditions yield a linear system of equations for acoustic waves in liquids or gasses. At all interfaces the matching conditions are applied on the pressure p while being projected over cavity modes $\langle m' |$, such as on the fluid particle velocity v_z that is projected over plane waves $\langle k_x^\gamma |$. It follows from this, that all linear expansion coefficients in Eqs. (2.7-2.9) can be extracted, when one first imposes continuity in pressure p at the openings and the endings of the slits and secondly does so regarding the velocity v_z though along the entire unit-cell at the interfaces $z = 0, h$. Following this sequential scheme, one creates a systematic top-down (from region *I* to *III*) wave mode coupling approach that with given attributes (functions), owns the ability to describe the entire acoustical problem under study and yields a quantitative field representation through out all space. Let us put this into equations. At the interface ($z = 0$) between region *I* and *II*) the pressure and velocity continuity equations read:

$$\begin{aligned}
Y_{k_z^0}^I |k_x^0\rangle + \sum_{\gamma=-\infty}^{\infty} R_\gamma Y_{k_z^\gamma}^I |k_x^\gamma\rangle &= \sum_m Y_{q_z^m}^{II} (A_m + B_m) |m\rangle \\
|k_x^0\rangle - \sum_{\gamma=-\infty}^{\infty} R_\gamma |k_x^\gamma\rangle &= \sum_m (A_m - B_m) |m\rangle,
\end{aligned} \tag{2.10}$$

which is nothing but the matching of Eqs. (2.7) with Eqs. (2.8). Again, the first mode matched equation in Eq. (2.10) representing the pressure p is solely continuous over the slit entrance while the second term in Eqs. (2.10) for the velocity v_z constitutes steadiness through out the entire interface $z = 0$. This being stated and

employed on Eqs. (2.10), leads to the following expressions:

$$\begin{aligned}
Y_{k_z^0}^I S_{0m'} + \sum_{\gamma=-\infty}^{\infty} R_{\gamma} Y_{k_z^{\gamma}}^I S_{\gamma m'} &= Y_{q_z^m}^{II} (A_m + B_m) \delta_{mm'} \\
\delta_{0\gamma'} - R_{\gamma'} &= \sum_m (A_m - B_m) S_{\gamma' m}^*.
\end{aligned} \tag{2.11}$$

It has possibly been observed that the waveguide modes such as the plane waves, are defined on a orthogonal basis: $\langle m|m' \rangle = \int \langle m|x \rangle \langle x|m' \rangle dx = \delta_{mm'}$ and $\langle k_x^{\gamma}|k_x^{\gamma'} \rangle = \int \langle k_x^{\gamma}|x \rangle \langle x|k_x^{\gamma'} \rangle dx = \delta_{\gamma\gamma'}$ respectively. Hence, whilst imposing continuity, to an efficient extend, Eqs. (2.11) are significantly simplified where the following definition has been set: $S_{\gamma m} = \langle k_x^{\gamma}|q_x^m \rangle = \int \langle k_x^{\gamma}|x \rangle \langle x|q_x^m \rangle dx$ which is an integral, defining the modal overlap between slit cavity modes q_x^m and the free space plane waves k_x^{γ} (see appendix A). Out from Eqs. 2.11 we immediately see that the reflection coefficient takes the following expression:

$$\boxed{R_{\gamma'} = \delta_{0\gamma'} - \sum_m (A_m - B_m) S_{\gamma' m}^*}, \tag{2.12}$$

hence when solved for this function in Eqs. (2.11), we gather those terms into one simple system:

$$2Y_{k_z^0}^I S_{0m'} = \sum_{m'} \sum_{\gamma=-\infty}^{\infty} Y_{k_z^{\gamma}}^I S_{\gamma m'} S_{\gamma m}^* (A_{m'} - B_{m'}) + Y_{q_z^m}^{II} (A_m + B_m) \delta_{mm'}. \tag{2.13}$$

In a similar manner continuity is preserved at the wave emerging interface ($z = h$), between region (*II* and *III*) with pressure and velocity:

$$\begin{aligned}
\sum_m Y_{q_z^m}^{II} (A_m e^{iq_z^m h} + B_m e^{-iq_z^m h}) |m\rangle &= \sum_{\gamma=-\infty}^{\infty} Y_{k_z^{\gamma}}^{III} T_{\gamma} |k_x^{\gamma}\rangle \\
\sum_m (A_m e^{iq_z^m h} - B_m e^{-iq_z^m h}) |m\rangle &= \sum_{\gamma=-\infty}^{\infty} T_{\gamma} |k_x^{\gamma}\rangle.
\end{aligned} \tag{2.14}$$

By this imposed steadiness at that particular interface, the pressure p is projected over cavity modes $\langle m'|$ and the velocity v_z over plane waves $\langle k_x^{\gamma}|$ just as in the latter

case:

$$\begin{aligned}
Y_{q_z^m}^{II} (A_m e^{iq_z^m h} + B_m e^{-iq_z^m h}) \delta_{mm'} &= \sum_{\gamma=-\infty}^{\infty} Y_{k_z^\gamma}^{III} T_\gamma S_{\gamma m'} \\
\sum_m (A_m e^{iq_z^m h} - B_m e^{-iq_z^m h}) S_{\gamma' m}^* &= T_{\gamma'}.
\end{aligned} \tag{2.15}$$

To this extend, as the 2nd part in Eqs. (2.15) reveals, a transmission coefficient of the form

$$\boxed{T_{\gamma'} = \sum_m (A_m e^{iq_z^m h} - B_m e^{-iq_z^m h}) S_{\gamma' m}^*} \tag{2.16}$$

is evident. Here with Eq. (2.16) substituted into Eqs. (2.15); all what remains is an entire mode deduction at $z = h$ that is nothing but:

$$\sum_{m'} \sum_{\gamma=-\infty}^{\infty} Y_{k_z^\gamma}^{III} S_{\gamma m'} S_{\gamma m}^* (A_{m'} e^{iq_z^{m'} h} - B_{m'} e^{-iq_z^{m'} h}) = Y_{q_z^m}^{II} (A_m e^{iq_z^m h} + B_m e^{-iq_z^m h}) \delta_{mm'}. \tag{2.17}$$

Before gathering Eq. (2.13) and Eq. (2.17) into a final system of equations, we will define two quantities that are serving as a further reduction, in order to obtain a high degree of analytical insight into the problem, which are the modal velocity amplitudes at input (unprimed) and at the output (primed) side:

$$\begin{aligned}
v_m &= A_m - B_m \\
v'_m &= -(A_m e^{iq_z^m h} - B_m e^{-iq_z^m h}).
\end{aligned} \tag{2.18}$$

Substituting those two modal definitions into the continuity systems at the wave incidence, Eq. (2.13), and wave emerging side, Eq. (2.17), a final compact linear system of equations is unravelled:

$$\boxed{
\begin{aligned}
(G_{mm} - \epsilon_m) v_m + \sum_{m' \neq m} G_{mm'} v_{m'} - G_m^V v'_m &= I_m^0 \\
(G_{mm} - \epsilon_m) v'_m + \sum_{m' \neq m} G_{mm'} v'_{m'} - G_m^V v_m &= 0
\end{aligned}
} \tag{2.19}$$

This linear system of equations is the very foundation of all the structures described within the framework of this thesis. With no loss of generality, as can be seen in

the subsequent chapters this modal expansion technique will serve as the tool to pursue physical insight in the transmission study of sound being funnelled through subwavelength apertures. If this system is solved for the unknown modal velocities v_m and v'_m an entire field mapping can be obtained, comprising far-field and near-field distributions. Moreover, the energy flux through the structure can be described by the acoustical analogy of the EM Poynting vector which is nothing but the acoustical intensity:

$$I_{sound} = \int \text{Re}\langle x|p\rangle\langle x|v_z\rangle dx. \quad (2.20)$$

Whether the transmittance is sought in the near-field (through the hole) or in the far-field, will in the absence of viscous losses and vibrational energy absorption (PRB-approximation) be irrelevant. In other words, as a fraction of the acoustical intensity Eq. (2.20) at the holes entrance and emission side, we get:

$$T_{near} = \frac{1}{Y_{k_z^0}} \text{Re}\left(\sum_m Y_{q_z^m}^{II} (|A_m|^2 - |B_m|^2)\right) = \frac{1}{Y_{k_z^0}} \text{Im}\left(\sum_m G_m^V v_m v_m'^*\right). \quad (2.21)$$

This equation was restated with the definitions in Eq. (2.18), for more details see appendix A. Eq. (2.21) is consequently equal in the far-field as no acoustic energy experiences attenuation, hence:

$$T_{far} = \frac{1}{Y_{k_z^0}} \text{Re}\left(\sum_{\gamma=-\infty}^{\infty} Y_{k_z^\gamma}^{III} |T_\gamma|^2\right) = \frac{1}{Y_{k_z^0}} \text{Im}\left(\sum_{m,m'} G_{mm'} v_m v_{m'}'^*\right). \quad (2.22)$$

The mathematical functions within Eqs. (2.19) will be elucidated in the following section, so far we solely want to explain those functions in a qualitative picture: In the inhomogeneous set of linear equations in Eq. (2.19), representing the side of sonic irradiation I_m^0 , components of acoustic self-radiation G_{mm} for the m -th cavity mode, the mutual sound interaction function $G_{mm'}$ between mode m and mode m' via diffracted orders and the interface coupler G_m^V at the m -th mode such as the bidirectional field propagation function ϵ_m are found. For the wave emerging side of the structure, an equivalent, though homogeneous system is assembled.

2.4 Transmission through a single slit

As has already been detailed in the introductory part of this thesis, stimulated by the EOT phenomena observed in 2D arrays of subwavelength holes, a renewed interest in the EM properties of subwavelength arrays of slits perforated in metallic films has been initialized. Studying slit arrays would ease the understanding of EOT through holes, but it was also a natural transition to follow, to expect that high transmission also would appear for those structures. Slit arrays have thoroughly been analyzed theoretically, where the two types of transmission resonances were predicted: coupled SPPs resonances and slit waveguide modes [78]. Experimental verification of the existence of these transmission resonances has been reported in the microwave regime [79]. In order to give a clear physical explanation of the origin of the extraordinary transmission peak from a metallic slit grating, Takakura [80] analyzed the interaction of TM-polarized waves with a single subwavelength metallic slit. The results show, for a thick enough conducting plate, a series of resonant transmission peaks with growing wavelength appear [23, 81]. Conclusively the excitation of those standing wave modes (Fabry-Perot (FP) resonances) are responsible for those transmission peaks in a single isolated slit, but among other mechanisms, also for slit arrays.

In connection with sound absorbing panels and room insulation, transmission of sound through arrays of variously shaped apertures but also isolated holes and slits has already been of interest in the past [82–86]. The models presented were based on lumped parameters containing aperture flow and radiation impedances, giving rise to rather complex expressions which were not in favour for the physical insight. Fig. 2.2 illustrates a single isolated subwavelength slit that is irradiated by sound, which forms the subject for this section. In here we not only want to emphasize the resonant modes which, as we will see later, give rise to enhanced transmission for sound, but we wish to illustrate what unique features this structure provides. The isolated slit from Fig. 2.2 again is subdivided into the 3 regions of wave expansions.

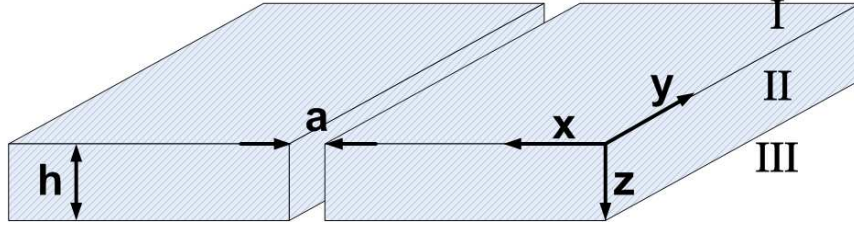


Figure 2.2: Schematics of a single slit, made out of a perfect rigid body, impenetrable for air-borne sound waves impinging on the structure.

When modal expansions are employed, we reach to a similar system of equations as presented in the latter section 2.3, though with the important attribute of being devoted to a non-periodic (finite) structure - a single isolated scatterer:

$$(G_{slit} - \epsilon)v - G^V v' = I^0, \quad (G_{slit} - \epsilon)v' - G^V v = 0. \quad (2.23)$$

As we consider a finite structure ($\Lambda_x \rightarrow \infty$), the discrete diffraction modes need to be restated into a continuous spectrum in k_x . As a consequence of this, the components in Eqs. (2.23) are being formulated under the fundamental slit waveguide mode approximation $m = 0$ at normal incidence ($k_x^0 = 0$):

$$I^0 = 2i \quad (2.24)$$

$$G^V = \frac{1}{\sin k_0 h} \quad (2.25)$$

$$\epsilon = \frac{1}{\tan k_0 h} \quad (2.26)$$

for $n_I = n_{II} = n_{III}$,

$$G_{slit} = \langle m = 0 | \tilde{G} | m' = 0 \rangle \quad (2.27)$$

with operator \tilde{G} :

$$\tilde{G} = \frac{i}{\lambda} \int_{-\infty}^{\infty} \frac{|k_x\rangle \langle k_x|}{\sqrt{k_0^2 - k_x^2}} dk_x. \quad (2.28)$$

As we are mainly interested in subwavelength apertures, we consider that only the fundamental propagating slit-eigenmode is excited. This mode converges very fast in the ME for a periodic case, see section 2.6. Eqs. (2.24-2.26) are very simple functions that straightforward can be implemented. Eq. (2.27) on the other hand can either be solved semi-numerically by rewriting it to the given form:

$$G_{slit} = \frac{ia_x k_0}{2\pi} \int_{-\infty}^{\infty} \frac{\text{sinc}^2\left(\frac{k_x a_x}{2}\right)}{\sqrt{k_0^2 - k_x^2}} dk_x, \quad (2.29)$$

or restating it into a Greens function on a position basis ($a_x \rightarrow a$):

$$G_{slit} \rightarrow G_{x,x'} = \langle x | \tilde{G} | x' \rangle = \frac{i\pi}{\lambda} \int_{-a/2}^{a/2} \int_{-a/2}^{a/2} H_0^{(1)}(k_0 |x - x'|) dx dx' \quad (2.30)$$

where $H_0^{(1)}$ is the zero-order Hankel function of the first kind. This function in turn can be further simplified for small or very large arguments, regarding the wavenumber and the slit width ka . Fig. 2.3 illustrates the transmission spectrum along with the

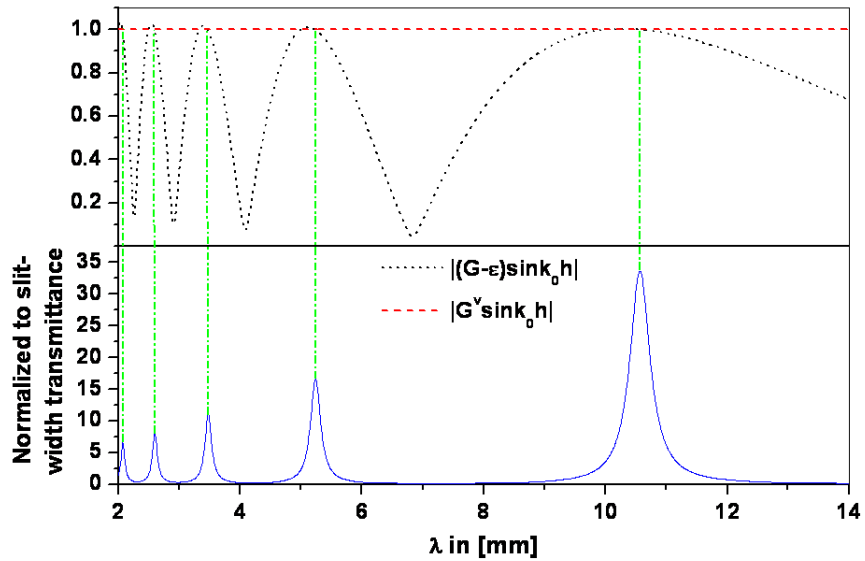


Figure 2.3: Transmittance spectrum for a single slit and the locations of the non-trivial solutions for a structure of thickness $h = 5$ mm and slit width $a = 0.02h$

non-trivial solutions as of the vanishing determinant in Eqs. (2.23). The geometries

which are given in the figure caption are chosen in order to justify the assumption of an inviscid fluid and to present a broad range of resonances. Indeed Fig. 2.3 reveals a broad distribution of discrete resonances which is linked to the growing normalized-to-area transmittance. E.g., for the peak at the highest wavelength a significant amount of sound is squeezed through the slit, as the transmitted intensity is about 35 times larger than the one impinging directly at the slit opening. The spectrum depicting non-trivial solutions, $|G_{slit} - \epsilon| - |G^V| = 0$, has been normalized with $\sin k_0 h$, which indicates the influence of diffraction, marking the variance of the actual solution to an exact FP resonance. This is the origin of the transmission peaks at around $\sin k_0 h = 0$, $\lambda = \frac{2h}{1}, \frac{2h}{2}, \frac{2h}{3} \dots \frac{2h}{m}$. This slight variance can be overcome within the long wavelength approximation, in other words when we choose an extremely small slit such that $\lambda \gg a$. The proof of that statement is hidden in the determinant when $|v| = |v'|$ which makes room for a further reformulation of the Eqs. (2.23) into the following resonant condition:

$$\tan k_0 h = \frac{2\text{Re}(G_{slit})}{|G_{slit}|^2 - 1}. \quad (2.31)$$

In the limit of extremely small apertures ($G_{slit} \rightarrow 0$), Eq. (2.31) predicts the appearance of transmission peaks close to the condition $\sin k_0 h = 0$ which we have already seen from Fig. 2.3. It is even possible to extract some analytical expressions for the normalized-to-area transmittance at resonance (T_{res}) for the isolated single slit. By incorporating the resonant condition, Eq. (2.31), into the equation $T_{slit} = \frac{1}{a} \text{Im}(G^V v v'^*)$ normalized to the slit width, it is found that:

$$T_{res} = \frac{|I^0|^2}{4\text{Im}(G_{slit})}. \quad (2.32)$$

As mentioned before and demonstrated in Eq. (2.31), we can isolate the FP resonances when we spectrally are located in the long wavelength regime compared to the size of the aperture. We can unambiguously demonstrate that for the extreme condition ($G_{slit} \rightarrow 0$), though restricting ourselves to a realistic case such that $\lambda \gg a$, propagating waves $k_0 \geq k_x$ within the system dominate the event and the overlap

function is nothing but $G_{slit} \approx i \frac{a\pi}{\lambda}$ which to the end, simplifies Eq. (2.32) into:

$$T_{res}^{slit} = \frac{\lambda}{\pi a}. \quad (2.33)$$

This expression is an accurate estimation for the linear growth in the transmittance for sound funnelled through narrow slits, which is a very interesting analytical result, as it implies an growth in T_{res}^{slit} as the resonant wavelength is increased. In the EM case, there is no broad range of cavity transmission resonances for subwavelength holes, due to the existence of a cut-off wavelength. However, this is not the case for a single slit and p -polarized light that is similar to the current findings. Fig. 2.4 serves

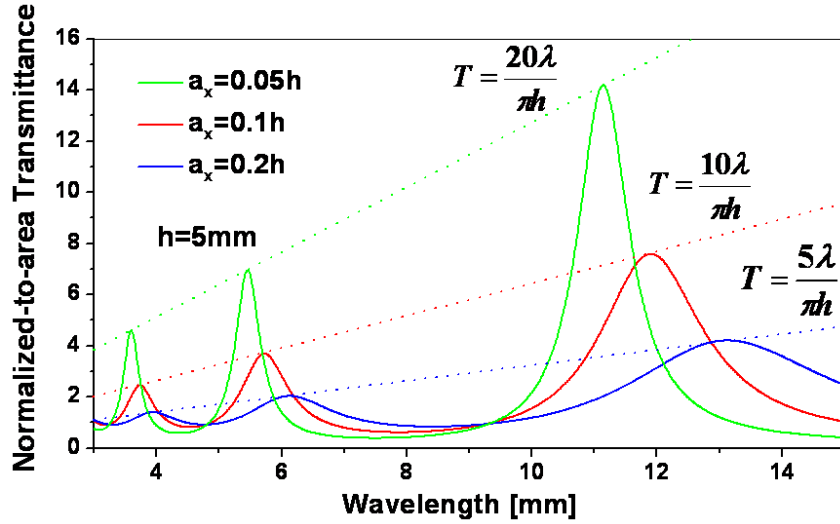


Figure 2.4: Transmittance spectra for single slits of three different geometries as given in the figure.

as a demonstration for the linear growth of the transmittance with the wavelength, but also validates the exact analytical geometry-dependent prediction, given in Eq. (2.33). In that respect we are examining the sound transmission through a plate of constant thickness ($h = 5\text{mm}$), but with different slit widths as indicated in Fig. 2.4. Our interest is devoted to spectral regimes of wavelengths being larger than a . For three different sets of slit-width $a = (0.2, 0.1, 0.05)h$ a growing transmittance with

wavelength for all cases is to be observed. Here Eq. (2.33) has been employed with the appropriate values for the slit width a , giving rise to a line that exactly matches the transmittance peaks for all wavelength. What might seem counter-intuitive but evident, is the increased slope with smaller values for a . The FP modes, $\text{sink}_0 h = 0$, which dominate the transmission spectra are better matched (see Fig. 2.4) the smaller the slits are, which is not surprising as that particular resonant condition easily is obtained for vanishing diffraction coupling ($G_{slit} \rightarrow 0$). This condition is achieved when the aperture is very small, and explains the shift towards the exact resonant locations $\lambda = 2h, h$ and $\frac{2}{3}h$. In relation to this, Fig. 2.5 surprises us only very little as

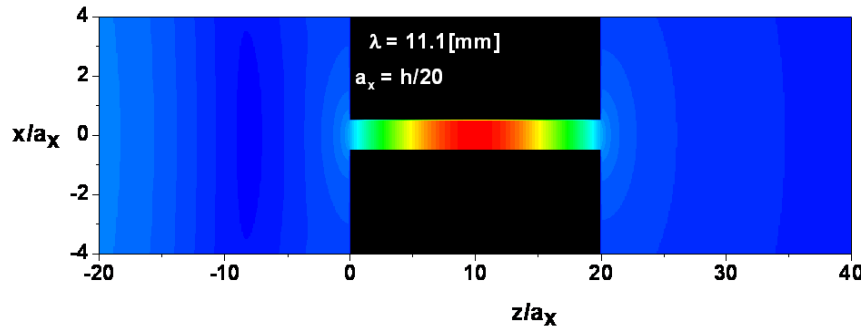


Figure 2.5: Modulus of the complex pressure field plotted for a single isolated slit, corresponding to $\lambda = 2h$. (Red: Max, Blue: Min).

we now have understood the resonant condition of an isolated single slit, that is due to the excitation of a standing wave mode within the slit. In here we have chosen to illustrate to lowest mode for the smallest aperture ($a = 0.05h$) from Fig. 2.4. To this end, we can hereby confirm on the similarity in single subwavelength slits drilled into PEC for the study of EM waves, compared to our acoustical case. It is also clear that this isolated aperture, forms a solid foundation in order to study the periodic arrangements of slits, as one of the main mechanisms (FP mode) for enhancing the very intensity of sound funnelled through these narrow periodic openings, is not governed by the periodicity contained.

2.5 Transmission through a single hole

This section deals with the second geometry for sound transmission studies. In 2004 A. Degiron et al. [87] presented an experimental study regarding the influence of hole shape on the optical transmission properties of a single subwavelength hole. Here it was demonstrated that transmission through a rectangular hole presents strong polarization dependencies and higher transmittance than square or circular hole with the same area. It was also shown that an isolated rectangular hole would support transmission resonances in the subwavelength regime. One year later Garcia-Vidal et al. [88] theoretically predicted that one of these resonances in a PEC appeared near the cutoff wavelength and that all discrete transmittance peaks were controlled entirely by the geometries such as the side of the hole. Additionally with an dielectric filling inside the aperture, the transmittance can be further tuned and increased [89]. Fig. 2.6 shows the diagram of a single rectangular hole of sides a_x and a_y perforated

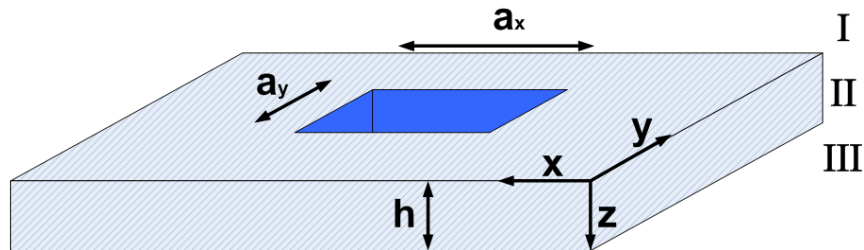


Figure 2.6: Schematics of a single isolated hole, made out of an perfect rigid body, impenetrable for air-borne sound waves impinging on the structure.

on a perfect rigid steel plate of thickness h , which is being irradiated by sound under normal incidence, exactly as in the preceding section. Continuity obviously also prevails when a holey structure is examined, in short we can conclude that the formalism derived in previous sections, easily applies to the present case. The overlap

between the incident sound field and the fundamental waveguide mode is written as:

$$G_{hole} = \frac{ia_x a_y k_0}{(2\pi)^2} \int_{-\infty}^{\infty} \int_{-\infty}^{\infty} \frac{\text{sinc}^2\left(\frac{k_x a_x}{2}\right) \text{sinc}^2\left(\frac{k_y a_y}{2}\right)}{\sqrt{k_0^2 - k_x^2 - k_y^2}} dk_x dk_y, \quad (2.34)$$

which is very similar to the 1D case, see Eq. (2.29). First, we analyse the case of a square hole of side $a = 1.06\text{mm}$ and thickness $h = 2.0\text{mm}$ (Geometries from a recent experiment [90]), which presents the same area as the circular holes forming the 2D array studied in [90]. In the inset of Fig. 2.7, a contour-plot of the normalized-to-area transmittance (normalized to the acoustic energy flux impinging directly at the hole opening) for a normally incident plane wave is shown as a function of wavelength and h . A set of resonances emerge in the transmission spectrum whose peak wavelengths depend almost linearly with h , suggesting a Fabry-Perot type origin. Although the existence of these resonances were reported many years ago for circular [91] and rectangular [92] holes, little attention has been paid to analyse in detail their physical origin. The lower panel of Fig. 2.7 illustrates the predictability of those resonances by means of the determinant, but as the hole is only slightly smaller than the wavelength, we find a discrepancy between the exact location for FP modes (dashed vertical lines) and the actual resonant transmission peaks.

In the following we are going into the physics involved, by choosing geometries similar to the ones for a isolated slits, presented in Fig. 2.4 but for quadratic holes ($a_x = a_y$). We have calculated the spectral transmittance curves which can be observed in Fig. 2.8. Also in this figure, when comparing to the previous evaluation in Fig. 2.4, we see that the normalized transmittance grows with wavelength. Interestingly, it seems that all peaks for the chosen values of a_x, a_y , coincides in their spectral locations with the transmittance peaks for the isolated slits. Mathematically we have already proven this indirectly, by deploying the resonant condition Eq. (2.31). Analogous to the slit, in the long wavelength limit ($\lambda \gg a_x, a_y$) for very small holes, the overlap function $G_{hole} \rightarrow 0$ which in turn isolates the FP condition in Eq. (2.31). Consequently, the FP mode only depends on the metal thickness, which explains

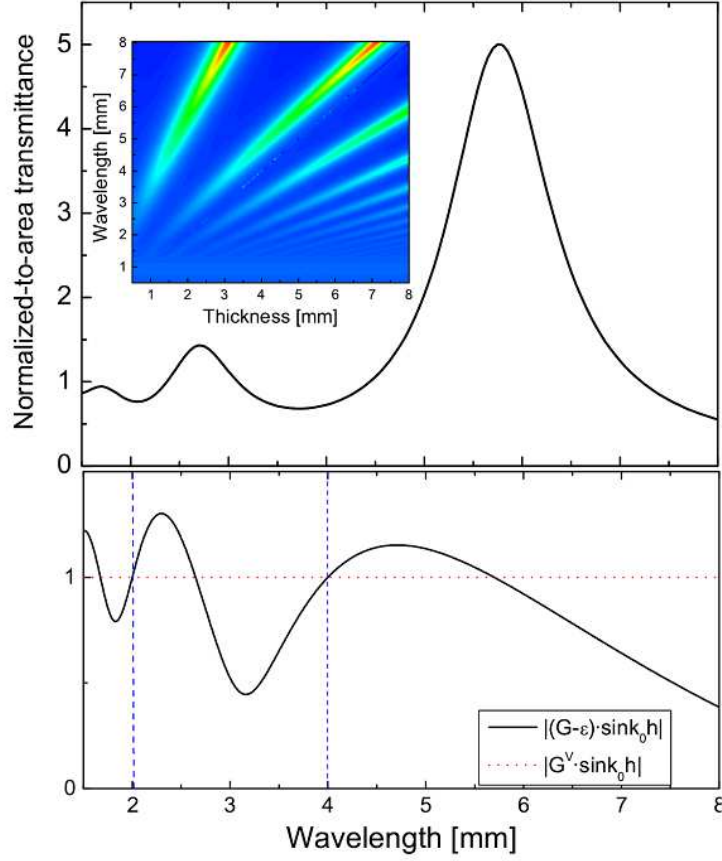


Figure 2.7: Transmittance spectrum for a single hole and the locations of the non-trivial solutions for a structure of thickness $h = 2$ mm and a square hole of size $a = 1.06$ mm

the agreement in the spectral peak locations when comparing Fig. 2.4 and Fig. 2.8. Note here, for the case with the smallest holes, $a_x = a_y = 0.05h$, we observe a precise matching of $\lambda_{FP} = \frac{2h}{m}$ which also holds true for the slit. However, a distinct difference has to be borne in mind, which is the quadratic nature of the overlap between diffracted waves and the fundamental hole mode. Because propagating waves $k_0 \geq k_x, k_x$ within the system are dominant, the overlapping function reads: $G_{hole} \approx 2i \frac{a_x a_y \pi}{\lambda^2}$. This namely, with the condition $T_{res} = |I^0|^2 / 4\text{Im}(G_{hole})$ is giving

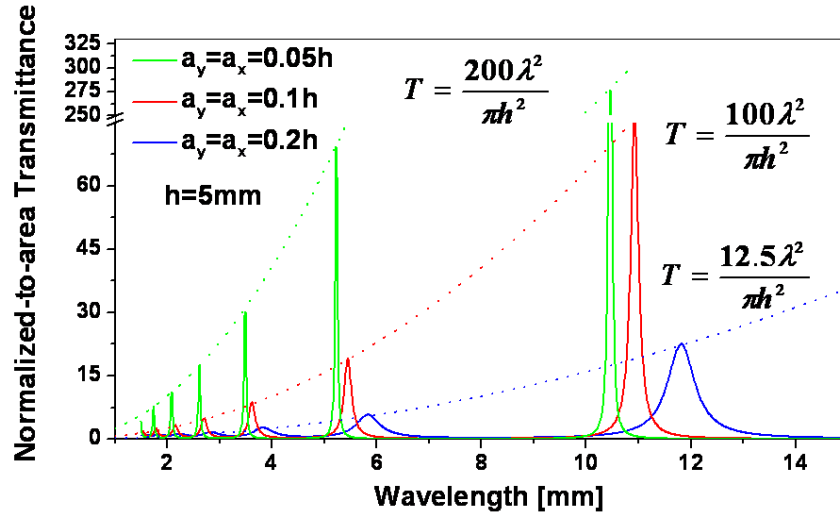


Figure 2.8: Transmittance spectra for single holes of three different geometries as given in the figure.

rise to a quadratic growth in the transmittance with respect to the wavelength:

$$T_{res}^{hole} = \frac{\lambda^2}{2\pi a_x a_y}. \quad (2.35)$$

In Fig. 2.8 where we have drawn the curves for continuous wavelength in Eq. (2.35) a good match with the peaks is evident for all three examples. In all cases this quadratic growth is clearly visibly, underlining the explicit difference between holes and slits with simple analytical expressions.

2.6 Transmission through a slit array

In this section we apply the theory derived to study the transmission properties on a simple structure, such as the initially proposed slit array. As has been mentioned in section 2.4, extensive work on sound transmission through periodic arrays of apertures has been elaborated in connection with sound sealing [85, 93]. In the pursuit of understanding the acoustical analogy of the EOT a quickly growing community has

emerged, dealing with theoretical but also experimental aspects on periodic structures. Slit arrays as the schematics in Fig. 2.1 depicts, have been fabricated out of solid steel or brass with typical geometries in the mm range. The designated PRB approximation along with the disregard of viscous losses has, as reported in several experimental works such as [90, 94], demonstrated to be a valid approximation in the high kHz to low MHz regime, when the structure is immersed in air or water. This fact also applies for the two dimensional structure which will be highlighted in a subsequent section. In these mentioned experiments, sound transmission proper-

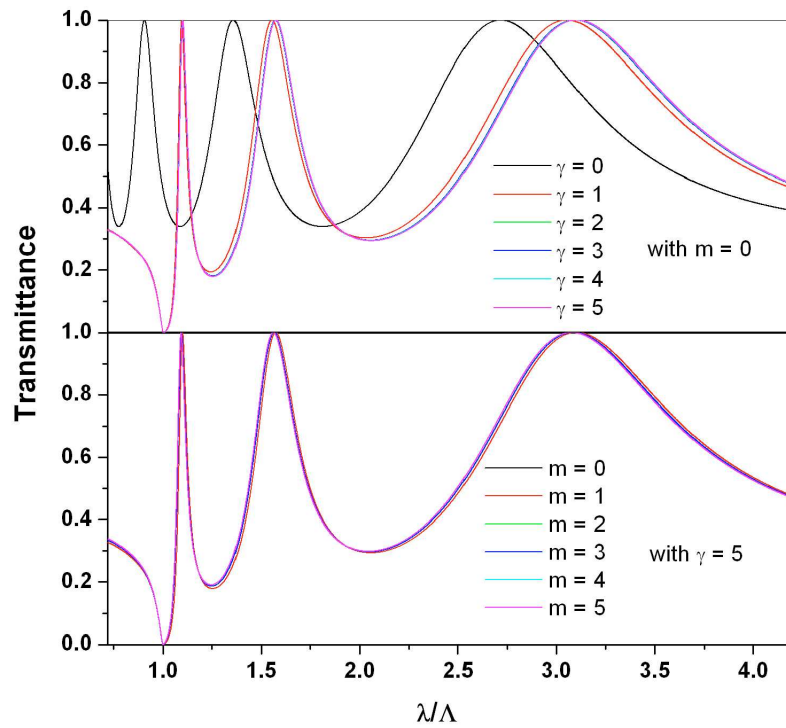


Figure 2.9: Convergence study with a normalized-to-unit cell transmittance spectrum for a slit array. The slit width $a = 0.3\Lambda$ whereas the slit array thickness $h = 1.4\Lambda$. The upper panel is for different number of diffraction orders at the fundamental waveguide mode ($m = 0$). Lower panel: Fixed number of diffraction orders ($\gamma = 0$) for different waveguide modes. The wavelength is scaled with the period Λ of the slit array.

ties solely controlled by geometrical parameters have been observed as we will see in

the following. Fig. 2.9 illustrates a convergence study on the transmission of sound through a subwavelength periodic slit array. Before getting into the details, the terms in Eq. (2.19) are highlighted:

$$I_m^0 = 2iY_{k_z^0}^I S_{0m} \quad (2.36)$$

$$G_m^V = \frac{Y_{q_z^m}^{II}}{\sin q_z^m h} \quad (2.37)$$

$$\epsilon_m = \frac{Y_{q_z^m}^{II}}{\tan q_z^m h} \quad (2.38)$$

$$G_{mm'} = i \sum_{\gamma=-\infty}^{\infty} Y_{k_z^\gamma}^{I/III} S_{\gamma m'} S_{\gamma m}^*. \quad (2.39)$$

Eqs. (2.36) in the inhomogeneous term of Eqs. (2.19) represents a function of sonic irradiation which basically is the overlap of the incident wave with the slit waveguide mode m . Eqs. (2.37,2.38) are related to wave motion within the slit by the waveguide eigenmode m which can be deduced from the system of equations, hence G_m^V is coupling the incident to the emerging field which pretty much is explained by the fact that this simple trigonometric function links the modal fields v_m and v'_m between each other. On the other hand, Eq. (2.38) describes the bidirectional wave motion within the slits, as this function both governs coupling between the input and the output sides in the positive z -direction but also in the negative direction. Finally, as it has already been mentioned before, the overlap function $G_{mm'}$ at either $z = 0$ or $z = h$ (refer to the admittance in Eq. (2.39) with corresponding index) reflects the radiation that the waveguide mode m is emitting into modes m' whilst being coupled to diffracted order γ . Having control over the entire system, the modal fields can be solved, followed by the evaluation of the amplitudes A_m, B_m which are further deduced in appendix A. Note that so far no further simplifications have been applied within this formalism, generally speaking; each individual layer properties

regarding the mass density and speed of sound are preserved, hence e.g. an gas/fluid filling or backing incorporated within the slit array is possible.

Accurate simulation of the current problem is a crucial theme, hence to that aim we highlight the dependence of both the number of waveguide modes and diffraction orders. Fig. 2.9 clearly shows that the specular mode ($\gamma = 0$), although not being convergent, already carries the characteristics peaks, that are found in the convergent case, ($\gamma = 5$). Remarkably by inspecting the lower panel in that figure, it becomes distinct that fields inside subwavelength apertures, to a quantitative and qualitative degree becomes convergent when only the fundamental waveguide mode, $m = 0$, is taken into account. This fact builds the very foundation on simplifying the problem by several means and providing analytical insight into the problem, which will be highlighted next. First, as of the absence of losses and the resonant interaction with the solid structure, all dimensions are scalable, hence, we have normalized all geometries to the period. Fig. 2.9 renders the appearance of a sharp drop in the transmission, exactly when the wavelength approaches the period $\lambda \sim \Lambda$. This feature (minima) is known as the Wood-Rayleigh anomaly which comes about when the diffraction order become grazing, in other words, when the diffracted waves are tangential to any kind of holey surface or groove grating consisting of periodic indentations. This appears when a diffraction order $(\pm 1, 0)$ becomes evanescent ($k_z = 0$). The admittance in Eq. (2.39) has a singularity at exactly this location making $G_{mm'}$ diverge at this Wood-Rayleigh anomaly (section 2.7 for more details). This minimum is accompanied by a strong peak arising slightly above the period ($\lambda \sim \Lambda$), which is connected to the excitation of surface modes. How this and all the other resonant peaks seen in Fig. 2.9 are explained with mathematical words, becomes transparent if we apply the knowledge gained from the convergence study, into Eqs. (2.19). In the following we shall derive an expression that governs the type of wave the present 1D system can sustain. As already mentioned, the simplest structure which comes the closest to a slit array is nothing but a groove grating which carries

the same type of resonances like the present structure. Structured PEC surfaces are known to support the existence of the so-called spoof surface plasmon polaritons (SPPs) or designer plasmons [28, 29]. Kelders et al. have both experimentally and theoretically shown that a 1D array of grooves that are drilled into a PRB made out of steel, supports the formations of surface waves for sound. Although the surface of a perfect rigid body presents no surface modes, when it is perforated with a periodic array of indentations, surface modes are built up. This finding has been reported by Kelders and co-workers [95, 96]. If the plate is drilled with a 1D array of slits, these

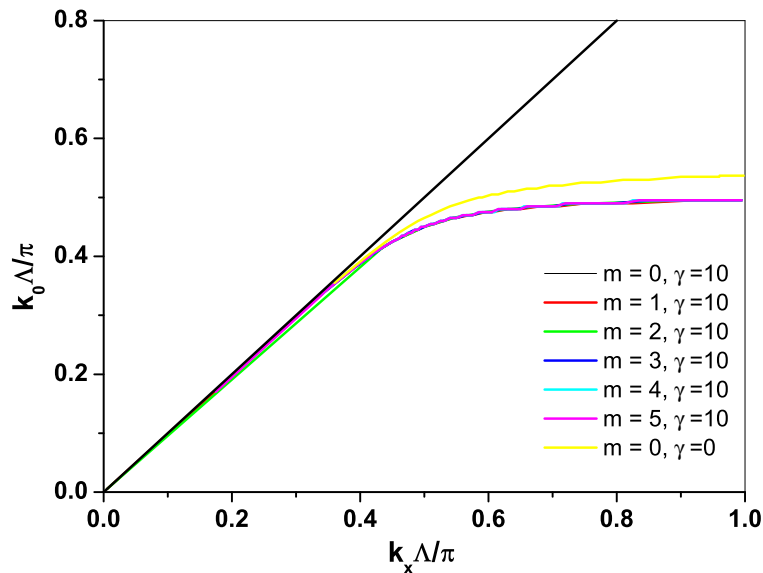


Figure 2.10: Convergence study with a dispersion relation plot for a groove grating. The slit width $a = 0.3\Lambda$ whereas the slit array thickness $h = 1.4\Lambda$. For a fixed number of diffraction orders convergence is sought for waveguide modes up to $m = 5$.

acoustic surface modes are always strongly coupled via the waveguide modes in the slits. The result is a mode which is guided along the plate and decays outside it, i.e. an acoustic guided mode, or in simple terms, an ASW. The theoretical formalism previously described can be used to calculate the dispersion relation (frequency

versus k_x) of these acoustic guided modes. The formalism with Eqs. (2.19) can straightforwardly be applied to groove gratings by rejecting the homogeneous term as of no wave emerging interface, and cancelling the terms responsible for the external irradiation I_m^0 as only bound surface states are sought, such as G_m^V that can't provide interface coupling to the output side due to the absence of perforations:

$$(G_{mm} - \epsilon_m)v_m + \sum_{m' \neq m} G_{mm'}v_{m'} = 0. \quad (2.40)$$

Within the first Brillouin zone, Fig. 2.10 illustrates the convergent surface bands that lie in the evanescent ($k_x > k_0$) regime of the dispersion relation. Again the fundamental waveguide mode is a very good approximation, though the specular mode ($\gamma = 0$) seems only to have good accuracy in the nearest vicinity of the sound line ($k_0 = k_x$) while for lower wavelength, only a qualitative but certainly physical meaningful picture is provided. Therefore it seems, that a groove grating in its simplest approximation, may tell us what physical features are carried in the transmission study for an array of slits provided that:

$$\boxed{\lambda > \Lambda \gg a} \quad (2.41)$$

is fulfilled. Within this inequality, we can further reduce both Eq. (2.12) and Eq. (2.40) with $m = \gamma = 0$ into:

$$R_0 = \frac{1 + i \frac{k_0}{k_z} S_{00}^2 \tan k_0 h}{1 - i \frac{k_0}{k_z} S_{00}^2 \tan k_0 h} \quad (2.42)$$

and

$$G - \epsilon = 0 \quad (2.43)$$

respectively ($G_{00} \rightarrow G$), with the overlap for very narrow slits (Eq. (2.41)), $S_{00}^2 \approx \frac{a}{\Lambda}$. Whether the divergence in Eq. (2.42) is sought, or some simple algebraic manipulation is employed on Eq. (2.43), both procedures place us to the same approximated dispersion relation for bound surface states, $k_z = i\sqrt{k_x^2 - k_0^2}$:

$$\boxed{k_x = k_0 \sqrt{1 + \frac{a^2}{\Lambda^2} \tan^2 k_0 h}}, \quad (2.44)$$

being the $m = \gamma = 0$ band in Fig. 2.10. This expression for the geometry induced surface modes (for cylindrical structures see Chapter 3) plays a key-role in understanding the resonant transmission peaks that can be observed in Fig. 2.9. To illustrate why we concentrated on a groove grating, let us come back to the slit array case and finally simplify the system of equations in Eqs. (2.19) into ($m = 0$):

$$\boxed{\begin{aligned} (G - \epsilon)v - G^V v' &= I^0 \\ (G - \epsilon)v' - G^V v &= 0 \end{aligned}}. \quad (2.45)$$

In the case of subwavelength slits where we seek bound modes, the system of Eqs. (2.45) is now driven by an evanescent wave of momentum k_x larger than k_0 . In this particular case where diffraction effects are neglected, G in (2.45) is a real magnitude, $G = \frac{a}{\Lambda} \frac{k_0}{\sqrt{k_x^2 - k_0^2}}$, and the denominator can be exactly zero at the condition:

$$\frac{\sqrt{k_x^2 - k_0^2}}{k_0} = \frac{a}{\Lambda \cos k_0 h} \pm 1 \quad (2.46)$$

where the sign (+) must be taken when $\sin k_0 h > 0$ and sign (−) when $\sin k_0 h < 0$. Eq. (2.46) gives the dispersion relation of the acoustic guided modes for a 1D periodic array of slits in the effective medium limit ($\lambda \gg \Lambda, a$). Introducing some new geometries as illustrated in the upper panel of Fig. 2.11, we see the same kind of shape in the transmittance spectra when comparing to Fig. 2.9. When the overall plate thickness h of the slit array is increased, apart from the peak close to the period that is associated to the bound surface modes, we observe an increase in the number of wide banded peak, fulfilling the FP condition ($\sin k_0 h = 0$, $\lambda = \frac{2h}{1}, \frac{2h}{2}, \frac{2h}{3} \dots \frac{2h}{m}$), which basically is due to an acoustical excitation of standing waves within each slits. In Fig. 2.11 we show the dispersion relation from Eq. (2.46) (white lines in the right part of the panel) for the geometrical parameters of the structure analyzed with $h = 0.9\Lambda$. Two regimes are clearly distinguishable: a linear part close to the sound line ($\omega = ck_x$) and flat parts that are associated with the FP cavity resonances ($\sin k_0 h = 0$). The important point to realize is that if $\lambda < 2\Lambda$, these guided

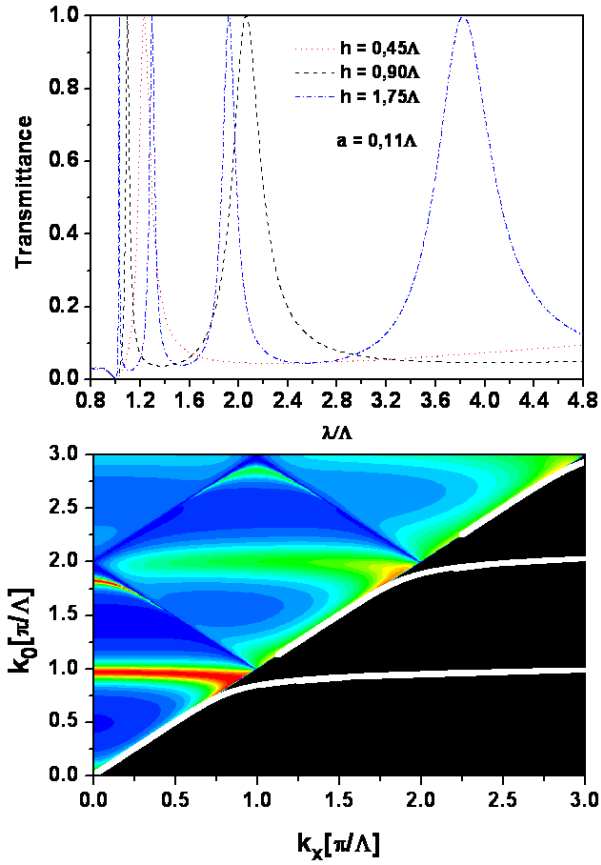


Figure 2.11: Normalized-to-unit-cell transmittance spectra for a normal incident plane wave impinging on an array of slits with geometries as illustrated. Lower panel illustrates a transmittance and an acoustic guided mode dispersion relation for the structure of thickness $h = 0.9\Lambda$, obtained with Eq. (2.46).

modes become leaky and can be excited by an impinging propagating plane wave. The connection between these leaky guided modes and the transmittance peaks is highlighted in the same figure. In the left part of this panel transmittance versus wavenumber and k_x within the *sound cone* is rendered (solved including diffraction). It is clear that the location of transmittance peaks can be extracted by just folding the guided modes bands inside the *sound cone*. We have checked when comparing the band diagrams for groove gratings and slit arrays, that they are very similar. There are slight discrepancies in the flat part of the curves, illustrating different binding

characteristics but in both cases, within the long wavelength limit approximation, Eqs. (2.41), both cases yield remarkable insight into the physics involved despite of the absence of diffraction effects which involves the possibility for Bragg folding. The bound surface states or guided modes as has been highlighted here are not truly surface modes as the two surfaces of the plate are always connected via a propagating wave. This fact provokes that acoustic guided modes always hybridize strongly with the FP resonances associated with slit cavities. The flatness of the curves linked to FP modes, also illustrates the angle independence of that particular mode. In other words, unlike the resonance closely located to the period, when varying the angle of incidence ϕ for sound impinging on the structure, enhanced transmission linked to those standing wave modes, prevails. In order to confirm the reasoning on the resonant nature regarding the enhanced acoustical transmission through slits, we have conducted pressure field computation for three different spectral locations, corresponding to the peaks seen in the upper panel of Fig. 2.12, with geometries tuned to exhibit those three features. From the three lowest panels, the hybrid nature of ASWs and FP standing waves is unambiguous observable. The time averaged acoustic pressure $|p|$ mapped within the unit cell of the slit-array at a wavelength $\lambda = 2.5\Lambda$ illustrates the distinct occurrence of a high pressure concentration of lowest order $m = 1$ solely inside the slit, which is the first Fabry-Perot resonance excited, exhibiting one node at $z = \frac{h}{2}$. When moving to lower wavelengths towards the period, the number of nodes and antinodes increases ($m = 2, 3$) corresponding to $\lambda = 1.3\Lambda$, $\lambda \approx 1.0\Lambda$ respectively. At a wavelength close to the period of the slit array $\lambda \approx \Lambda$, one observes an increasing confinement along the structure input and output surfaces, which clearly indicated the correspondence to ASW coupling.

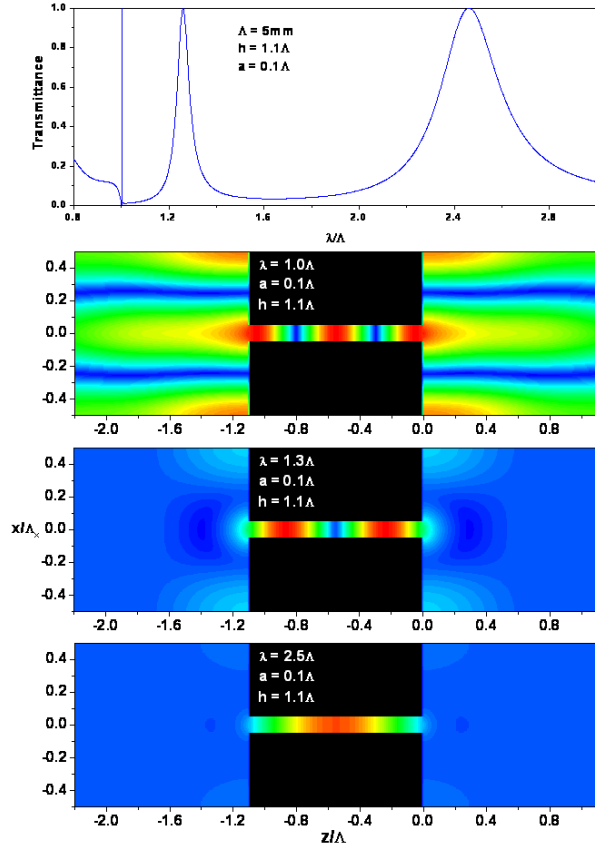


Figure 2.12: Normalized-to-unit-cell transmittance spectra for a structure with geometries given in the figure. The lower panels plot the modulus of the pressure fields inside the unit-cell of the structure, calculated at the transmission peaks located at $\lambda \sim 1.0\Lambda$, $\lambda = 1.3\Lambda$ and $\lambda = 2.5\Lambda$. (Red: Max, Blue: Min).

2.7 Transmission through a hole array

In this section we wish to awake the readers attention on the 2D analogy of the previous study: sound transmission through subwavelength hole arrays. As has already been hinted at throughout the latter section, the very fundamental physics is not differing significantly from the 1D case. From fundamental theoretical acoustics, it is known that with, e.g., rectangular waveguides, unlike for EM waves the fundamental cavity mode is always propagative. Recall waveguides for optical systems in

transmission lines, fibers and more, whether the guides are rectangular or cylindrical in shape, the lateral dimensions of the waveguides define the wavelength at which light can no longer propagate through the aperture. This wavelength is known as the cutoff wavelength λ_c . When the incident wavelength $\lambda > \lambda_c$ the transmission is exponentially small, characterizing the non-propagating regime [77]. Within those constraints we wish to demonstrate the acoustical analogy of the EOT through an array of subwavelength holes and by this show that transmission resonances prevails in the absence of a cutoff. In fact the acoustic transmission study through holes is to a great extent similar to the slit array case that was highlighted in the previous section and discussed in several works [90, 97, 98]. Those findings did not only demonstrate that sound always propagate inside holes, but Estrada et al. showed how diverse the problem is from EOT when elastic plate motions are excited. Let us initially start to indicate how the same formalism derived previously can be extended to 2D perfect rigid hole arrays. If again, the structure is split up into

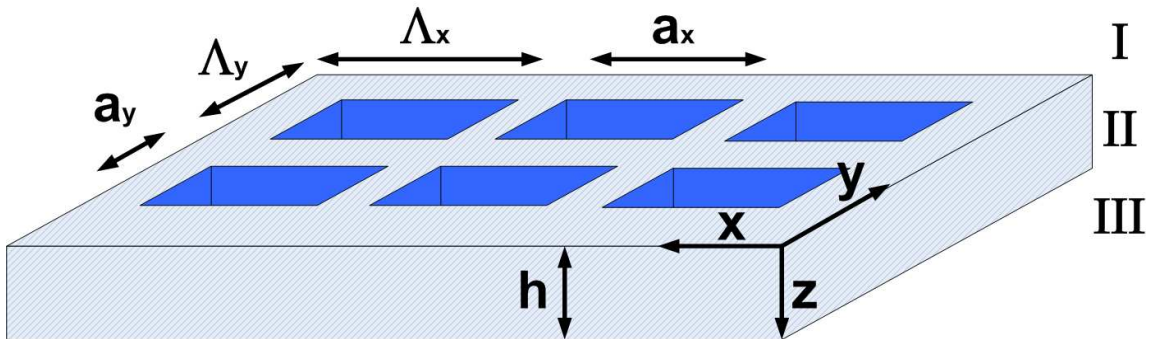


Figure 2.13: Schematics of a periodic array of holes, made out of a perfect rigid body, impenetrable for air-borne sound waves impinging on the structure.

the wave incident, hole, and wave emerging part as illustrated in Fig. 2.13, in the following it is displayed how the formalism with only minor modifications prevails.

In Region I the pressure field p is expressed in terms of real space Bloch waves:

$$\langle \mathbf{r}_{\parallel} | \mathbf{k}_{\parallel}^{\beta} \rangle = \frac{e^{i\mathbf{k}_{\parallel}^{\beta} \mathbf{r}_{\parallel}}}{\sqrt{\Lambda_x \Lambda_y}}, \quad (2.47)$$

with $\mathbf{r}_{\parallel} = (x, y)$ and the parallel momentum associated with Bloch mode β is expressed as $(\mathbf{k}_{\parallel}^{\beta})^2 = (\mathbf{k}_{\parallel}^{\gamma n})^2 = (k_x^n)^2 + (k_y^{\gamma})^2$ with discrete diffraction orders n and γ ($n, \gamma = -\infty, \dots, \infty$) comprising in-plane scattering where $k_x^n = k_x^0 + \frac{2\pi}{\Lambda_x} n$, $k_y^{\gamma} = k_y^0 + \frac{2\pi}{\Lambda_y} \gamma$, hence the z-component of the wave vector is nothing but:

$$k_z^{\beta} = \sqrt{(n_I k_0)^2 - (\mathbf{k}_{\parallel}^{\beta})^2}. \quad (2.48)$$

Already here we see that wave interaction taking place in In Region I , is not differing much from the slit array case, hence Eqs. (2.7) is slightly modified into the following:

$$\begin{aligned} |p^I(z)\rangle &= Y_{k_z^0}^I |\mathbf{k}_{\parallel}^0\rangle e^{ik_z^0 z} + \sum_{\beta=-\infty}^{\infty} R_{\beta} Y_{k_z^{\beta}}^I |\mathbf{k}_{\parallel}^{\beta}\rangle e^{-ik_z^{\beta} z} \\ |v_z^I(z)\rangle &= |\mathbf{k}_{\parallel}^0\rangle e^{ik_z^0 z} - \sum_{\beta=-\infty}^{\infty} R_{\beta} |\mathbf{k}_{\parallel}^{\beta}\rangle e^{-ik_z^{\beta} z}. \end{aligned} \quad (2.49)$$

Note also that now the orthogonal Bloch wave basis within the unit cell $\Lambda_x \times \Lambda_y$ is written as:

$$\langle \mathbf{k}_{\parallel}^{\beta} | \mathbf{k}_{\parallel}^{\beta'} \rangle = \int \langle \mathbf{k}_{\parallel}^{\gamma n} | \mathbf{r}_{\parallel} \rangle \langle \mathbf{r}_{\parallel} | \mathbf{k}_{\parallel}^{\gamma' n'} \rangle d\mathbf{r}_{\parallel} = \delta_{\gamma\gamma'} \delta_{nn'}. \quad (2.50)$$

In what follows we demonstrate that the waveguide modes within a subwavelength hole aperture, for the acoustical case significantly is different when comparing to the optical case. As has already been mentioned before, the presence of a cutoff frequency is manifested by the dominant fundamental waveguide mode as it is the least strongly decaying wave surrounded by PEC interfaces, hence for TE (transverse electric) polarized modes it becomes $q_z = \sqrt{\varepsilon_h k_0^2 - \pi^2/a^2}$, with ε_h being the permittivity within the hole and the cutoff wavelength $\lambda_c = 2\sqrt{\varepsilon_h} a$. Acoustical eigenmodes within a general cavity consisting of perfect rigid walls can be expressed with the following spatial eigenmodes comprising parallel momenta:

$$\langle \mathbf{r}_{\parallel} | \alpha \rangle = \sqrt{\frac{(2 - \delta_{0m})(2 - \delta_{0l})}{a_x a_y}} \cos q_x^m \left(x + \frac{a_x}{2}\right) \cos q_y^l \left(y + \frac{a_y}{2}\right), \quad (2.51)$$

where $(\mathbf{q}_{\parallel}^{\alpha})^2 = (\mathbf{q}_{\parallel}^{ml})^2 = (q_x^m)^2 + (q_y^l)^2 = \pi^2(\frac{m^2}{a_x^2} + \frac{l^2}{a_y^2})$ and as a results of this, the wave vector parallel oriented to the holes reads $q_z^{\alpha} = \sqrt{(n_{II}k_0)^2 - (\mathbf{q}_{\parallel}^{\alpha})^2}$. Here it is clear that the fundamental waveguide mode in the absence of losses never experiences attenuation; the wave is always propagative. The pressure and the z-component of the velocity within a hole, therefore reads as follows:

$$\begin{aligned} |p^{II}(z)\rangle &= \sum_{\alpha} Y_{q_z^{\alpha}}^{II} (A_{\alpha} e^{iq_z^{\alpha} z} + B_{\alpha} e^{-iq_z^{\alpha} z}) |\alpha\rangle \\ |v_z^{II}(z)\rangle &= \sum_{\alpha} (A_{\alpha} e^{iq_z^{\alpha} z} - B_{\alpha} e^{-iq_z^{\alpha} z}) |\alpha\rangle, \end{aligned} \quad (2.52)$$

now with the basis function:

$$\langle \alpha | \alpha' \rangle = \int \langle \mathbf{q}_{\parallel}^{ml} | \mathbf{r}_{\parallel} \rangle \langle \mathbf{r}_{\parallel} | \mathbf{q}_{\parallel}^{m'l'} \rangle d\mathbf{r}_{\parallel} = \delta_{mm'} \delta_{ll'}. \quad (2.53)$$

Apart from the modified wave vector and admittance, the field in the wave emerging side of region *III* remains equally as stated in Eqs. (2.9):

$$\begin{aligned} |p^{III}(z)\rangle &= \sum_{\beta=-\infty}^{\infty} Y_{k_z^{\beta}}^{III} T_{\beta} |\mathbf{k}_{\parallel}^{\beta}\rangle e^{ik_z^{\beta}(z-h)} \\ |v_z^{III}(z)\rangle &= \sum_{\beta=-\infty}^{\infty} T_{\beta} |\mathbf{k}_{\parallel}^{\beta}\rangle e^{ik_z^{\beta}(z-h)}. \end{aligned} \quad (2.54)$$

Now as all fields are expressed throughout all space, the modal expansion technique can be applied appropriately just in a similar way as has been employed in the 1D case. Continuity of the pressures is preserved through the holes, whereas the velocity is continuous through out the 2D unit cell. After projecting the modes all terms and set of equations are gathered into an equivalent system of equations, differing only slightly from Eqs. (2.19):

$$\boxed{\begin{aligned} (G_{\alpha\alpha} - \epsilon_{\alpha})v_{\alpha} + \sum_{\alpha' \neq \alpha} G_{\alpha\alpha'} v_{\alpha'} - G_{\alpha}^V v'_{\alpha} &= I_{\alpha}^0 \\ (G_{\alpha\alpha} - \epsilon_{\alpha})v'_{\alpha} + \sum_{\alpha' \neq \alpha} G_{\alpha\alpha'} v'_{\alpha'} - G_{\alpha}^V v_{\alpha} &= 0 \end{aligned}}. \quad (2.55)$$

With the new overlap integral $S_{\beta\alpha} = \langle \mathbf{k}_{\parallel}^{\beta} | \mathbf{q}_{\parallel}^{\alpha} \rangle = \int \langle \mathbf{k}_{\parallel}^{\beta} | \mathbf{r}_{\parallel} \rangle \langle \mathbf{r}_{\parallel} | \mathbf{q}_{\parallel}^{\alpha} \rangle d\mathbf{r}_{\parallel}$, the 2D constituents from Eqs. (2.55) are:

$$I_{\alpha}^0 = 2iY_{k_z^0}^I S_{0\alpha'} \quad (2.56)$$

$$G_{\alpha}^V = \frac{Y_{q_z^{\alpha}}^{II}}{\sin q_z^{\alpha} h} \quad (2.57)$$

$$\epsilon_{\alpha} = \frac{Y_{q_z^{\alpha}}^{II}}{\tan q_z^{\alpha} h} \quad (2.58)$$

$$G_{\alpha\alpha'} = i \sum_{\beta=-\infty}^{\infty} Y_{k_z^{\beta}}^{I/III} S_{\beta\alpha'} S_{\beta\alpha}^*. \quad (2.59)$$

The overlap integrals can be found in the appendix A and as in the 1D case, all expansion coefficients such as R_{β} and T_{β} and the modal fields v_{α}, v'_{α} can be obtained when solving the system of Eqs. (2.55), describing sound being funnelled through a hole array. Before a phenomenological study is initiated, it would be convenient to strive for a simplified model, in other words, checking for a precise convergence given by the fundamental mode approximation. Fig. 2.14 shows transmittance spectra of sound penetrating a hole array which have converged. In here it is shown that only a few waveguide modes and diffraction orders are sufficient in order to obtain good accuracy. In this particular case of certain chosen geometries, we see that the fundamental waveguide mode, even though not accurate, already carries all physical important properties that one would expect from the knowledge gained from the slit array study. In this sense, qualitative one observes a similar spectra, but let us define this one precise. We now choose a set of geometries that are leading to a valid and precise approximation by means of the fundamental hole waveguide mode (long wavelength limit) and demonstrate by this how to explore the resonant attributes that are giving rise to transmission peaks. As the FP type resonance ($\lambda = \frac{2h}{m}$) plays a crucial role in transferring sound efficiently through structures consisting

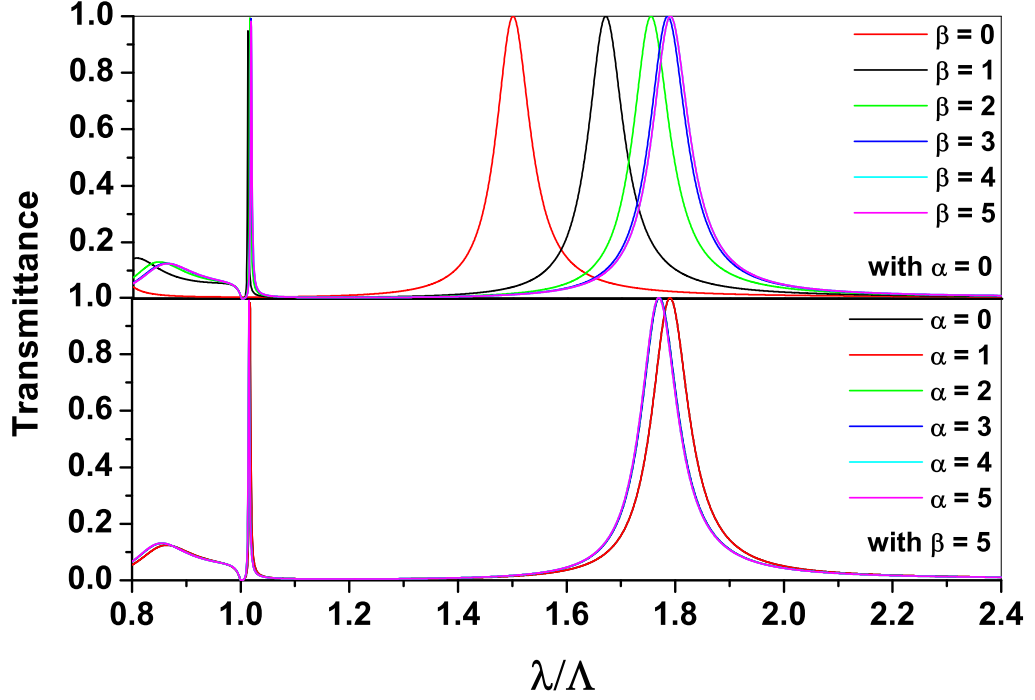


Figure 2.14: Convergence study of normalized-to-unit cell transmittance spectra for a hole array. The hole square width $a_x = a_y = 0.2\Lambda$ whereas the thickness $h = 0.75\Lambda$. The upper panel represents different number of diffraction order at the fundamental waveguide mode $\alpha = 0$ ($m, l = 0, 0$). Lower panel: Fixed number of diffraction orders $\beta = 5$ ($\gamma, n = 5, 5$) for different waveguide modes.

of subwavelength holes, we know that the thickness of the structure determines the tuneability with ASWs and consequently the transmittance itself. When reformulating the system of Eqs. (2.55) into the long wavelength limit by taking into account only the fundamental waveguide mode ($\alpha = 0$):

$$(G - \epsilon)v - G^V v' = I^0, \quad (G - \epsilon)v' - G^V v = 0, \quad (2.60)$$

these two equations of two unknowns can be employed to find the non-trivial solutions, by taking the determinant of the matrix (non-indexed functions means $\alpha = 0$).

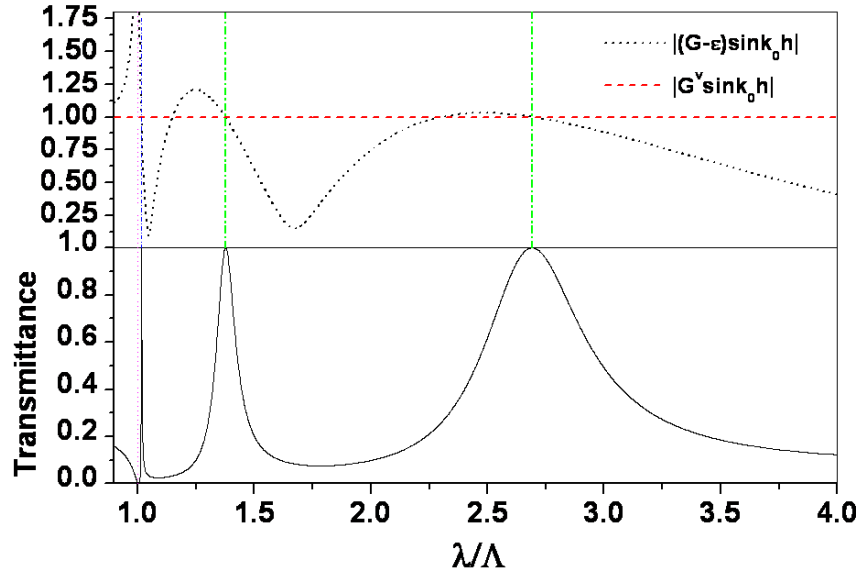


Figure 2.15: Transmittance spectra for an array of holes and the locations of the non-trivial solutions for a structure of thickness $h = 1.15\Lambda$ and a square hole of size $a_x = a_y = 0.15\Lambda$

This leads to the following expression $|G - \epsilon| - |G^V| = 0$ which determines all locations giving rise to an enhanced acoustical transmission. Now we immediately see how this condition when being fulfilled, determines the acoustical transparency at resonance making the modal velocities $|v| = |v^V|$ equal. In order to normalize the determinant we have scaled it with $\sin k_0 h$ as illustrated in Fig. 2.15. In this context, at a wavelength matching the period $\lambda = \Lambda$ we see the first similarity to the 1D counterpart, the slit array. The Wood-Rayleigh anomaly, which sets in when the diffracted waves are tangential to the holey surface due to diffraction order $(\pm 1, 0)$ becoming evanescent ($k_z = 0$), is understood with Eq. (2.59) which has a divergence due to the singularity of the admittance, that clearly can be seen in Fig. 2.15, marked with a magenta vertical dotted line. The determinant is fulfilled at all intersecting locations between the functions $|G - \epsilon|$ and $|G^V|$. Care has just to be taken with the normalization with $\sin k_0 h$, giving rise to another non-resonant

root. The blue vertical dotted line, is at a wavelength slightly larger than the period and stems from the excitation of ASWs, whereas the other features, marked with green lines, underpins the standing wave excitation of order $m = 1$ and $m = 2$ at locations $\lambda_{FP} = 2h$ and $\lambda_{FP} = h$ respectively. Intuitively one can hereby see,

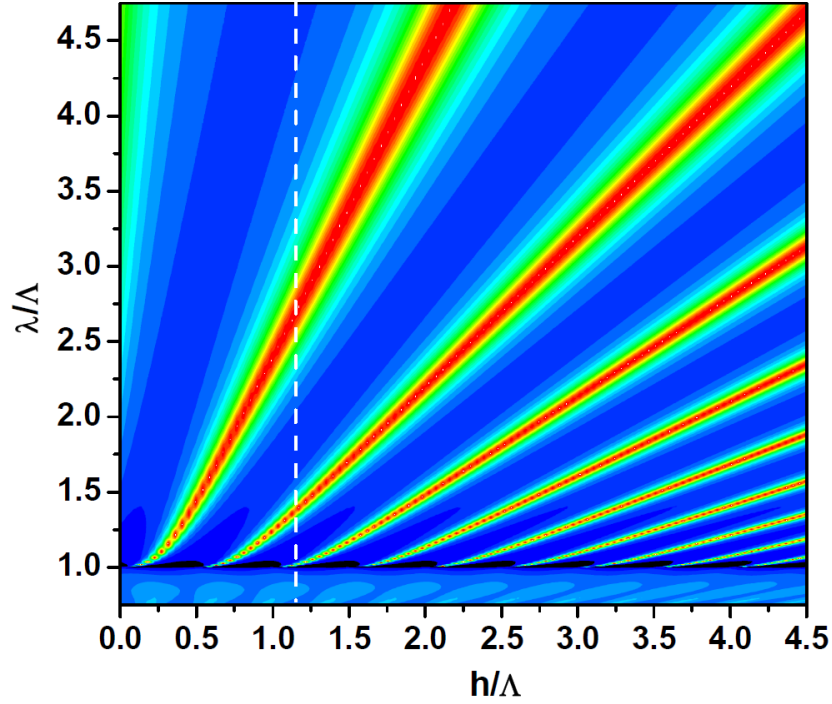


Figure 2.16: Spectral transmittance contour for an array of holes as a function of the metal thickness, for a structure with square holes of size $a_x = a_y = 0.15\Lambda$. The vertical white dashed line, corresponds to one example shown in Fig. 2.15.

in the absence of a cutoff within the holes, transmission of sound through a hole array is in a distinct way reminiscent to the slit array case. Through this current study, but also for the slit array case, we have seen how the variation of the plate thickness h can tune the resonances of the holey structures, more precisely, the hybrid nature of FP and ASW modes. Fig. 2.16 shows a transmission contour (red: max, blue: min) plot where the thickness is varied over the entire frequency

spectrum. At this figure, a white line is drawn, which is resembling the example that has been depicted in Fig. 2.15, clearly the minimum that is accompanied by a transmission maximum close to the period of the structure, and the two FP resonances are following this line. Note that the appearance of the peak associated with the excitation of ASWs is very sensitive to the thickness, because when concentrating at the location of the white line, and slightly varying (\pm) the thickness h , it is to be observed that the peak either merges with an even or odd FP mode. This sensitivity demonstrates the complex interplay between the FP resonances and the resonant features appearing close to $\lambda \sim \Lambda$ in hole arrays. Further increasing the thickness by many periods, clearly the growth in the number of resonances appears. In the following we wish to verify the resonance mechanism involved by means of pressure field plots $|p|$ in the xy -plane. Fig. 2.17 highlights three pressure maps corresponding to the full transmission peaks, with the geometries as in Fig. 2.15, for all cases evaluated at the wave emerging interface, $z = h$ (the white dotted squares, corresponds to the

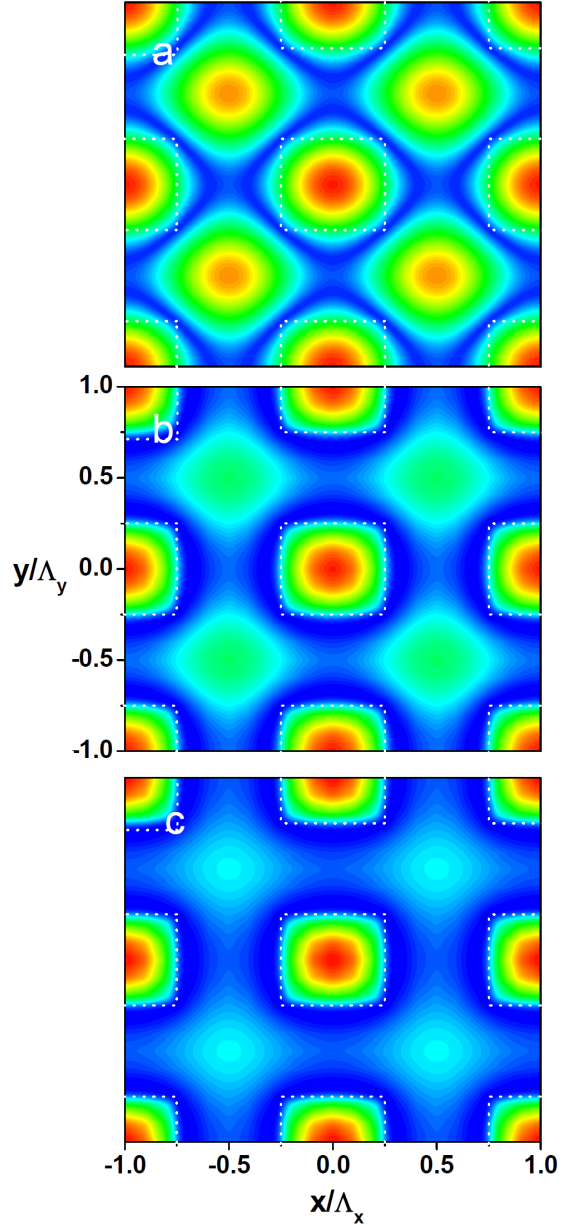


Figure 2.17: Pressure field maps ($z = h$) for a hole array with the geometries specified in Fig. 2.15, plotted at the transmission peaks, spectrally located at: a) $\lambda = 1.05\Lambda$, b) $\lambda \simeq 1.35\Lambda$ and b) $\lambda = 2.70\Lambda$.

quadratic drilled holes $a = a_x = a_y$). As the figure captions declares, following from the top till the bottom, panel (a) corresponds to the pressure field for a wavelength close to the period, whereas panel (b) and panel (c) illustrate pressure mappings at the 2nd and the 1st FP mode respectively. Recalling Fig. 2.12 from section 2.6, it was displayed how the hybridization of ASW (or guided modes) and FP modes took place, by means of observing the field distribution in the sagittal (xz) plane. It was clear, that the closer the wavelength approaches the period, the higher the degree of hybridization. In other words, around $\lambda \approx \Lambda$, the coupling of pure ASWs and higher ordered standing waves within the slit is evident, whereas this coupling becomes weaker when moving away from that wavelengths. By several means, it has so far been stated that the acoustical transmission phenomena through slit arrays own similar properties as sound being funnelled through hole arrays. Clearly we showed how the sensitivity of the narrow peaked resonance of wavelength around the period ($\lambda \approx \Lambda = \Lambda_x = \Lambda_y$), can be controlled by the thickness that in turn dominates the standing wave modes inside the holes. In a similar way as was presented in the previous section, we could illustrate a dispersion relation, but as of great similarities in the resonance mechanisms, we demonstrate those features by the pressure field mapping in the xy-plane. Below the holes in all three cases, we see a high intensity of sound, confirming that within the holes, FP resonances are excited. It has been checked, whether slit or hole arrays are under study, in the sagittal plane the field always exhibits an integer number of nodes (FP order). Conclusively, out of Fig. 2.17a, it now becomes evident that either for slit or hole arrays, the excitation of surface modes (panel (a) clearly depicts high pressure concentration between the holes at the perfect rigid surface, whereas the other panels illustrate a high field localization within the apertures only) plays an intrinsic role in squeezing sound efficiently through holes that are much smaller compared to the wavelength.

2.8 Transmission through a single slit surrounded by corrugations

In this section we present another analogy from the field of optics and demonstrate how the diffraction of sound in all directions when it emerges from a subwavelength aperture can be controlled. In 2002, 4 years after the seminal work by Ebbesen and co-authors, new routes for controlling the flow of EM waves were placed in the spot light [99]. According to standard diffraction theory, apertures such as slits, much smaller than the wavelength of light transmit very poorly and diffract light in all directions uniformly. These two properties, transmission and diffraction are considered fundamental constraints in manipulating light on a very small scale for technological purposes. It has been shown that the patterning of the wave impinging and emerging interfaces by a finite periodic set of shallow grooves yields an enhancement of the transmission, but more importantly, the diffracted radiation could be compressed into a narrow beam. In other words, light could be channelled in a well defined direction as a collimated beam. This has both been demonstrated for a 3D structure, the so-called bull's eye, but also for a single slit surrounded by shallow corrugations [100–102]. Fig. 2.18 is the structure under the present examination devoted to the

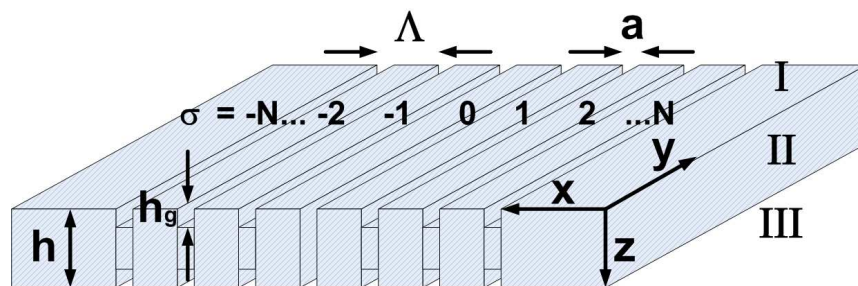


Figure 2.18: Schematics of a single slit surrounded by finite corrugations, made out of a perfect rigid body, impenetrable for air-borne sound waves impinging on the structure.

study of collimation and enhanced transmission of sound waves. This structure is basically a modification of Fig. 2.2 as apart from the present single isolated slit, furthermore the PRB is textured by indentations at the upper and the lower interface. In order to study the sound phenomena theoretically, to a great extent, we can deploy the theory derived in section 2.4, but here we need to introduce some modifications, accounting for the rectangular groove cavity modes and their spatial phase. Also in this example, we will neglect higher order waveguide modes within the slit (and cavities), due to the small size compared to the wavelength. The wave impinging and emerging side remains unaffected but region *II* containing indentations σ or σ' is split up into the input, central and output sub-region. This is now being presented in the following way with $m = 0$ and the same fluid in all layers:

The cavity mode at the input side reads:

$$\begin{aligned} |p^{in}(z)\rangle &= \sum_{\sigma} (A_{\sigma}e^{ik_0z} + B_{\sigma}e^{-ik_0z})|0\rangle \\ |v_z^{in}(z)\rangle &= \sum_{\sigma} (A_{\sigma}e^{ik_0z} - B_{\sigma}e^{-ik_0z})|0\rangle \end{aligned} \quad (2.61)$$

if $|x - x_{\sigma}| < \frac{a}{2}$ otherwise zero where $x_{\sigma} = \sigma\Lambda$ is the phase, depicting the discrete groove locations. The only location where sound can propagate through the entire structure is within the central slit, which is when $\sigma = 0$:

$$\begin{aligned} |p^{centr}(z)\rangle &= (A_0e^{ik_0z} + B_0e^{-ik_0z})|0\rangle \\ |v_z^{centr}(z)\rangle &= (A_0e^{ik_0z} - B_0e^{-ik_0z})|0\rangle, \end{aligned} \quad (2.62)$$

and subsequently emerge over the output rectangular grooves:

$$\begin{aligned} |p^{out}(z)\rangle &= \sum_{\sigma} (C_{\sigma}e^{ik_0(z-h)} + D_{\sigma}e^{-ik_0(z-h)})|0\rangle \\ |v_z^{out}(z)\rangle &= \sum_{\sigma} (C_{\sigma}e^{ik_0(z-h)} - D_{\sigma}e^{-ik_0(z-h)})|0\rangle. \end{aligned} \quad (2.63)$$

At this stage we will not go through all the details of the matching procedure of the modes, as it would not differ much from the latter case. We would end up with a set of linear continuity equations, projecting the fundamental cavity mode in groove

σ over diffraction orders to the fundamental cavity mode inside groove σ' . In order to gather the entire continuity representation into a linear system of equations, we need to set some basic definitions at first place. To do so one has to incorporate the phase of the structure (see Eq. (A.8) from appendix A), in order to distinguish the modal field above the slit or above the grooves.

*For $\sigma \neq 0$, at the grooves:

At the bottom of the groove ($h_g = h_{in}$) at the impinging side, the velocity v^{in} vanishes due to the perfect rigid wall that the pressure field encounters, hence with $\psi_{in} = e^{2ik_0h_{in}}$ the wave amplitudes read:

$$B_\sigma = \psi_{in}A_\sigma. \quad (2.64)$$

This statement is very useful in order to write down the identities for the modal field at the input side:

$$\begin{aligned} v_\sigma &= A_\sigma - B_\sigma \\ \epsilon_{in}v_\sigma &= A_\sigma + B_\sigma. \end{aligned} \quad (2.65)$$

Similar we can unravel expressions for the modal velocity at the emerging side with $\psi_{out} = e^{-2ik_0h_{out}}$ inside the groove ($h_g = h_{out}$):

$$D_\sigma = \psi_{out}C_\sigma \quad (2.66)$$

From this we also deduce the definitions for the modal velocity field at the output side:

$$\begin{aligned} v'_\sigma &= C_\sigma - D_\sigma \\ \epsilon_{out}v'_\sigma &= C_\sigma + D_\sigma. \end{aligned} \quad (2.67)$$

ϵ_{in} and ϵ_{out} are equivalent to the bouncing back and forth of acoustic wave motion inside grooves placed either at the input or output side respectively, as described, e.g., in Eq. (2.26).

*For $\sigma = 0$, at the slit:

The central slit is reminiscent to the conventional case where we impose continuity through an aperture. At that spatial location we match the groove cavity with the slit waveguide modes and together with the definitions:

$$\begin{aligned} v_0 &= A_0 - B_0 \\ v'_0 &= D_0 - C_0, \end{aligned} \tag{2.68}$$

we hereby illustrate that the central slit, unlike for $\sigma \neq 0$, couples the incident to the emerging field that is occurring via the interface coupling function G^V :

$$\begin{aligned} A_0 + B_0 &= \epsilon_0 v_0 + G^V v'_0 \\ D_0 - C_0 &= \epsilon_0 v'_0 + G^V v_0. \end{aligned} \tag{2.69}$$

With all those terms defined in Eqs. (2.65-2.69) we can conclude the modal expansion by gathering all terms into the following system:

$$\boxed{\begin{aligned} (G_{\sigma\sigma} - \epsilon_{in})v_\sigma + \sum_{\sigma' \neq \sigma} G_{\sigma\sigma'} v_{\sigma'} - \delta_{\sigma 0} G^V v'_0 &= I_\sigma^0 \\ (G_{\sigma\sigma} - \epsilon_{out})v'_\sigma + \sum_{\sigma' \neq \sigma} G_{\sigma\sigma'} v'_{\sigma'} - \delta_{\sigma 0} G^V v_0 &= 0 \end{aligned}}, \tag{2.70}$$

with:

$$G^V = \frac{1}{\sin k_0 h} \tag{2.71}$$

$$\epsilon_{in} = \frac{1}{\tan k_0 h_{in}} \tag{2.72}$$

$$\epsilon_{out} = \frac{1}{\tan k_0 h_{out}} \tag{2.73}$$

$$\epsilon_0 = \frac{1}{\tan k_0 h}. \tag{2.74}$$

The irradiation term I_σ^0 and the overlap functions $G_{\sigma\sigma'}$ are similar to the ones derived in the previous section, now just containing a phase with regards to indentation

σ (see appendix A). We start out with analysing the influence of having surface corrugations at the input-, output or both input/output-sides of the plate, on the transmittance $T(\lambda)$. In all cases we are going to restrict the calculations to normal incident radiation on an infinite plate consisting of a finite number of grooves with period Λ . For all cases, we have compared all transmittance calculations to the one of a plate without corrugations at both sides, which is nothing but the structure presented in section 2.4. Initially though, we like to underline how to tune the resonances supported by the slit surrounded by indentations. Fig. 2.19 shows results of

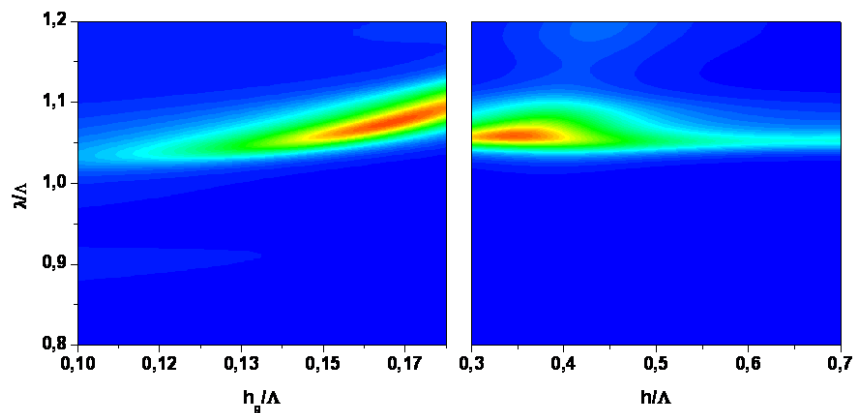


Figure 2.19: Normalized-to-area transmittance contour for the optimization of a single slit surrounded by corrugations. Normalized to the period Λ , the slit and groove width is $a = 0.08\Lambda$, with optimized overall plate thickness $h = 0.37\Lambda$ and groove depth $h_g = 0.17\Lambda$. (Red: Max, Blue: Min).

a kind of self-consistent optimization, when the depth of the shallow indentations h_g and the overall plate thickness h are varied. Fig. 2.19 are basically narrow windows of the optimised case, but in the following we are going to highlight the three main mechanisms to tune the structure. For a full graphical representation one should refer to [101] for the optical analogy where the optimum is based on the same algorithm.

*Slit waveguide modes, $\lambda \approx 2h$:

The first component is governed by the thickness of the structure and has been derived in section 2.4, which is the excitation of FP resonances in the isolated slit. Later we will see that the introduction of indentations at the output side of the plate does not affect these FP modes significantly.

*Groove cavity modes, $\lambda \approx 4h_g$:

In order to boost sound through the central slit ($\sigma = 0$) mediated by the surface corrugations, obviously v_0 in Eq. (2.70) must be large, which is provided with large v_σ . For large values of v_σ we can write : $(G_{\sigma\sigma} - \epsilon_{in}) = 0$ which in the long wavelength limit $\lambda \gg a$ is given for $\cos k_0 h_g$ that is nothing but $\lambda = \frac{4h_g}{2n+1}$ where n is an integer.

*In-phase radiation, $\lambda \approx \Lambda$:

This is the well known resonance attributed to the excitation of surface modes of wavelength close to the period. At that particular wavelength, all sound emitted from the groove σ over groove σ' reaches the central slit in phase. In section 2.6 we have examined the support of surface states by indentation on metallic plates in great detail.

Fig. 2.19 clearly highlights the optimum value in the nearest vicinity of the period ($\lambda \approx \Lambda$), but in a later example we will demonstrate the interplay of all the three resonant components. Fig. 2.20 illustrates the transmittance spectra through a plate of thickness $h = 0.37\Lambda$, groove depth $h_g = h_{in} = h_{out} = 0.17\Lambda$ and slit width $a = 0.08\Lambda$ that is derived from Fig. 2.19. If the incident side of the plate, symmetrically around the central slit, is corrugated by a finite number of grooves, a strong enhancement can be seen in $T(\lambda)$ in the lower left panel of Fig. 2.20. We have chosen to compare the transmittance through one slit in a non-corrugated plate (black curve), with plates having three different numbers of patterning, $N_\alpha^{input} = 5, 10$ and 20

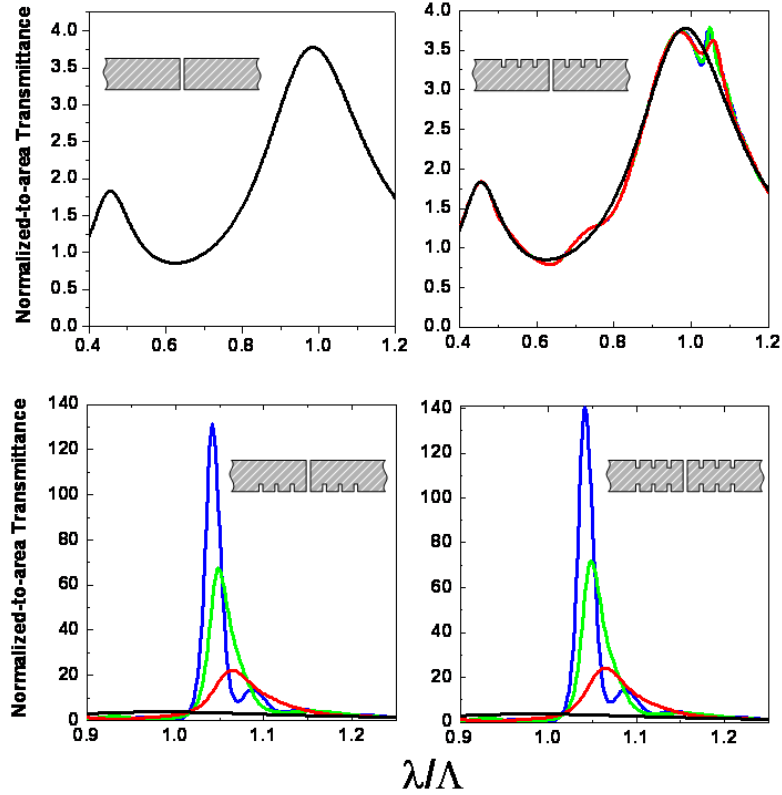


Figure 2.20: Influence on the transmittance spectra dependent on the location and numbers of surface corrugations with the geometries as specified in the caption of Fig. 2.19. The curves of colour black, red, green and blue, corresponds to (0, 5, 10, 20)-numbers of indentations respectively.

(red, green and blue respectively). Before discussing further what can be observed in that figure, little contribution to the total transmittance $T(\lambda)$, when corrugating the wave emerging side only is given for $N_{\alpha}^{output} = 5, 10$ and 20 , seen in the upper right panel. The two peaks that almost are unaffected by patterning the output side are located about $\lambda_1 \approx 0,5\Lambda$ and $\lambda_2 \approx 1,0\Lambda$. These peaks are associated to the excitation of slit-cavity modes of the FP type, which occurs at $\lambda_{FP} \approx \frac{2h}{m}$ for $m = 1, 2$. N_{α}^{input} varying between 5, 10 and 20 gives rise to increasing $T(\lambda)$ when the number of grooves is raised. At a wavelength equal the period Λ one finds a transmittance

minimum for all cases which is the Woods anomaly. This minimum is accompanied with a strong peak arising slightly above the period ($\lambda \approx \Lambda$) which is connected to the excitations of ASWs due to the periodicity of the structure. Fig. 2.21 shows the

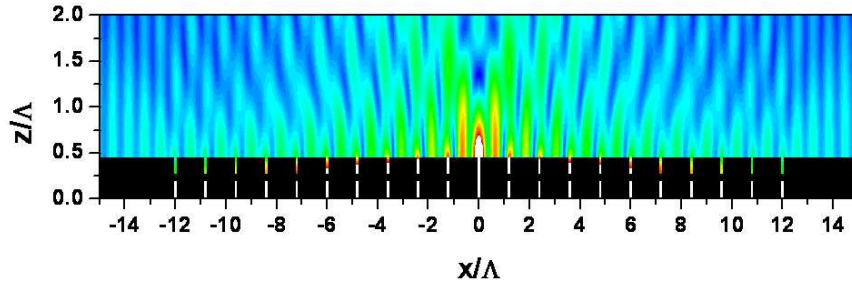


Figure 2.21: Near-field pressure on a plate with a single slit surrounded by corrugations. The geometries are the same given in the caption of Fig. 2.19 and the field is calculated for $\lambda = 1.05\Lambda$.

fingerprints of those surface mode as time averaged pressure in the near-field, in the presence of both input and output indentations. For the case with $N_\alpha^{input} = 20$, $T(\lambda)$ is enhanced by a factor of 130, and with regards to $N_\alpha^{input} = N_\alpha^{output} = 20$ in the lower right panel of Fig. 2.20, this factor even reaches a value of 140. It though has to be announced, that the role of the output corrugations in combinations with grooves at the input side as well, does not change the transmittance spectrum significantly. However, apart from the fact that $T(\lambda)$ generally is unchanged by virtue of additionally structuring the output side, the property to influence the angular distribution of sound and creating a collimated beam is highlighted in the following. The upper panel in Fig. 2.22 illustrates a transmittance spectra containing all resonant features mentioned before. Here two wide-banded FP modes located approximately around $\lambda = 2h \approx 1.7\Lambda$ and $\lambda = h \approx 0.8\Lambda$ which surround the narrow sharp transmittance peak close to the period are seen. Interestingly we also see the correspondence to groove cavity modes $\lambda \approx 4h_g$ which for this particular example is located at $\lambda \approx 0.8\Lambda$, at the second FP peak. With respect to the output corrugations, it will now become clear, how they are affecting the formation of the beam, when the acoustic wave is

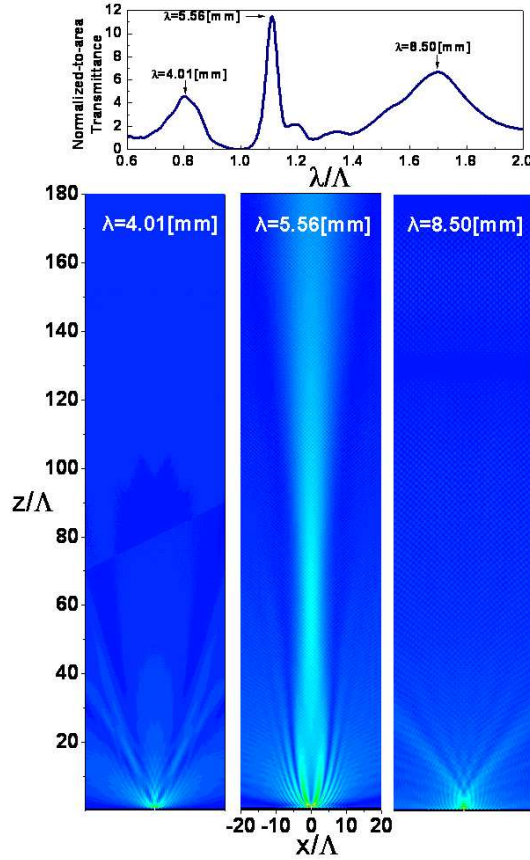


Figure 2.22: Transmittance diagram for a plate of thickness $h = 0.7\Lambda$, groove depths $h_g = 0.2\Lambda$ and slit width $a = 0.08\Lambda$. In this particular case the period Λ of the system is 5 mm, giving rise to three resonances ($\lambda_1 = 4.01$, $\lambda_2 = 5.56$ and $\lambda_3 = 8.50$ mm) to which we have calculated a pressure far-field map.

emerging the output side of the structure. For these three resonant peaks we have, as illustrated in Fig. 2.22, performed a pressurefield mapping in the far-field. All field plots clearly illustrate the presence of an enhanced acoustical transmission by virtue of a strong (absolute) pressurefield confinement, at the slit, towards the output side of the structure. At $\lambda \approx 5.5$ mm though, an ASW is also excited at the output side of the structure, this then is scattered away by the grooves, and interferes constructively with the wave at the slit, giving rise to elongated focal spot in the far-field, as has been illustrated in the lower central panel of Fig. 2.22. In order to create this type of directional far-field beaming in an off-axis fashion, a simple aperiodicity is

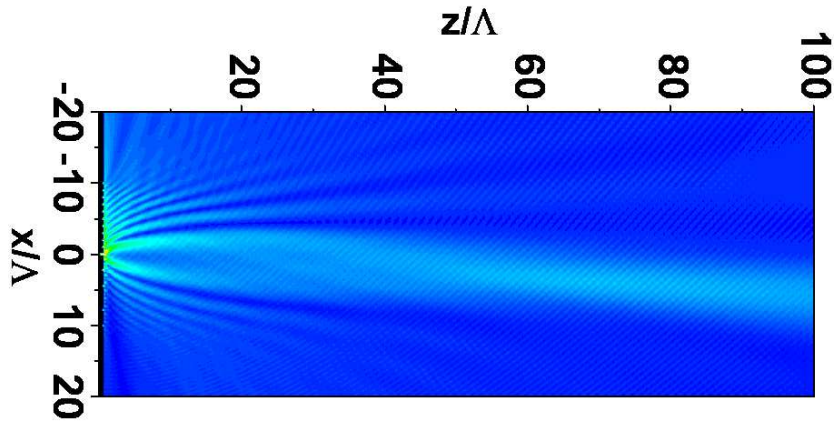


Figure 2.23: Off-axis pressure field mapping of sound through a structure with same geometry as in Fig. 2.22, though with unequal groove distances: $\Lambda(\sigma > 0) = 1.11\Lambda(\sigma < 0)$.

introduced in the groove spacing. Considering a corrugated plate, with the geometries as depicted in Fig. 2.22. The discrete groove locations, as specified formerly, are $\sigma > 0$ for grooves located to the RHS of the central slit ($\sigma = 0$) and $\sigma < 0$ representing the LHS, all placed at the structures input and output side, simultaneously. The main difference in the geometries compared to the one in Fig. 2.22, are the periods: $\Lambda(\sigma < 0) = \Lambda(\sigma = 0)$ and $\Lambda(\sigma > 0) = 1.11\Lambda(\sigma < 0)$. For this new structure comprising two different periodicities, as expected, one obtains two Wood anomalies where these minimas are followed up with two transmission peaks, deducing the excitation of ASWs of wavelengths λ close to these periods. As a consequence of this anisotropic surface pattering, the collimated beam is inclined to the side of larger period $\Lambda(\sigma > 0) = 1.11\Lambda(\sigma < 0)$, as one may observe in Fig. 2.23, for $\lambda = 5.77$ mm.

For a single slit within a perfect rigid plate, we have demonstrated how acoustic waves efficiently can be transferred through this aperture. It has been shown that the main mechanism giving rise to an enhanced transmission, is governed by to right choice of geometrical parameters which allows the coupling to FP resonances. In

particular by flanking the transmission with surface corrugations and allowing the coupling with ASWs, we have shown that by means of pressure field mappings one can associate far-field sound beaming with this resonant attribute. Moreover, it is also possible to control the spatial location of an elongated focal spot in an off-axis orientation, by texturing the surface corrugations with different periods at the LHS and the RHS of the central slit.

2.9 Direct comparison to the optical counterpart

A complete landscape of the acoustic transmission properties of subwavelength apertures has been presented throughout this chapter. We have studied the emergence of FP resonances in single apertures and when these apertures are placed in a periodic fashion, a new type of transmission resonance appears in the spectrum. It has been demonstrated that this resonance stems from the excitation of an acoustic guided wave that runs along the plate, which strongly hybridizes with the FP resonances associated with waveguide modes in single apertures. Hopefully the readers mind has not got confused when swapping between the terms of acoustic guided modes and the excitation of ASWs. In the field of optics it is clear and unambiguous. Despite of controverse explanations, denials and false interpretations regarding the identification of the origin of EOT in its first years [103], it is clear that surface plasmons play a key role in transferring light efficiently from the input side of a metal film (consisting of slits or holes) to the output region [104]. To the best of our knowledge, the idea of corrugating an interface to create a fluid-borne ASW was first proposed [95] and verified experimentally [96] by Kelders and co-workers in connection with ultrasonic surface waves in porous media. In this study regarding groove gratings, the kind of waves supported by this structure were identified as ASWs even though they rather are reminiscent to the spoof nature of these waves as of impenetrable structures, which is widely used in optics (spoof SPPs [28]). The

	Slit With fundamental slit waveguide mode	Hole With fundamental hole waveguide mode	$T_{res}(slit)$	$T_{res}(hole)$
EOT P-polarized	$q_z = \sqrt{\varepsilon_h} k_0$ Propagative	$q_z = \sqrt{\varepsilon_h k_0^2 - \pi^2/a^2}$ Cutoff	$\frac{\lambda}{\pi a_x}$	$\frac{3}{4\pi} \frac{\lambda^2}{a_x a_y}$
EAT	$q_z = n k_0$ Propagative	$q_z = n k_0$ Propagative	$\frac{\lambda}{\pi a_x}$	$\frac{\lambda^2}{2\pi a_x a_y}$

Figure 2.24: Tabular representation of the similarities between EOT and EAT

existence of geometry-induced EM spoof surface modes in 2D hole arrays perforated on PEC films, is the origin of the EOT phenomenon in metals at the THz or microwave regimes. These EM modes have similarities with guided modes which we have discussed for acoustic waves. However, there is a fundamental difference: in the acoustic case, these modes are not truly surface modes as the two surfaces of the plate, always are connected via a propagating wave. Nevertheless, those acoustic guided modes, hybridized with the FP resonances associated with the hole or slit cavities, are the true mechanism for boosting sound transmission through tiny apertures. A summarizing table is illustrated in Fig. 2.24 highlighting the intrinsic equivalences and differences between EOT and EAT.

2.10 Summary and future work

This chapter of the thesis dealt with a theoretical transmission study on sound passing through subwavelength apertures, both in the finite and infinite case. With a ME technique, in the long wavelength limit we have been able to gather analytical insight into all structures in both 1D and 2D, and henceforth provided exact results on the fundamental ingredients, playing a key role of transferring sound efficiently through a perfect rigid hole array. Since the emergence of this topic, a vast amount of

theoretical and experimental work has been employed to gain further insight into the system, where modifications and other physical events have been the theme of study. Extraordinary transmission of sound has been experimentally observed for a periodic array of slits and circular holes in rigid plates made out of both steel and brass [90, 94]. Other variations such as the acoustic bull's eye structure or the compound array of hole structures have been analyzed to present 3D collimation and FP peak splitting respectively [105, 106]. In all cases the apertures analysed have been only a few mm wide and resulted in excellent agreement between theory and experiment, for lossless assumptions. This means that despite of small holes, drag forces inside the apertures due to fluid viscosity which significantly would lower the transmittance efficiency, do not play a crucial role. However, Estrada et al. have examined EAT for sound-soft plates (Al) immersed in water, giving rise to elastic wave coupling to the structure and providing rich phenomenological properties, different to the optical counterpart [97, 98].

All together it could be interesting to funnel acoustic waves through even smaller apertures in the μm range, and by this studying the importance of viscous losses in the MHz regime. Filling the holes with an fluid inclusion different from the background or imposing an fluid flow to the system, would be new foundations in order to tune the bands and locations for enhanced sound transmission. Finally it could be very important for metamaterial studies to introduce an effective medium theory, in order to understand the fluid nature of a vibrating perforated screen together with the retrieval of an effective mass density.

Chapter 3

Confining acoustic surface waves along a wire

The propagation of sound waves through a hollow tube remains a classical example of a very first demonstration regarding acoustic waveguides and their mathematical solutions, which basically can be found in any textbook [75]. Technically there is no question that the tube, for guiding and absorbing sound is found in many areas such as the automotive field, ultrasonic NDT, music instruments, probing for detecting vibrations and medical surgery and treatment. Certainly we will keep all technicalities far away from our view, but one has to bear the implications in mind on how to control sound by a tube or rod. Thus briefly, we are going through some basic schemes that enable efficient sound guiding, which will be presented in the following. In this present chapter, again we have to distinguish between elastic (structure-borne sound) and acoustic (fluid-borne sound) waves. As of the complexity of elastic waves (the wave is decomposed into a longitudinal and transversal displacement), a broad variety of different guiding techniques exists. Elastic waves in a isotropic elastic rod can ideally propagate either purely as a longitudinal, dilatationally displaced wave or in a shearing manner. Typical modes existing in both homogeneous plates or rods are the flexural or "bending" waves, where the bending is manifested in a 4th order

spatial derivative. Also the so-called torsional modes or "screwing waves" that are displacing in the angular direction and propagating along the axis, are a well known member in the broad family of elastic waves in a tube or rod. The concept of "slow waves" which we will present later for a corrugated wire, is already a main theme regarding both torsional waves and flexural modes. Usually they are supported by the presence of a cladding layer or a hole within the rod forming a hollow tube. Cladded or layered rods are the circular versions of the layered guides supporting the propagation of Love-waves, whereas the hollow rod, analogous to the non-circular version constituting an air gap between two finite elastic slabs, is giving rise to gap surface modes of the Stoneley-Scholte type. For more informations regarding all those type of waves, the tutorial review by R. N. Thurston is an excellent starting point [107].

Acoustic waves through tubes need no introduction in terms of guiding sound. It is not clear when they were initially studied but in the "theory on sound" by Lord Rayleigh this theme was taken seriously under investigation, maybe for the first time [108, 109]. In this chapter we present a new type of waveguide not only able to guide sound within the subwavelength frequency regime, but also to slow down the group velocity to a still standing wave. Within the concept of phononic crystals it is not a new idea to reduce the speed of sound, but as those type of crystals are Bragg-scattering based, the phenomena obtained by those structures would truly be limited in their capabilities for sub-diffraction limited sizing [2].

3.1 Theoretical description of a corrugated metawire

In this section we present a theoretical formalism devoted to analyze the propagation of acoustic surface waves (ASW) along cylindrical wires. A perfectly rigid cylindrical wire does not support the propagation of ASWs. However, as we have discussed in section 2.6 from Chapter 2, it is known that when a flat interface between two

fluids is periodically corrugated, ASWs are supported [95, 96], which is also the case for an equivalent solid-solid interface with shear-horizontal waves, see [110]. Our aim is to study these geometrically-induced ASW in a cylindrical geometry. Sound wave propagation along corrugated wires have been studied before [111–116]. However, our motivation is to demonstrate the capabilities of these ASWs for acoustic wave focusing and slowing. Consider an acoustical perfect rigid ($\partial_n p = 0$) cylinder of radius R_o into which periodically rings are grooved, just as the schematics in Fig. 3.1 is illustrating. The rings, that are separated with constant Λ , have the

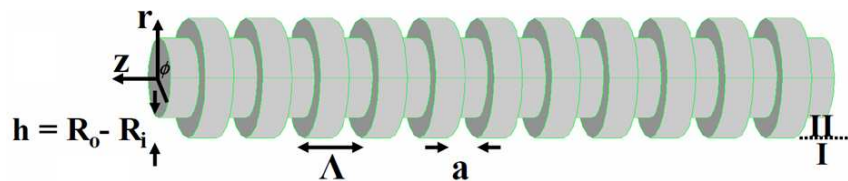


Figure 3.1: Schematic view of the acoustic metawire analyzed. The rings of width a and depth $h = R_o - R_i$ are arranged into a 1D lattice of constant Λ . The outer and the inner radius are denoted as R_o and R_i respectively.

depth $h = R_o - R_i$ and width a . Since the structure is considered to be perfectly rigid, Λ is chosen to be the unit length of the structure. Initially, we are interested in calculating the dispersion relation ($k_z(\omega)$) of the geometrically-induced ASWs propagating along the corrugated wire. To simplify the problem, we will assume that the pressure field does not have azimuthal (ϕ) dependence. How can this corrugated structure support the propagation of surface states? Obviously we know that this type of geometry is inducing ASWs for a planar structure, and in the following it will be demonstrated, that one basically can fold a planar structure into a cylinder, and obtain a likewise picture. With the knowledge acquired from the previous chapter, we can decompose all wave interactions into their subregions, which for this current case, divides the structure, as given in Fig. 3.1, into a cylindrical halfspace of wave irradiation that is region I , and a domain of periodic cavities located in region II . As a possible solution for the Helmholtz equation in region I , a Sommerfeld type wave

is sought [10], composed of a discrete set of Bloch waves:

$$p_I(r, z) = \sum_{n=-\infty}^{\infty} C_n K_0(q_n r) \sigma_n(z) \quad (3.1)$$

here $\sigma_n(z) = e^{ik_{z,n}z}/\sqrt{\Lambda}$ and the expansion coefficients are C_n . The radial dependence is governed by the zero-order modified Neumann function K_0 . The wavevector component in the r -direction is $q_n = \sqrt{k_{z,n}^2 - k_0^2}$ with $k_{z,n} = k_z + n\frac{2\pi}{\Lambda}$ and $k_0 = \frac{2\pi}{\lambda}$ where the integer n represents the diffraction orders. Our main interest is devoted to regimes where $k_z > k_0$, in which the pressure p_I decays exponentially with r as $r \rightarrow \infty$. In this case, the geometrically-induced ASW are truly bound. As no pressure field can penetrate into the sound-hard wire (steel or brass), the only non-zero field distribution in region II wire occurs within the radial grooves:

$$p_{II}(r, z) = \sum_{m=0}^{\infty} A_m [J_0(\beta_m r) - \alpha(m) N_0(\beta_m r)] \psi_m(z) \quad (3.2)$$

where $\alpha(m) = J_1(\beta_m R_i)/N_1(\beta_m R_i)$ and $\beta_m = \sqrt{k_0^2 - (m\pi/a)^2}$ which represents the wavevector inside the ring. The pressure field inside the grooves is expanded in terms of the ring waveguide modes m , in which the z -dependence is controlled by the function

$$\psi_m(z) = \sqrt{\frac{2 - \delta_{0m}}{a}} \cos \frac{m\pi}{a} \left(z + \frac{a}{2} \right), \quad (3.3)$$

equivalent to $\langle x|m \rangle$ from Eq. (2.8) in the previous chapter, and the radial dependence is dictated by the zero-order/first-order Bessel and Neumann functions J_0, J_1, N_0 and N_1 , respectively. If we take the radial component in the gradient of the pressure from Eq. (3.2), we obtain the particle velocity v_r that must vanish at every face of the milled wire as of a PRB approximation. The function $\alpha(m)$ is satisfying this condition at the very bottom of the corrugated rings. The matching procedure of the acoustic field at the single interface ($r = R_o$) is performed similarly to Eq. (2.40) from section 2.6 governing a groove grating. Continuity of the acoustic field at that interface is imposed where the pressure is continuous only at the ring opening, whereas the radial component of the velocity v_r must be continuous along that

entire interface. As we seek surface eigenstates, we can employ the same matching procedure as we did with Eq. (2.40), there we just need to cancel the wave irradiation term and account for cylindrical structures. In other words, the pressure continuity is projected over ring waveguide modes while the radial velocity component is projected over periodic Bloch states, which is giving rise to:

$$\begin{aligned} \sum_{n=-\infty}^{\infty} C_n K_0(q_n R) S_{nm'} &= A'_m [J_0(\beta_{m'} R) - \alpha(m') N_0(\beta_{m'} R)] \delta_{mm'} \\ C_n q_n K_1(q_n R) &= \sum_m A_m \beta_m [J_1(\beta_m R) - \alpha(m) N_1(\beta_m R)] S_{nm}^*, \end{aligned} \quad (3.4)$$

the mode matched pressure and velocity respectively. Here it becomes clear, when the spatial derivative in Eqs. (3.1,3.2) is taken with respect to the radius in order to obtain v_r in regions I/II , a reordering of the Bessel and Neumann function in Eqs. (3.4) is the cause. The overlap function S_{nm} is given as:

$$S_{0n} = \sqrt{\frac{a}{\Lambda}} \operatorname{sinc} \frac{k_{z,n} a}{2}. \quad (3.5)$$

As we did in the previous chapter, also here it is convenient to define a ring modal velocity of the following kind:

$$v_m = A_m \left(J_1(\beta_m R) - \alpha(m) N_1(\beta_m R) \right), \quad (3.6)$$

and with no loss of generality, with this definition comprising the m^{th} ring mode for the radial velocity field, we again can gather an entire linear set of acoustic continuity equations, and express them as a homogeneous system:

$$\boxed{(G_{mm} - \epsilon_m) v_m + \sum_{m' \neq m} G_{mm'} v_{m'} = 0}. \quad (3.7)$$

With Eq. (3.7) we can generalize the mode matching technique and confirm its suitability even for this current cylindrical case. The description of ϵ_m accounting for the bidirectional wave motion in an aperture applies also to the radial bouncing process of sound within the ring:

$$\epsilon_m = \frac{1}{\beta_m} \frac{J_0(\beta_m R) - \alpha(m) N_0(\beta_m R)}{J_1(\beta_m R) - \alpha(m) N_1(\beta_m R)}, \quad (3.8)$$

which is governed by the m^{th} mode. $G_{mm'}$ given below with Eq. (3.9), takes into account the sonic radiation emitted by waveguide mode m into free-space Bloch waves and collected by mode m' , with overlapping integral $S_{nm} = \langle q_n | \beta_m \rangle$, which provides the acoustical coupling between the n^{th} Bloch wave and the m^{th} waveguide mode:

$$G_{mm'} = \sum_{n=-\infty}^{\infty} \frac{1}{q_n} \frac{K_0(q_n R)}{K_1(q_n R)} S_{nm'} S_{nm}^*. \quad (3.9)$$

To this end, a set of linear equations for the expansion coefficients, A_m , has been built up, where the dispersion relation for the ASWs can be extracted by just looking at the zeroes of the determinant of the corresponding matrix. Before we get into the details, we are starting out with a mandatory convergence study and thus apply appropriate geometries for a metawire with $a = 0.5\Lambda$, $R_o = 1.5\Lambda$ and $h = 0.5\Lambda$. Fig. 3.2 illustrates a good convergence with the fundamental ring waveguide mode

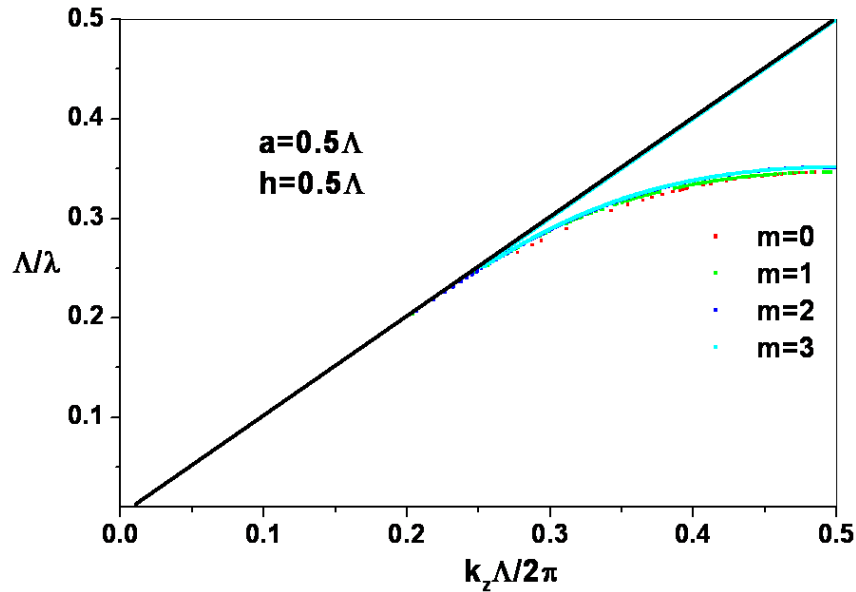


Figure 3.2: Convergence study with a dispersion relation plot for a metawire. The ring width $a = 0.5\Lambda$ whereas the ring depth $h = 0.5\Lambda$. For a fixed high number of diffraction order convergence is sought for waveguide modes upto $m = 3$.

and already now gives us a clue on the ASWs that can be excited on a corrugated

sound-hard wire. For very narrow subwavelength ($\lambda \gg a$) rings that are milled into a steel or brass wire, the fundamental mode approximation ($m = 0$) holds very precise and hereby makes room for further reduction in Eq. (3.7), which yields an azimuthally independent dispersion relation for ASWs sustained by the metawire:

$$\boxed{\sum_{n=-\infty}^{\infty} \frac{\beta_0 K_0(q_n R_o)}{q_n K_1(q_n R_o)} |S_{0n}|^2 = \frac{J_0(\beta_0 R_o) N_1(\beta_0 R_i) - J_1(\beta_0 R_i) N_0(\beta_0 R_o)}{J_1(\beta_0 R_o) N_1(\beta_0 R_i) - J_1(\beta_0 R_i) N_1(\beta_0 R_o)}}. \quad (3.10)$$

At low frequencies ($\lambda > \Lambda \gg a$) which is the long wavelength limit specified for groove grating with Eq. (2.41) in section 2.6, we can approach that planar structure for wires much thicker and rings much shallower than the array period ($R_o, R_i \gg \Lambda$). Under this condition we can obtain an analytical expression for the induced ASW dispersion relation by introducing the asymptotic expansions of the different Bessel and Neumann functions involved in Eq. (3.10), that are: $J_0(x) = N_1(x) \approx \sqrt{\frac{2}{\pi x}} \cos(x - \frac{\pi}{4})$ and $J_1(x) = N_0(x) \approx \sqrt{\frac{2}{\pi x}} \sin(x - \frac{\pi}{4})$. This dispersion relation is simply the one we know from groove gratings Eq. (2.44) and directly applicable to the metawire

$$\boxed{k_x = k_0 \sqrt{1 + \frac{a^2}{\Lambda^2} \tan^2 k_0 h}}, \quad (3.11)$$

which immediately suggests the identification of axially excited FP modes. As in the planar case, the key parameter governing the surface mode confinement is the depth of the rings h , as we will see clearly with an example in the next section. Interestingly, those ASWs resemble the limiting values for SPPs in a flat metal surface approaching $\omega_s = \omega_p/\sqrt{2}$ where ω_p is the plasma frequency of the metal. The limiting value in Eq. (3.11) is approached for infinite parallel momentum which is given when $\tan \rightarrow \infty$, that yields an ASW frequency for a metawire $\omega_{ASW} = \pi c/2h$, again controlled by the ring depth.

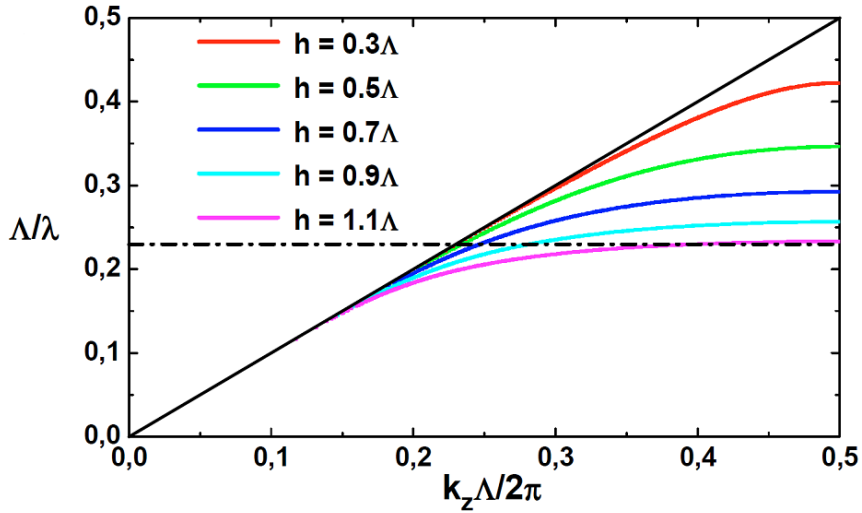


Figure 3.3: Dispersion relation for infinite structures with $a = 0.5\Lambda$, $R_o = 1.5\Lambda$ and several values of h as indicated. The bands are obtained from the analytical dispersion relation from Eq. (3.10). The intersections of the dash-dotted line with the ASW bands, will be used to illustrate the degree of field confinement as a function of the ring depths, shown in Fig. 3.4.

3.2 Geometrically tunable surface states

Fig. 3.3 displays $k_z(\omega)$ for acoustic metawires with fixed $a = 0.5\Lambda$ and $R_o = 1.5\Lambda$, but for different values of h . For very shallow grooves ($h = 0.3\Lambda$), a corrugated wire has weak sound guiding properties as $k_z(\omega)$ runs very close to the sound line ($k_z = \omega/c_0$). However, as the ring depth h becomes more and more pronounced, the tailored ASWs waves are getting more localized as the increase in the propagation constant ($k_z \gg k_0$) gives rise to a large value for $q_n \approx \sqrt{k_z^2 - k_0^2}$. Note that this increasing confinement is accompanied by a strong reduction in the group velocity $c = \frac{\partial\omega}{\partial k_z}$ towards a *flat dispersion relation* $k_z(\omega)$. As we have hinted on in the previous section, the ASW guided along the wire has a hybrid nature of partially being supported due to excited ring cavity modes, and the periodicity induced surface states. From Eq. (3.11) it is clear, that a bare ($h = 0$) sound-hard wire only provides

pure sound radiation and no bound modes are supported, $k_z = k_0$ and $\omega_{ASW} \rightarrow \infty$. Contrary to this, the analytical expression in Eq. (3.11) enables us to explore the deviation of the ASW bands in relation to the sound line when the groove depth h is increased, which is lowering the the asymptotic behaviour of the curves as seen in Fig. 3.3 and also is predicted by $\omega_{ASW}(h)$. The increase in confinement is

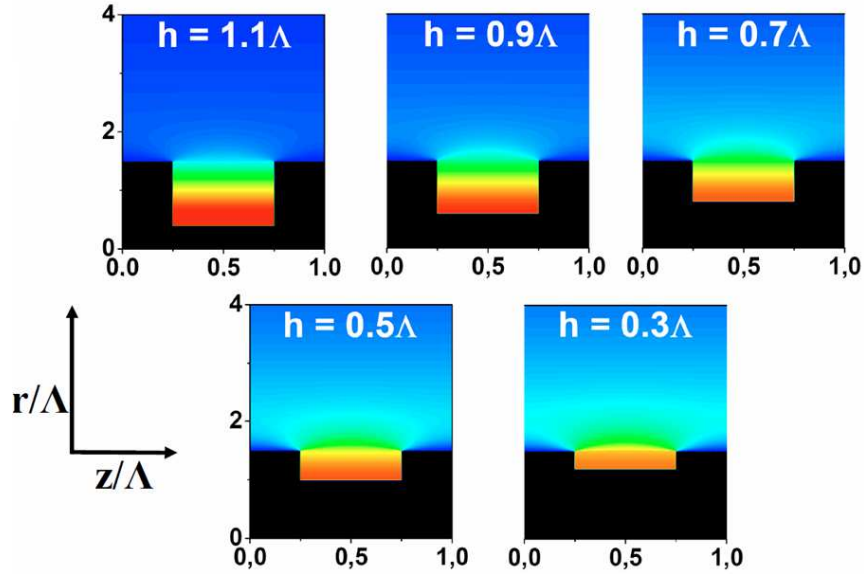


Figure 3.4: Pressure field ($|p|$) within one unit cell (rz -plane) for metawires of various depths h at fixed frequency ($\Lambda/\lambda = 0.23$), which corresponds to the intersections of the dash-dotted line with the ASW bands presented in Fig. 3.3.

visualized by virtue of the pressure field plots shown in Fig. 3.4, which show the pressure field amplitudes (evaluated at $\Lambda/\lambda = 0.23$, corresponding to the dot-dashed horizontal line in Fig. 3.3) for different ring depths. Unambiguously, when we follow the intersection of the bands with dot-dashed line, we are moving towards decreasing group velocity and increasing ring depths. In other words, as we clearly can see in Fig. 3.4, the larger h is, the higher the pressure field concentration in the bottom of the rings becomes, which collectively as of an infinite length is giving rise to an enhanced sound guiding profile.

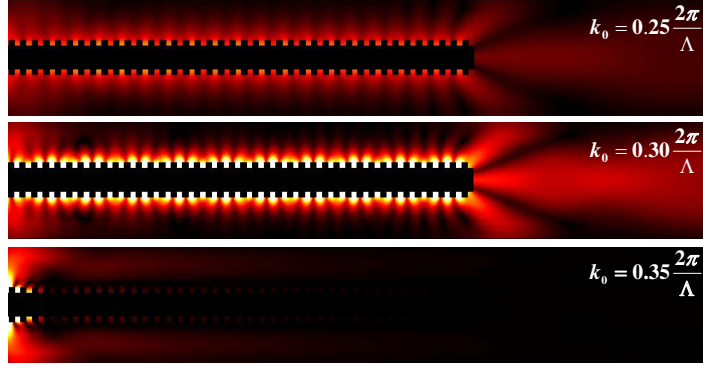


Figure 3.5: Numerical (FE) pressure field-mapping $|p|$ of a truncated metawire (40Λ) for three different wavenumbers k_0 . Geometries are as in Fig. 3.3 with ring depth $h = 0.5\Lambda$.

In order to illustrate the confining properties that are connected to the excitation of ASWs, finite element (FE) (COMSOL Multiphysics) simulations have been employed for a metawire of finite length, $L = 40\Lambda$, with the parameters corresponding to Fig. 3.3 for $h = 0.5\Lambda$. Depending on the wavelength of the impinging acoustic wave, sound can be guided along the corrugated wire or being radiated away (similar to phononic crystals [2]). This is exposed in Fig. 3.5 for three different wavelengths. For $k_0 = 0.25\frac{2\pi}{\Lambda}$, which is in the nearest vicinity of the sound line, only poor field confinement to the wire is expected, but as one tends to higher frequencies ($k_0 = 0.30\frac{2\pi}{\Lambda}$) a strong acoustic wave localization can be observed. Note that when the ASW reaches the end of the metawire, this surface wave is scattered and yields a strong sound radiation at the wire tip. For the last case with $k_0 = 0.35\frac{2\pi}{\Lambda}$, the gap of the ASW band is reached and the incident pressure field is being radiated away at the entrance of the wire, as no ASWs are supported at that wavelength. To this end, we can readily confirm that the analytical prediction for the dispersion relations, given in Eq. (3.10) based on the fundamental ring waveguide mode $m = 0$, is a precise mean for understanding sound propagation along a corrugated wire, which

is in good agreement to results obtained with FE techniques.

3.3 Applying the slowing effect for superfocusing sound

Apart from the possibility of subwavelength field confinement of sound by taking advantage of the strong localization associated with the ASWs, in this section we propose two schemes for focusing sound at the end of a corrugated wire and/or stopping sound of different frequencies at different places along the rod. The basic structure able to support these two phenomena is a corrugated wire in which the depth of the grooves, adiabatically (i.e., back-reflection and scattering are negligible) along the wire is increased (see top panel of Fig. 3.6). If the gradual increase of h

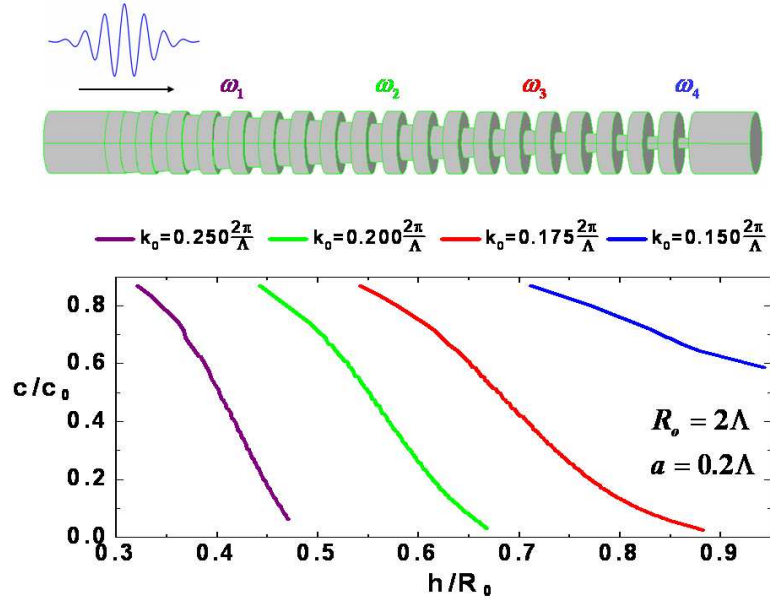


Figure 3.6: Schematic of a metawire with adiabatic reduction of R_i and incident wave packet. Lower panel shows the normalized c versus h calculated with the mode matching technique for $k_0 = 0.15 \frac{2\pi}{\Lambda}$, $0.175 \frac{2\pi}{\Lambda}$, $0.2 \frac{2\pi}{\Lambda}$ and $0.25 \frac{2\pi}{\Lambda}$ with $a/\Lambda = 0.2$ and $R_0 = 2\Lambda$.

is chosen such that the depth of the grooves at the final end leads to an asymptote frequency ω_4 , then an incident acoustic wave of that particular frequency will be focused at the tip of the corrugated wire. Moreover, if now the incident acoustic wave is not monochromatic but contains several frequencies above ω_4 , each of these frequencies will be stopped at different places along the wire. This is due to the univocal relation between h and the frequency of the ASW band edge, as demonstrated in Fig. 3.3. The slow sound phenomenon is illustrated in the lower panel of Fig. 3.6, in which the evolution of the group velocity, c , as a function of h for four different frequencies is displayed. For calculating these four curves we have considered infinitely periodic corrugated wires with uniform h . It is then envisaged that, in a finite wire presenting a gradual and adiabatic increase of h , the wave component associated with each frequency will be stopped at the spatial location (h) in which $c \rightarrow 0$ for that particular frequency. The same concept can be extended to conical

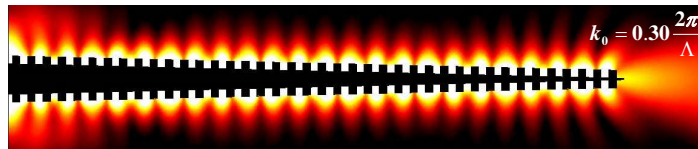


Figure 3.7: Numerical (FE) pressure field-mapping $|p|$ of a corrugated cone with 40 periods at a wavenumber $k_0 = 0.30 \frac{2\pi}{\Lambda}$. Geometries are as in Fig. 3.3 with ring depth $h = 0.5\Lambda$, though with a decreased outer radius of factor 10 when comparing the base with the tip.

sound-hard corrugated structures, where both R_o and R_i are adiabatically reduced. If we apply the same geometries as in Fig. 3.3 for $h = 0.5\Lambda$ being constant, though with a 10 fold reduction in the outer radius at the tip (compared to the base of the cone), we will experience a gradual slowing down of the acoustical energy along the cone, giving rise to a high field concentration at the tip, see Fig. 3.7. Even though

the structure is conical and provides gradual sound confinement along the axis, as a consequence of the adiabatic reduction that does not make the cone more disperse compared to a homogeneous corrugated metawire, we can relate the wave motion to the dispersion relation in Fig. 3.3. As can be seen, a frequency has been chosen that provides strong excitation of ASWs where deep subwavelength confinement to the tip ($R_i = \frac{\lambda}{30}$) takes place.

3.4 Confining light along a corrugated perfect conducting wire

In this chapter we presented a theoretical study on the acoustic wave propagation along a periodically corrugated perfect rigid wire surrounded by fluid. It was shown how ASWs can be engineered with their propagating properties controlled by geometrical means. These highly localized ASWs give rise to strong acoustical field confinement along the wire, whereas the slowing down of sound decelerate the group velocity down to zero. What is believed to be a promising feature of these low-loss propagation properties, is the ability to tune sensing and screening applications with good transducer coupling. In the optical analogy regarding the guidance of spoof SPPs along PEC wire, from [30] it is known that the dispersion relation for the geometrically-induced SPPs within the fundamental mode approximation, takes the following form:

$$\sum_{n=-\infty}^{\infty} \frac{\beta_0 K_1(q_n R_o)}{q_n K_0(q_n R_o)} |S_{0n}|^2 = \frac{J_1(\beta_0 R_o) N_0(\beta_0 R_i) - J_0(\beta_0 R_i) N_1(\beta_0 R_o)}{J_0(\beta_0 R_o) N_0(\beta_0 R_i) - J_0(\beta_0 R_i) N_0(\beta_0 R_o)}. \quad (3.12)$$

This is a very interesting result, as due to the difference in the boundary conditions (either perfectly rigid or conducting for geometry-induced ASWs or SPPs, respectively), the dispersion relations for the surface waves in the electromagnetic and acoustic cases are quite similar but not identical. Remarkably, this is not the case in 1D-structures (periodic array of 1D grooves in a flat interface) where the dispersion

relation of the surface waves is given by $k_z = k_0 \sqrt{1 + \frac{a^2}{\Lambda^2} \tan^2 k_0 h}$ within the long wavelength limit provided $R_o, R_i \gg \Lambda$ as we have seen before. One may therefore

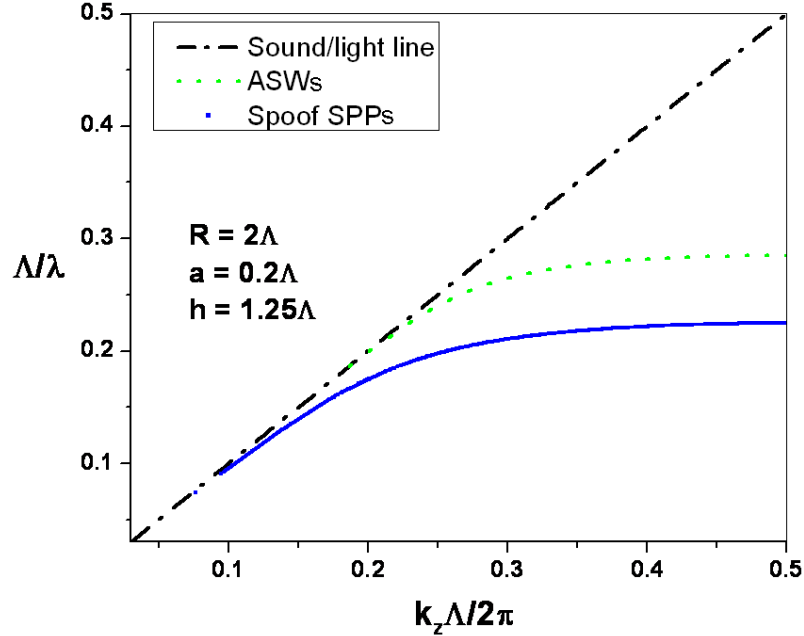


Figure 3.8: Direct comparison of spoof SPPs and ASWs along a metawire of same geometries. The unitlength of the structure, Λ , must be identical for sound and light without violating any of the assumptions taken.

be tempted to ask, even though for low frequencies at large radii, the dispersion relations for ASWs and spoof plasmons along a corrugated wire are equivalent (if the wires can be scaled to a similar size, regarding sound and light), what the difference between Eq. (3.10) and Eq. (3.12) might be. We are trying to explain that by a direct comparison of the band diagrams for light and sound structures of same geometrical parameters, as illustrated in Fig. 3.8. Here it is clear, that this mathematical curiosity implies more than only a swapping of zeroes and ones in the corresponding expressions for the dispersion relations, Eq. (3.10, 3.12). Moreover, it is evident that the spoof SPPs sustained by a corrugated wire seem to experience better field confinement compared to the acoustical counterpart due to the flatter

curve and a consequently lower group velocity. In that instant, we have checked, that the long wavelength limit is approached when we choose very subwavelength geometries and large radii, and the two different dispersion relations for sound and light coincide.

3.5 Conclusion and further directions

The prospect of engineering an acoustic surface wave along a corrugated wire opens up a possibility to confine and slow down sound. Moreover, by gradual energy concentration, super-focusing in the sub-millimeter range could be achieved and the possibility to create an axial-guide with tunable frequency passbands is facilitated. With minor technical extensions, acoustical scanning, spectroscopy, medical ultrasound instrumentation and imaging could obtain good field resolution.

An experimental realization of a metawire would not be a difficult task. Milling rings into a steel or brass rod with a diameter of a few mm, is easily accomplished in a metal workshop. The acoustic source could be realized out of a piezoceramic shell of hollow cylindrical shape [117], attached to the base of the wire. The azimuthal dependence of ASWs on a helically grooved metawire would be a very interest modification to study. Introducing helical indentations could give the possibility to create a new type of polarization of air-borne sound, which also could be accomplished by an elastic excitation of torsional waves. Generally speaking, the tunability of the geometry induced ASW by means of elastic waves (flexural or longitudinal) would form another interesting topic.

Chapter 4

A holey structured metamaterial for acoustic deep subwavelength imaging

In the quest of a perfect acoustic imaging device able to capture a subwavelength object, one must admit that only little contribution has been accomplished [2, 118] when comparing to the huge impact, Pendry's perfect lens for EM waves has aroused [53]. In the introductory part of this thesis, we have reviewed a few concepts that in the last decade have been employed in order to achieve this goal to resolve a sonic "picture" by all its near-field components. To this we certainly shall count phononic crystal structures made out of periodic elastic or acoustic scatterers. Those structures unveiled the existence of a negative refraction pass band, above the complete band gap in a 3D crystal, making the sound bend the wrong way and giving rise to a focusing phenomenon. All effects that are associated with phononic crystals are governed by Bragg scattering, limiting the size of the focus to about half of the lattice constant, unable to overcome the diffraction limit and to recover all near-field components of a scattered source [119, 120]. On the contrary, metamaterials which are structures containing exotic properties gained by geometrical arrangements of

subwavelength features rather than their chemical composition is the answer for achieving super focusing. It was since the introduction of the local resonant structures by Liu et al. [3], where rubber coated bead crystals exhibit attenuation bands due to the negative dynamical mass density of the spherical composition embedded in an epoxy background, acoustic metamaterials were born. This concept was further advanced by the theoretical prediction from Li and Chan in 2004 [60], who modelled an array of soft rubber beads embedded in a fluid in order to study the implications of Mie-scattering processes. They found that the symmetric monopolar and the asymmetric dipolar resonances of the oscillating subwavelength spheres give rise to an effective negative bulk modulus and mass density, respectively. At the degenerated band where those two modes overlap, the authors discovered a narrow band of negative refraction. Unfortunately, this work was not able to drag any experimental verifications behind, the reason is the difficult realization of a low filling fraction crystal which would distort the very effect to be demonstrated, when, e.g., the beads would be attached into a matrix array. In this chapter, we wish to demonstrate a simple perforated structure that is capable to reproduce a full 3D deep subwavelength image in the near-field side of the metamaterial. We are going through very simple analytical derivations, and demonstrate that when FP modes of order m are excited, image transfer (canalization), 50 times smaller than the wavelength and beyond is possible, which coincides very precise with experimental observations.

4.1 Theoretical development

The concept of a perfect imaging device, using a slab of an artificially engineered metamaterial, has been one of the main discoveries within the field of optics throughout the last years. It was proven that a thin slab with a negative refractive index yields a lens with unlimited resolution, solely constricted by the inherent metallic losses. The challenge thus remained to engineer a metamaterial with the desired

optical property, which probably still is the most difficult task today. In the electrostatic limit, near-field superlensing has been obtained with a thin silver slab, due to the fact that every good metallic conductor has an electric response dictated by a Drude function with a plasma frequency, below which the electric permittivity is negative [121]. Other examples of metamaterials for subwavelength imaging are layered metal-dielectric structures [122–124], metallic wire media [125–127] and holey films [128]. As already outlined in the previous pages, little compared to the huge impact on EM imaging has been accomplished for sound waves. Acoustic metamaterials broaden the range of material responses found in nature, which can be a useful guide in obtaining perfect acoustical lensing, as no natural media provides exotic properties such as negativity. Those materials provide a major step toward an effective-medium description, as the spatial periodic modulation of impedances is much smaller than the wavelength. Yet to the best of our knowledge, there has been very limited investigation in this direction.

At first, we derive the expression for a surface mode running along the interface between two half-spaces, and deduce its applicability for an acoustic superlens, analogous to Pendry’s perfect lens for sub-diffraction limited acoustic imaging [129]. The condition for the existence of an ASW propagating at the interface between semi-infinite fluids, is very similar to the equation governing the presence of a surface electromagnetic mode running at the interface between two dielectric media:

$$\boxed{\frac{k_z^I}{\rho^I} + \frac{q_z^{II}}{\rho^{II}} = 0}, \quad (4.1)$$

where k_z^I and q_z^{II} are the inverse of the decay lengths of the ASW in media I and II , respectively, and ρ^I and ρ^{II} are the corresponding mass densities. Note that the mass density plays the same role as the dielectric constant in the EM case. It is clear that if the two media have positive mass densities, there is no ASW running at the I - II interface. The necessary condition for a bound state to exist at the interface, requires that both z wavevector components have positive imaginary parts,

which implies that the mass density of the acoustic metamaterial should be negative, $\rho^{II} < 0$. One way to obtain perfect lensing is by means of negative refraction, where a metamaterial whose effective material properties - mass density and bulk modulus, are simultaneously negative and perfectly matched, impedance wise, to the surrounding medium. Fig. 4.1 illustrates the very meaning of having either the effec-

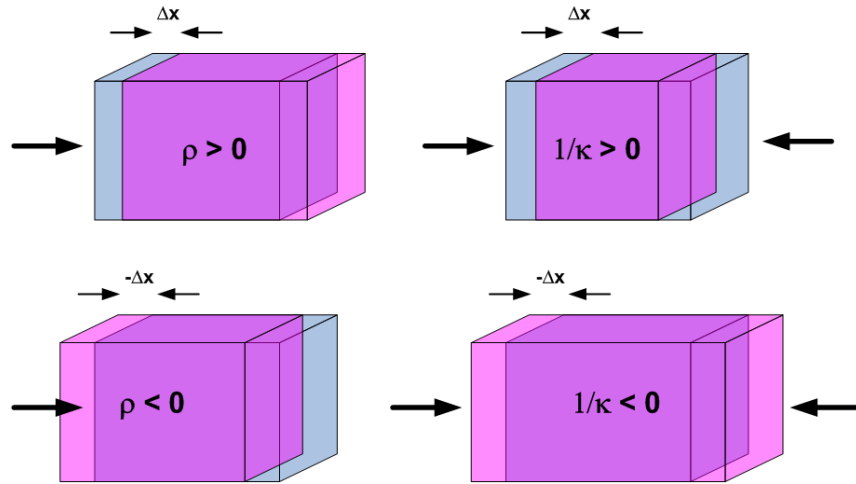


Figure 4.1: Concept of negativity in acoustics. Here the kinematics of a fluid element is demonstrated for both positive and negative effective values in the mass density and bulk modulus.

tive acoustic density or the bulk modulus negative. The blue shaded box represents a fluid element at rest, and light-red under infinitesimal displacement. Negative mass density implies that the average acceleration of a fluid segment is opposite to the driving force, whereas a negative bulk modulus in a fluid element occurs, when it is expanding when the applied dynamical pressure is acting positively on it. In the pressure static limit we neglect radiative effects decoupling velocity static contributions, which is a feasible approach when the thickness of the metamaterial is smaller than the acoustical wavelength [129]. This enables us to eliminate the dependence on the bulk modulus, where only the mass density is relevant for pressure fields. The

overall transmission across a material slab after a multiple scattering event reads:

$$T(k_{\parallel}, h) = \frac{tt'e^{iq_z^{II}h}}{1 - rr'e^{2iq_z^{II}h}}, \quad (4.2)$$

with coefficients:

$$r = \frac{\frac{k_z^I}{\rho^I} - \frac{q_z^{II}}{\rho^{II}}}{\frac{k_z^I}{\rho^I} + \frac{q_z^{II}}{\rho^{II}}}, \quad r' = -r, \quad t = 1 + r, \quad t' = 1 + r'. \quad (4.3)$$

Here it can now be worked out, that the overall transmission Eq. (4.2) will experience exponential growth for evanescent pressure fields, which is accomplished by the excitation of ASWs (Eq. (4.1) is fulfilled) on both surfaces of the lens.

As we have mentioned, acoustic metamaterials for lensing purposes are very difficult to achieve. From the literature, the only prediction on negative refraction for the focusing of sound below the diffraction limit, has so far only been presented in connection with Mie scattering of rubber spheres [60, 130]. In what follows, we are going to introduce a new three dimensional acoustic metamaterial that is easy to fabricate and is able to serve as a quasi-perfect imaging device for subwavelength objects in the near-field, much in the same way as the perfect lens proposed by Pendry [53] and endoscopes [128] do for optical imaging. Fig. 4.2 shows the basic structure, which consists of a rigid steel block (impenetrable for sound waves) of thickness h , perforated with square holes of side a forming a periodic array with lattice parameter Λ . The capability of this structure to resolve all spatial information of an acoustic image is best explained by an effective medium approach. It can be shown that, in the limit in which the transmission process is dominated by the fundamental waveguide mode inside the holes ($\lambda > \Lambda \gg a$), the transmission coefficient for an acoustic plane wave of parallel momentum $(\mathbf{k}_{\parallel}^{\beta})^2 = (\mathbf{k}_{\parallel}^{\gamma n})^2 = (k_x^n)^2 + (k_y^{\gamma})^2$ with the use of Eq. (2.16) from section 2.3 and rewritten into a 2D problem, is given as follows ($v'_0 \rightarrow v'$):

$$T_{\beta} = -v'S_{\beta 0}^*. \quad (4.4)$$

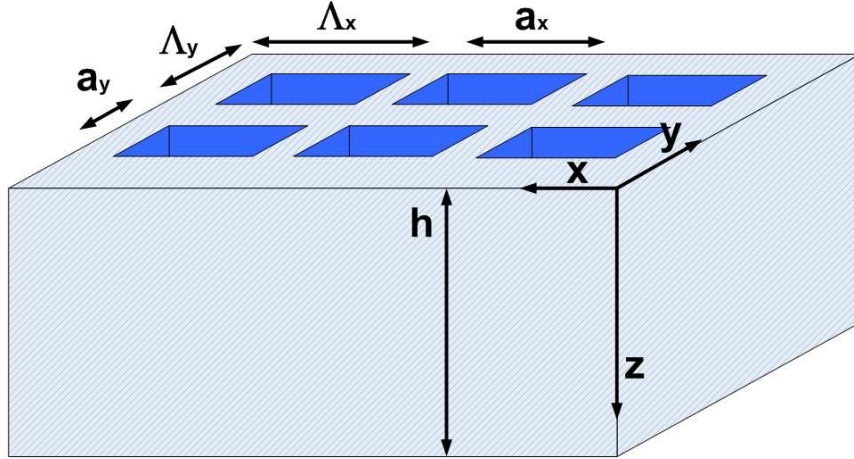


Figure 4.2: Schematics of a holey block, made out of a perfect rigid body, impenetrable for air-borne sound waves impinging on the structure.

This equation can entirely be generalized with the expressions, Eq. (A.12), contained in the system of equations:

$$T_\beta = -\frac{I^0 G^V}{(G - \epsilon)^2 - (G^V)^2} S_{\beta 0}^*. \quad (4.5)$$

Substituting the corresponding wave interaction functions, that can be found in section 2.7 now with same hole-filling fluid as in the surroundings, into Eq. (4.5), yields

$$T_\beta = \frac{4 \frac{k_0}{k_z^0} S_{00} S_{\beta 0}^*}{e^{iq_z^0 h} (G - i)^2 - e^{-iq_z^0 h} (G + i)^2}. \quad (4.6)$$

If we impose $S_{\beta 0} S_{\beta 0}^* = |S_{\beta 0}|^2$ into Eq. (4.6) it further simplifies into:

$$T_\beta = \frac{4 \frac{k_0}{k_z^0} |S_{\beta 0}|^2 e^{iq_z^0 h}}{e^{2iq_z^0 h} (i \frac{k_0}{k_z^\beta} |S_{\beta 0}|^2 - i)^2 - (i \frac{k_0}{k_z^\beta} |S_{\beta 0}|^2 + i)^2}, \quad (4.7)$$

and if we now neglect diffraction for very subwavelength geometries given as $a = a_x = a_y$ such as $\Lambda = \Lambda_x = \Lambda_y$ we can rewrite Eq. (4.7) into a zero-order transmission coefficient:

$$T_0 = \frac{4 \frac{k_0}{k_z^0} \left| \frac{a}{\Lambda} \right|^2 e^{iq_z^0 h}}{\left(\frac{k_0}{k_z^0} \left| \frac{a}{\Lambda} \right|^2 + 1 \right)^2 - e^{2iq_z^0 h} \left(\frac{k_0}{k_z^0} \left| \frac{a}{\Lambda} \right|^2 - 1 \right)^2}. \quad (4.8)$$

Eq. (4.8) resembles a very general expression for the transmission coefficient due to multiple scattering events, similar to the one expressed with Eq. (4.2). The question may now arise, whether the holey structure is able to serve as an perfect acoustic lens that amplifies an evanescent wave containing near-field components of a deep subwavelength object. For a holey block, however, q_z^0 is fixed by the fundamental waveguide mode $q_z^0 = k_0$ and will never obtain the appearance of $q_z^0 = \sqrt{k_0^2 - \mathbf{k}_{\parallel}^2}$, which is essential for the amplification process. We can thus conclude that perfect sonic lensing, with a holey structure (giving rise to $T_0 = \exp(q_z h)$ for all \mathbf{k}_{\parallel}) cannot be realized. However, if a FP resonance of order m is excited, $q_z^0 h = m\pi$, and substituted into Eq. (4.8), we have:

$$T_0 = \frac{4 \frac{k_0}{k_z^0} \frac{a^2}{\Lambda^2} (-1)^m}{\left(\frac{k_0}{k_z^0} \frac{a^2}{\Lambda^2} + 1\right)^2 - \left(\frac{k_0}{k_z^0} \frac{a^2}{\Lambda^2} - 1\right)^2}, \quad (4.9)$$

which is nothing but:

$$\boxed{T_0 = (-1)^m \text{ for all parallel wavevector components } \mathbf{k}_{\parallel}}. \quad (4.10)$$

Eq. (4.10) states that an incoming sound wave containing a broad range of spatial subwavelength informations, such that $\mathbf{k}_{\parallel} \gg k_0$, at a FP resonance $\lambda = \frac{2h}{m}$ is perfectly transmitted through a holey perfect rigid (steel, brass or ceramics) block, with all its propagating and evanescent components. For the entire derivation of Eq. (4.10) one should refer to appendix B. As a hole array acting as an acoustic waveguide contains no cutoff wavelength, this structure suggest to be a broadband metamaterial, able to capture a sub-diffraction limited object at m -frequency components. Also the term, "bulk metamaterial", is not over-hyped, because FP modes are all-angle resonances. Structures that can transfer an optical image by all its near-field components without distortion have been accomplished by means of a wire-array, or one-dimensional sandwich-structures and are widely known as endoscopes [122–127]. A similar approach than this present metamaterial has been fulfilled by means of slit arrays for light [128]. As this present holey block serves as an entirely new imaging

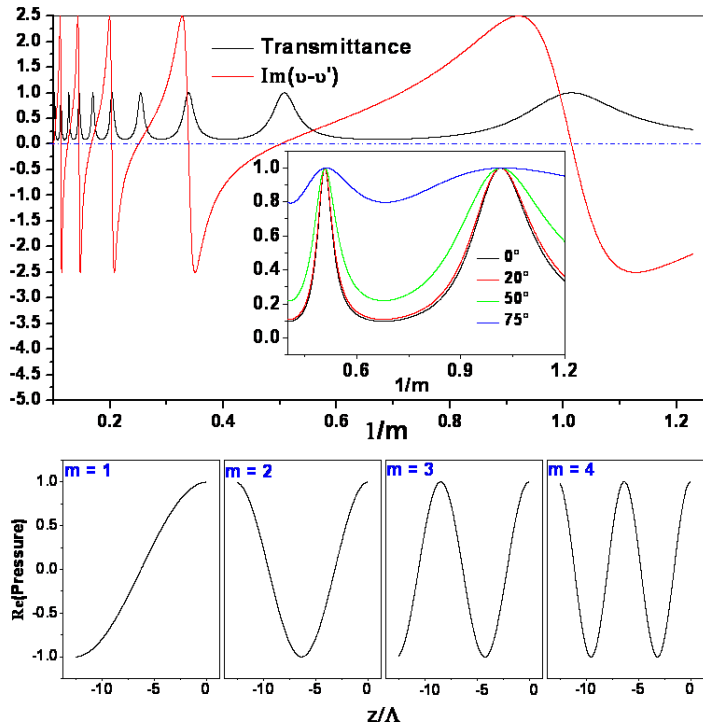


Figure 4.3: Upper panel shows the transmission spectrum together with the phase difference ($\text{Im}(v - v')$) for a hole-array metamaterial of thickness $h = 13.5\Lambda$ and square holes of size $a_x = a_y = 0.4\Lambda$. The inset depicts the angular sensitivity of the FP resonances for various angles of incidence, whereas the lower panels plot the $\text{Re}(p)$ depth profile inside the aperture of one unit cell, for the first four Fabry-Perot resonances.

device for sound waves, we remain with the term, holey metamaterial. Before we put the imaging effect to the test, by means of numerical analysis, we are briefly going to review some basic properties regarding FP resonances in a hole array structure. The upper panel of Fig. 4.3 illustrates the transmission spectrum for a hole array, with geometries given in the figure text. Already here it becomes evident, that this thick chosen structure, contains a broad range of discrete (order m) FP resonances. In the same image, we have plotted the difference of the input and output imaginary modal velocities $\text{Im}(v - v')$, to study the phase change through the holey block. It is clear, that a FP mode exhibits no phase change, at all transmission peaks, $\text{Im}(v - v')$

is exactly zero, which is reminiscent to DC (direct current) transmission lines of zero phase. From Fig. 2.11 we know that the excitation of FP resonances, implies flat bands in the dispersion relation diagram, which means that this type of resonance is supported by all parallel wave vector components \mathbf{k}_{\parallel} . We are demonstrating this for the current thick holey block, with the inset of Fig. 4.3, that unambiguously shows that the transmission peaks associated to standing wave formations within the holes, can be excited from all angles. In other words, as the thick structure supports a broad discrete range of standing wave resonances, to which we have calculated the real part of the pressure as a function of space in one unit cell for $x = y = 0$ (see lower panel in Fig. 4.3), one can hereby conclude that the holey block features bulk properties in these transparent frequency regimes.

4.2 Subwavelength imaging by means of a slit array and a hole array

For proof-of-principle purposes we introduce two different structures, starting out with an infinite array of slits. We wish to use a slab of steel or brass of thickness h , as a holey metamaterial to restore the amplitude of higher order Fourier components and to focus the image. The slab can be considered as a perfect rigid body, into which slits, of width a and periodicity Λ , are milled. One of the greatest obstacles reported on Pendry's perfect lens, are the losses. Even the smallest loss mechanism in left-handed materials, that are described by imaginary quantities in the permittivity (ε) and permeability (μ) are strongly affecting the perfect impedance matched boundaries, which are significantly decremental for imaging purposes. In what follows, we are not introducing loss mechanisms, but rely on the fact, that in acoustical hole array structures, FP resonances easily are built up for small apertures in the mm range, predicted (in inviscid fluids) and observed in several works [90, 73, 97]. A point dipole, two spikes of amplitude P_{in} , width $w = 10\Lambda$ and separation $s = 15\Lambda$

is oscillating at frequency $\lambda = 2h = 100\Lambda$, the lowest order FP mode. On either sides of the object plane, z_1 away from the structure, waves are emitted in such a way that energy in terms of propagating waves such as the near-field that exponentially decays away, leave the source. As we now know, for high resolution images,

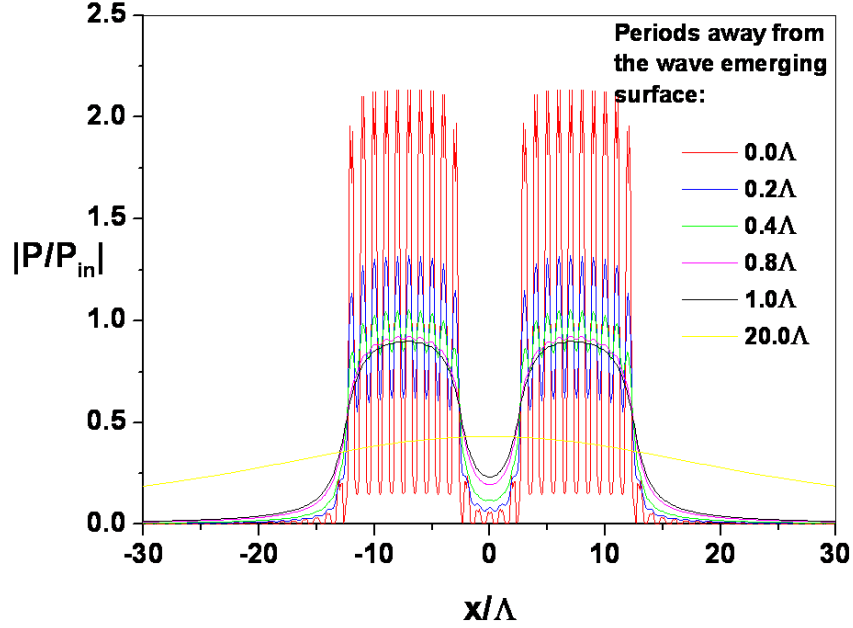


Figure 4.4: Spatial image plot ($|P/P_{in}|$) with the slit array metamaterial with the following geometries: $h = 50\Lambda$, $a = 0.5\Lambda$ at the first FP mode $\lambda = 2h = 100\Lambda$. The object are two spikes of width $w = 10\Lambda$ separated by $s = 15\Lambda$.

as of large values of $\mathbf{k}_{||}$, the field will not grow throughout the metamaterial, but as of all-angle transparency and constant phase characteristics due to the coupling to standing wave motions inside the holes, the acoustical object is rather channelled through the structure, z_2 from the wave emerging side of the holey plate, much like an endoscope [125–127]. Fig. 4.4 depicts the discussed arrangement for $z_1 \approx 0$ at different image planes z_2 . The two spikes together with the transmission coefficient Eq. (4.4) are Fourier transformed in the frequency domain containing diffraction components, whereupon the spatial informations are recovered at the image plane.

The effective medium approach (EMA), that has been applied in order to derive the unitary transmission, Eq. (4.10), makes the negligence of diffraction terms γ valid only when $T_0 \gg T_\gamma$ for $\gamma \neq 0$ is justified. In the subwavelength regime satisfying $\lambda \gg w \gg \Lambda$, it is obvious that the evanescent decay of all diffracted waves for $\gamma \neq 0$ is dominated by the term $\frac{\pi}{\Lambda}$ from $k_x^\gamma = k_x^0 + \frac{2\pi}{\Lambda}\gamma$ along with the attenuating wavenumber $k_z^\gamma = i\sqrt{(k_x^\gamma)^2 - (k_0)^2}$. On the other hand, the specular transmission with k_x^0 is governed by the width of the source $\frac{\pi}{w}$, and together this means that higher-order diffraction waves distort the acoustical image in the extreme near-field zone, $z_2 \approx 0$, which only can be brought to perfection if diffraction can be neglected completely. Those extreme near-field components die much faster out than the specular transmitted wave, provided that $w \gg \Lambda$. In other words, if the distance from the wave emerging interface to the image plane z_2 is increased, the higher-order diffracted waves will fade away, and no longer leave heavy image distortions. Fig. 4.4 illustrates the normalized spatially distributed time averaged pressure field maps $|P/P_{in}|$, along the output surface of the structure for various values of z_2 , from which we can conclude, that the metamaterial posses two near-field zones; the first in which the acoustical image is distorted by the presence of higher order diffracted waves, $z_2 < \Lambda$, and the other one, located in the region $\Lambda < z_2 < w$, where sub-wavelength resolution has prevailed in the image, and diffraction distortions has died out. Clearly the slits, constituting the metamaterials can be seen for those curves corresponding to an image plane at distance smaller than one period away from the output surface, $z_2 < \Lambda$. Even though these results hardly show perfect resolution in terms of featured sharp edges, it is however evident that this holey acoustic metamaterial enables deep subwavelength imaging of those two slits (spikes), at the near-field of the structure. We have checked that at other higher-ordered FP resonances, the perfect image arround, $z_2 \approx \Lambda$, is nicely recovered and is not much affected. Though at the lowest mode, $m = 1$, imaging has been pushed to the highest limit, because with the chosen spike width w the metamaterial provides super resolution, 10 times

smaller than the wavelength, $\lambda = 10w$, able to overcome the diffraction limit five times. The logical question that might appear is, to which extend one can go beyond

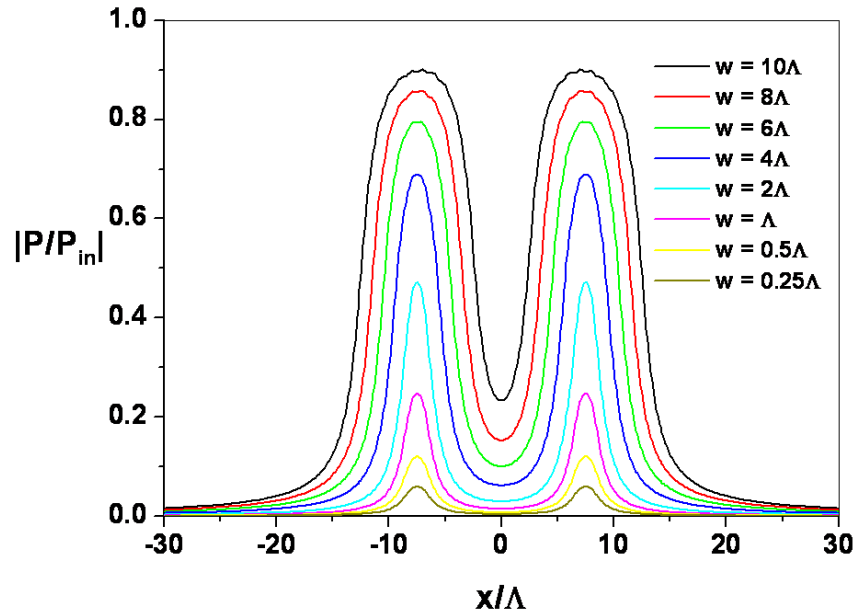


Figure 4.5: $|P/P_{in}|$ at the image plane for a holey metamaterial with the geometries as in Fig. 4.4. Here different images of sources containing varying spike widths are plotted.

the diffraction limit. For metamaterials that acquire their properties from structural and topological features, such as grooves, split ring resonantors (SRRs) or wires, the ultimate resolution or degree in which exotic properties prevails, is the interatomic spacing of those resonant features - the period [53]. Metamaterials consist of those subwavelength structures that collectively, array-wise, respond to any external disturbance of wavelength of the order or larger than the period, which should be in agreement with the natural frequency of those "atoms". Therefore it is expected that the width w of the current dipole or two-slit numerical experiment, should not fall below the the size of the period Λ of the slit array. With the same frequency and geometries from the previous example, see details in the caption of Fig. 4.4, we have varied the value for w , such that the metamaterial acoustically would be irradiated

by two spikes of constant separation s , but different width as can be seen in Fig. 4.5. Clearly we have put the resolution characteristics of the metamaterial based lens to the test. Down to a width of $w = 4\Lambda$ the resolution of the image is still captured, even though the intensity has shrunk approximately 25%. At a width of exactly the interatomic spacing, which is the period Λ of the slit array, most of the details of the subwavelength image is still recovered, even though the intensity has gone down to one third. Decreasing the size further, most of the informations are lost, which indicates that in spite of the intensity lowering for about $w = \Lambda$, the interatomic spacing is the ultimate resolution limit for the slit array acting as a robust imaging device.

If we now go back to the basic structure, presented in Fig. 4.2 we now wish to demonstrate full 3D imaging of a deep subwavelength object. In that respect, we will make use of the knowledge acquired from the previous discussions regarding slit arrays, and the fact that 1D and 2D problems are similar in acoustics, in order to provide the possibility to capture the image of a 3D subwavelength object, by all its near-field components \mathbf{k}_{\parallel} . The geometries of the holey steel block, acting as a imaging device, is given in the caption of Fig. 4.6. For wavelengths $\lambda_{FP} = \frac{2h}{m}$, where standing waves for all parallel wavevector components \mathbf{k}_{\parallel} are excited, we now wish to demonstrate how one is able to channel a subwavelength object (two dots) to the very image plane of the structure. We have checked that almost identical images are obtained, for metamaterials either containing a thickness according to an integer order of $\frac{\lambda}{2}$, $h(m) = m\frac{\lambda}{2}$, or being irradiated at a wavelength according to an integer fraction of twice the thickness, $\lambda(m) = \frac{2h}{m}$ for $m = 1, 2, 3, \dots$. Fig. 4.6 illustrates a particular case where $m = 4$ making the two dots 10 times smaller than the incoming wavelength ($\lambda = \frac{h}{2} = 50\Lambda$), even though we could have chosen the lowest-order FP mode, making the object 40 times smaller compared to the wavelength. What we observe is again reminiscent to the 1D case, in such a way that at exactly the output surface ($z = h$), the acoustic image of the two square dots is heavily distorted by

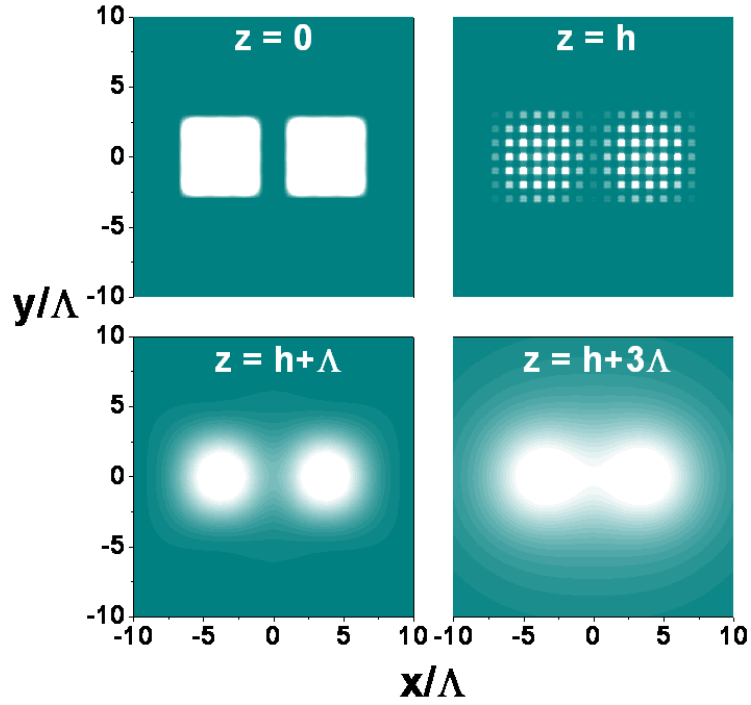


Figure 4.6: Near-field pressurefield $|P(x, y)/P_{in}(x, y)|$ at different image planes, with the geometries a and h of values $\Lambda/2$ and 100Λ respectively such as the wavelength $\lambda = 2h/m = 200\Lambda/m$ with $m = 4$. The source are square dots of size 5Λ times 5Λ and center to center distance 7.5Λ

diffraction effects and the basic units of the metamaterial (i.e., the holes) are visible. However, if now the image plane is moved further away (lower left panel in Fig. 4.6), higher order diffracted modes have died off and a nearly perfect image of the two subwavelength objects is obtained, as Eq. (4.10) predicts. At a distance 3Λ from the output surface (lower right panel in Fig. 4.6), the subwavelength details of the two dots start to disappear. Our numerical results confirm that a holey plate could act as a near-field superlens for acoustic waves with deep subwavelength resolution at a discrete set of resonant wavelengths. As an example, we could choose the unit length Λ to be 2mm and quantify the working frequencies, in terms of a dispersion relation as illustrated in Fig. 4.7. This chosen period for the hole array embedded in, e.g., water, corresponds to a discrete set of acoustic bands, between 2-20 kHz

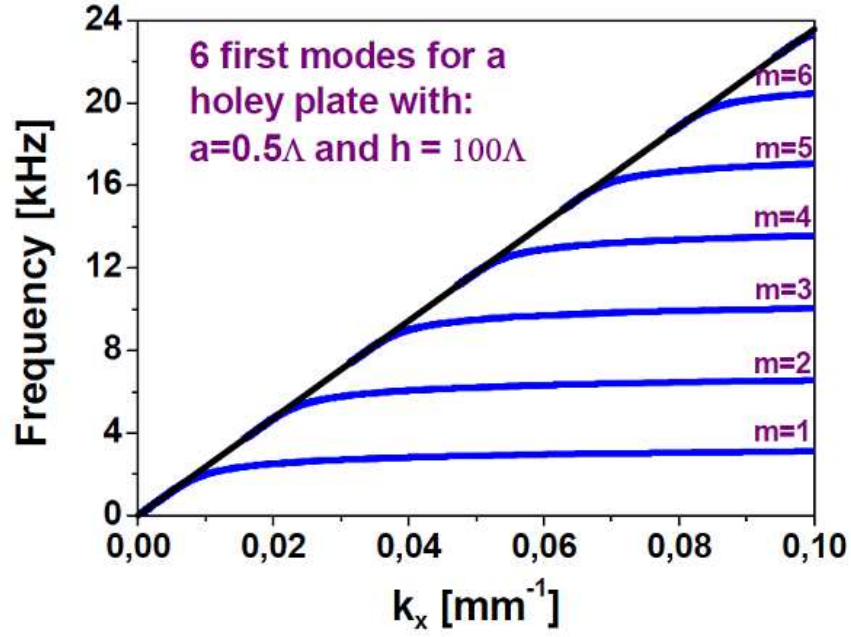


Figure 4.7: Dispersion relation of the standing waves supported by a holey plate embedded in water. In order to work in the KHz regime, the period Λ of the hole array is chosen to be 2mm.

for m ranging from 1 to 6, as illustrated in Fig. 4.7. As the results are scalable by just changing Λ , the operating frequency range of the imaging device can be tuned at will. What the dispersion relation illustrates is nothing new, with the insight acquired from the band diagrams analysis in Chapter 2, it is clear that due to structural periodicity, the bands below the light line can be Bragg-folded into regimes of wave radiation, which means that an external sound field could excite those standing waves of constant phase. This discrete range of flat FP pass bands, would provide the possibility for a broad spectrum of excitations, where each branch m contains all parallel momentum (e.g. in k_x -space), constituting the image of highest resolution.

4.3 Experimental verification

In order to verify the lensing properties of the proposed hole array, acting as a metamaterial, experimental observations have been conducted, in collaboration with the team headed by Prof. Xiang Zhang, UC Berkeley, at the Lawrence Berkeley Laboratory. The intention was to fabricate a structure, possessing a broad range of resonance frequencies and to be able to break the diffraction limit by several means, which in both cases would require the height h of the structure to be very large compared to the period Λ . In order to perform lensing in the kHz regime, we have chosen quadratic apertures, which should not fall below $a = 0.5\text{mm}$, for the sound wave funnelled through the structure at resonance, not to be converted into heat due to viscosity, which is common in narrow fluid tracts. Fig. 4.8 captures the ge-

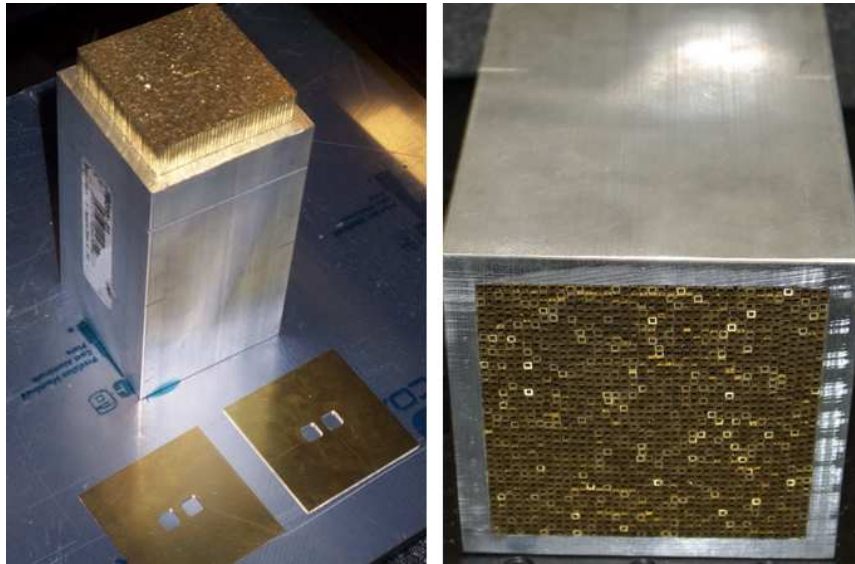


Figure 4.8: Device to perform quasi-perfect acoustic imaging, with a, h being $\Lambda/2$, $h = 100\Lambda$ respectively and the period Λ is chosen to be 1.59 mm. The source are square dots of size $5\Lambda \times 5\Lambda$ and center to center distance 7.5Λ

ometrical parameter chosen. The thickness of the metamaterial, clearly dominates the structure, and made the fabrication in terms of drilling an array of holes into a

solid brass material block of thickness $h = 159\text{mm}$, rather difficult. To make such a structure, 1600 (40x40) square brass alloy 260 tubes were utilized as illustrated in Fig. 4.8. The size of each hole a , lattice constant Λ and tube length h are 0.79, 1.58 and 158mm, respectively. All tubes are parallel clamped together within a 4 inch wide aluminium bushing. Super glue is filled between the tubes to prevent any movement or vibration under acoustical load. The object are two subwavelength quadratic dots, that are carved into a soundhard brass plate, which is put at the input side of the device. At the front side of the object-plate, a 20mm diameter round speaker driven by a Tektronix AFG3021B arbitrary-function generator is placed, which sends out continuous sinusoidal waves. The object-plate together with the mounted speaker, were attached directly and the wave incident side of the hole array ($z_1 \approx 0$), while pressure field scanning was performed, on the wave emerging side, at different distances z_2 . At this side, a 3mm diameter microphone is combined with a three dimensional stepping scanning system to run zigzag routes. Collected signals are amplified with 50dB output gain, then processed by a Tektronix TDS 2002B digital storage oscilloscope and sent to a computer where data is controlled by software (Labview). As mentioned, the source was driven to generate a monochromatic wave, of wavelenghts $\frac{200\Lambda}{m}$. The entire setup with its object and image plane, were surrounded by sound absorbing foam, in order to block the interference of externally sonic disturbances.

Those measurements where performed in the frequency range from 1-5 kHz, corresponding the first four FP resonances in air. Before every field scan was initiated, the transmission peaks through the hole array were spectrally measured, in order to determine the exact frequency value, that would yield a transparent all-angle mode. Fig. 4.9c illustrates the simulation of $|P(x, y)|$ for the two subwavelength dots at $z = h$, which is the exact output interface of the structure. This result is simulated at the second FP mode, corresponding to a frequency of 2.18 kHz and illustrates heavy near-field diffraction that is distorting the image. Fig. 4.9d and

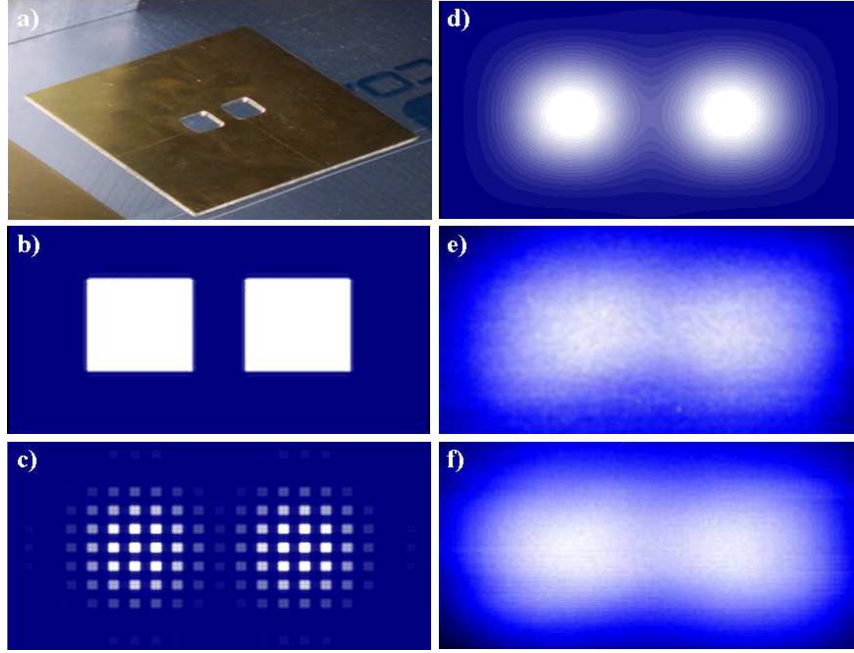


Figure 4.9: Experimental and theoretical results of two subwavelength dots captured by the holey metamaterial surrounded by air. (a,b) The source are square dots of size 5Λ times 5Λ and center to center distance 7.5Λ , the brass sample and calculation respectively. (c) Calculation of $|P(x,y)|$ at the imageplane $z = h$ at a wavelength $\lambda = h$ corresponding to 2.18 kHz. (d) Calculation at $z = h + \Lambda$, $\lambda = h$. (e,f) Measurements at $z = h + \Lambda$ for $\lambda = h$ (2.18 kHz) and $\lambda = h/2$ (4.36 kHz) respectively.

e, capture the subwavelength image at the same operating frequency which makes the two dots 10 times smaller than the wavelength. At a distance Λ away from the wave emerging side of the metamaterial, which is a distance 160.6 mm away from the source, it can be concluded that the agreement between theory and experiment is excellent. At the 4th order FP resonance corresponding to 4.36kHz, as depicted in Fig. 4.9f, we demonstrate the flexibility of the device also being able to capture an subwavelength object at another working frequency. With those observations, it is hereby confirmed together with our theoretical prediction from Eq. (4.10), that the aforesaid hole array can serve as a robust imaging device. Not only are the two dots present as can be seen but also the intermediate stub, here basically illustrated as a

shadow between the two objects, give an unambiguous clue on the imaging quality one can obtain by this holey metamaterial. Again, whilst the results hardly show the sharpest resolution, it is clear that the utilization of a perforated brass slab provides an efficient mean to channel a subwavelength acoustic object to be resolved, into an image plane. In the following, the limiting boundaries of the holey metamaterial,

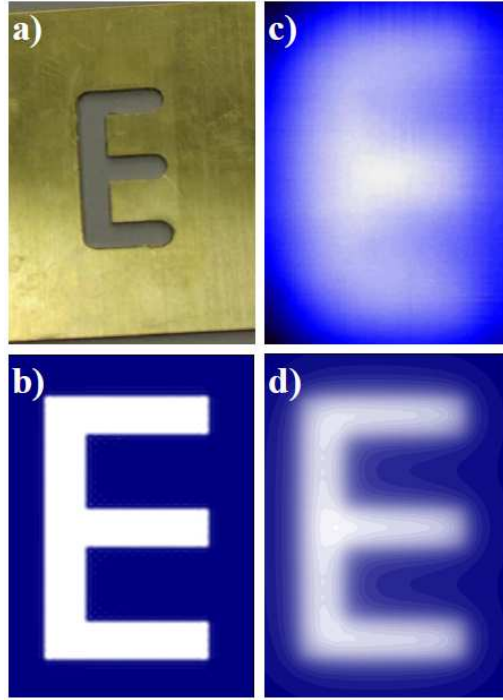


Figure 4.10: Experimental and theoretical results of a subwavelength ($\lambda/37$) "E" captured by the holey metamaterial. (a,b) The letter to be imaged contains a linewidth of 4.76 mm, the brass sample and calculation respectively. (c) Measurement of $|P(x,y)|$ at the imageplane $z = h + \Lambda$ at a wavelength $\lambda = h$ corresponding to 2.18 kHz. (d) Calculation of the image with the same data as in (c).

are intended to be pushed in order to capture even finer subwavelength features. For this purpose we have chosen a letter "E" as a complex subwavelength 3D object, carved into a brass plate as shown in Fig. 4.10a and calculated in Fig. 4.10b. We have chosen a letter of linewidth 4.76 mm that is being irradiated by sound ($m = 2$ FP mode). The scanning output as shown in Fig. 4.10c clearly depicts a distin-

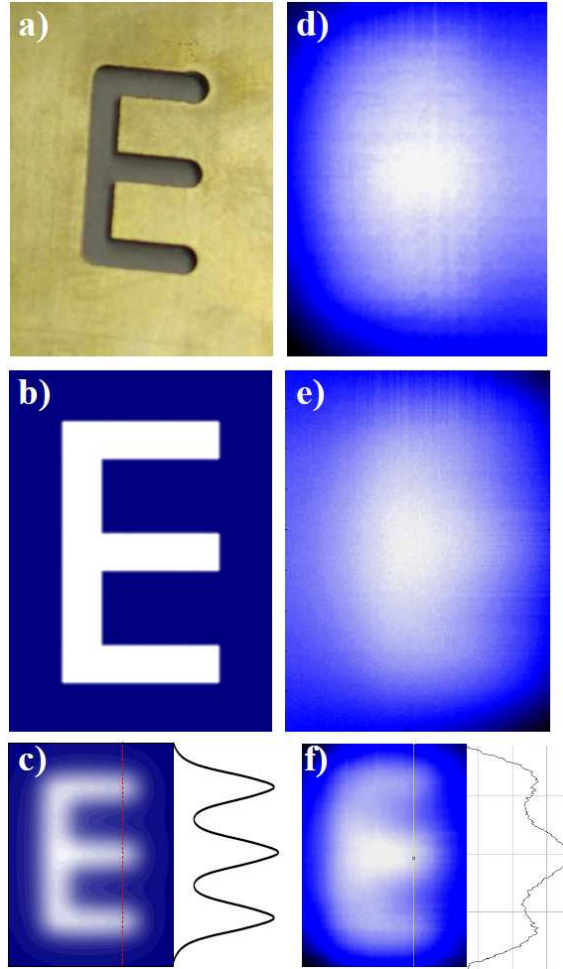


Figure 4.11: Experimental and theoretical results of a subwavelength ($\lambda/50$) "E" captured by the holey metamaterial. (a,b) The letter to be imaged contains a linewidth of 3.18 mm, the brass sample and calculation respectively. (c,f) Measured and simulated spatial surface $|P(x, y)|$ and line $|P(y)|$ plots at $z = h + \Lambda$ for $\lambda = h$ (2.18 kHz). (d) Measurement as in (c) though at $f = 2.42$ kHz. (e) Measurement as in (c) though at $z = h + 3\Lambda$.

guishable shape of the letter, which agrees very well with the simulation, Fig. 4.10d. The evanescent waves contained in this sonic object are carried through the holes, and consequently make a significant contribution to the captured image with deep subwavelength resolution. If we keep the operation frequency fix, we now strive to go further beyond the diffraction limit by taking an "E" of linewidth 3.18 mm . Experiments and simulations in Fig. 4.11c and f are in very good agreement where the line plots represented in those figures, highlight the three bars of the letter of width $\lambda/50$. In addition we have conducted some control experiments, i. o. to study the limits of the imaging capability of the holey metamaterial. Varying the operating frequency (Fig. 4.11d) or moving the image plane further away (Fig. 4.11e) shows a decreased lensing capability with an almost entire loss of resolution. The holey structure now is detuned and monochromatically not excited as resonance. However, by the right design concerning geometrical parameters or even hole-fillings, one can extend the properties contained in the metamaterial at will.

4.4 Summary and outlook

Fig. 4.12 illustrates a comparison between the acoustic equivalence of Pendry's perfect lens and the holey metamaterial which we have presented through out this chapter. The perfect lens would give rise to an amplification of the near-field components of an object, and transpose them on the order of half the lens thickness, into the imageplane [129]. However, this type of acoustic perfect lens has so far not seen the day of light, and still remains a difficult challenge to be faced for acoustic metamaterial designer. The imaging device which we have proposed, constitutes a bulk metamaterial that can capture a subwavelength image for a broad range of discrete frequencies, matched to the standing wave modes supported by the holey block. The experiments shown are in very good agreement with the results that are calculated, and in that sense, we have demonstrated deep subwavelength imaging of complex

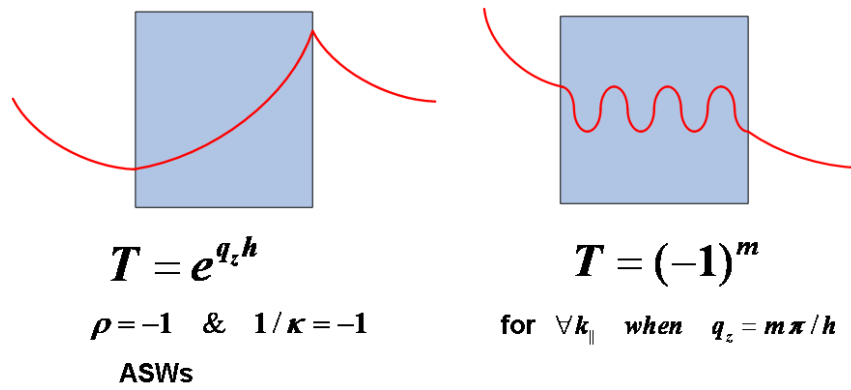


Figure 4.12: Pendry's perfect lens for sound comprising a growth of an evanescent wave versus a DC-like mode lens which we have detailed in this chapter.

structures 50 times smaller than the wavelength. Measurements did also highlight the limits of the structure when it, e.g., was irradiated off-resonance or when the field scan of the image was performed at a greater distance from the metamaterial. Apart from its fundamental interest, the findings could be utilized for improving medical ultrasonic imaging for scanning and diagnosis purposes, such as for non-destructive detection of cracks in alloy materials, among others. However, there is still room for improvements of the structure, that in particular is important when an image is to be resolved in the far-field. Also realistic applications do rely on transient pulses, rather than mono-frequency operation.

Chapter 5

Broadband all-angle blockage of sound by a double-fishnet structure

The previous chapter, reporting on the imaging capabilities of structured materials, already gave the reader a clue on how long-standing work on artificial magnetism and plasmas has defined the role of EM-metamaterials as a forerunner and motivator, regarding the study on tailoring the attributes of propagating sound. Even though the range of EM material response found in nature only represents a small fraction of that, which is theoretically possible, this limited range can be extended by the use of artificially structured materials. In single negative (SNG) metamaterials, either (but not simultaneously) the permittivity ε (epsilon negative (ENG) media) or the permeability μ (mu negative (MNG) media) is negative. One prominent application of those two concepts are the LHMs, which basically are double negative (DNG) metamaterials. In the first experiment on negative refraction, R. A. Schelby et al. [52] measured the refracted angle of a transmitted microwave beam through a DNG prism that was made out of an array of metallic wires (ENG) and SRRs (MNG but

also ENG [131]). In this chapter, we will solely concentrate on SNG media, consequently a brief review on EM SNG media such as the progress made for the acoustical counterpart will be given in the following. In the late 90s, John Pendry introduced the concept to alter functions by changing a materials internal structure on a very small scale, less than the wavelength of the impinging light. In that respect splitting resonators (SRRs), that are a pair of concentric annular or quadratic loops with splits in them at opposite ends, were proposed. Those structures are intrinsically not magnetic but can be tuned, effectively to exhibit artificial magnetism [50, 54]. Also altering the level of the electrical response of metals by means of artificially manufactured structures, has shown to be a valid mean in the world of metamaterials. SPPs which are propagating on metallic surfaces in the visible and near UV range can be tailored to propagate at much lower frequencies, such as in the GHz regime. Very thin metallic wires, assembled into a periodic lattice, composing a micro-structure, will support GHz plasmons bound to the surface, which can be controlled by the local geometry [49]. In that respect, a plasma frequency can be tuned, below which little light can be transmitted, due to single negativity as of being a ENG medium. Optical but also radar absorbing man made materials, obviously motivated new interest in the field of acoustics in order to design resonance based sonic attenuators. To this degree, two milestone papers on SNG structures can be named that has sparked significant interest and followers, both in terms theory and experimental observations. Liu et al. designed the so-called locally resonant phononic crystals, consisting of rubber coated lead spheres, and arranged into a 3D crystal [3]. The ground breaking feature of this composite lies in the negative effective mass density over certain frequency ranges, thus breaking the constraints, governed by the conventional mass density law of sound propagation. The researchers found the existence of two wide attenuation bands, centred around 0.4 and 1.3 kHz, which corresponds to the spectrally measured transmission dips. In 2006, Fang et al. put the effective bulk modulus to the test. Helmholtz resonators that have widely been used as bandstop

filters due to the oscillation of air in the neck with the compressibility in the cavity, which at resonance absorb all sound, have been tuned to act at a wavelength much smaller than this structure [63, 75, 62]. In an array of those resonators, the authors excited this structure at the right ultrasonic tone (32.5 KHz in water), giving rise to full sound attenuation due to a resonant single negativity (real part of the effective bulk modulus less than zero $\text{Re}(1/\kappa < 0)$).

In the following we design a metamaterial that is the acoustical analogue of the double-fishnet structure recently analyzed in Optics. Two adjacent holey plates are predicted to support a gap mode which is responsible of a forbidden band, characterized by a negative effective bulk modulus. This acoustic metamaterial exhibits a weak dispersion with parallel momentum so the regime of strong attenuation appears for a broad range of angles of incident sound. Compared to those two highlighted examples from the literature, we will show how the acoustic fishnet structure in its simplest sense, can be manufactured by two adjacent hole arrays.

5.1 Modal expanding the acoustic double-fishnet structure

Fig. 5.1 illustrates a schematic drawing of the acoustical version of the double fishnet structure. Recent interest in LHM has sparked the desire to create efficient structures such as the gap material and metallic wires composite: Double-fishnet structure. In 2005, Zhang and co-workers demonstrated negative refraction of light in the near-IR regime [132] which later was extended to visible frequencies [133–135]. In the same framework, detailed theoretical explanations in terms of lumped-parameter models and full modal analysis were given [136, 137]. In the following we will derive the ME for the structure given in Fig. 5.1, which is a perfect rigid structure (steel, brass or concrete) that, e.g., is surrounded by air. We follow up with the theory employed in section 2.7 from Chapter 2 upon modelling hole arrays, and start out with Region

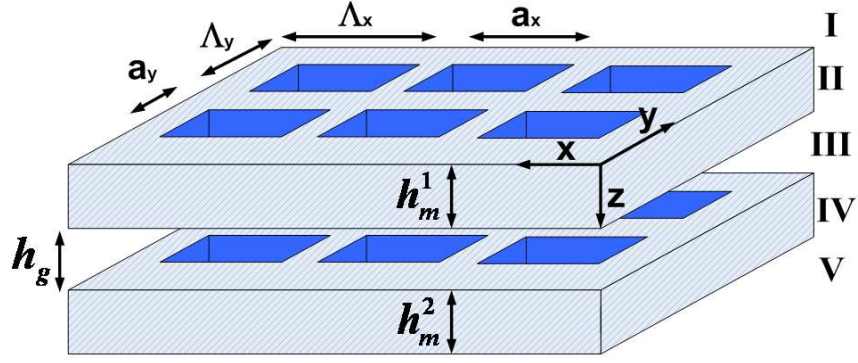


Figure 5.1: Schematics of an acoustic double-fishnet structure, made out of a perfect rigid body, impenetrable for air-borne sound waves impinging on the structure.

I , the zone of sound irradiation:

$$\begin{aligned}
 |p^I(z)\rangle &= Y_{k_z^0}^I |\mathbf{k}_{\parallel}^0\rangle e^{ik_z^0 z} + \sum_{\beta=-\infty}^{\infty} R_{\beta} Y_{k_z^{\beta}}^I |\mathbf{k}_{\parallel}^{\beta}\rangle e^{-ik_z^{\beta} z} \\
 |v_z^I(z)\rangle &= |\mathbf{k}_{\parallel}^0\rangle e^{ik_z^0 z} - \sum_{\beta=-\infty}^{\infty} R_{\beta} |\mathbf{k}_{\parallel}^{\beta}\rangle e^{-ik_z^{\beta} z}.
 \end{aligned} \tag{5.1}$$

For a detailed explanation of the quantities and functions involved one should review section 2.7. Region II again is represented as a sum over hole waveguide modes, hence the pressure and velocities read:

$$\begin{aligned}
 |p^{II}(z)\rangle &= \sum_{\alpha} Y_{q_z^{\alpha}}^{II} (A_{\alpha}^{II} e^{iq_z^{\alpha} z} + B_{\alpha}^{II} e^{-iq_z^{\alpha} z}) |\alpha\rangle \\
 |v_z^{II}(z)\rangle &= \sum_{\alpha} (A_{\alpha}^{II} e^{iq_z^{\alpha} z} - B_{\alpha}^{II} e^{-iq_z^{\alpha} z}) |\alpha\rangle.
 \end{aligned} \tag{5.2}$$

The two metallic plates are separated by a fluid gap of thickness h_g wherein waves freely can scatter. The wave running in the positive and negative direction along the z -axis are weighted by a discrete set of diffraction amplitudes, Γ such as τ respectively:

$$\begin{aligned}
 |p^{III}(z)\rangle &= \sum_{\beta} Y_{k_z^{\beta}}^{III} (\tau_{\beta} e^{ik_z^{\beta}(z-\varphi_a)} + \Gamma_{\beta} e^{-ik_z^{\beta}(z-\varphi_a)}) |\mathbf{k}_{\parallel}^{\beta}\rangle \\
 |v_z^{III}(z)\rangle &= \sum_{\beta} (\tau_{\beta} e^{ik_z^{\beta}(z-\varphi_a)} - \Gamma_{\beta} e^{-ik_z^{\beta}(z-\varphi_a)}) |\mathbf{k}_{\parallel}^{\beta}\rangle.
 \end{aligned} \tag{5.3}$$

The in-plane diffracted waves inside the gap $\mathbf{k}_{\parallel}^{\beta}$, are spatially phase shifted along the z -axis, of the order $\varphi_a = h_m^1$, in relation to scattering taking place in Region I . Region IV again comprise waveguide modes inside the lower hole array of thickness h_m^2 , where pressure $p(z)$ and the z -component of the velocity $v_z(z)$ are given as

$$\begin{aligned} |p^{IV}(z)\rangle &= \sum_{\alpha} Y_{q_z^{\alpha}}^{IV} (A_{\alpha}^{IV} e^{iq_z^{\alpha}(z-\varphi_b)} + B_{\alpha}^{IV} e^{-iq_z^{\alpha}(z-\varphi_b)}) |\alpha\rangle \\ |v_z^{IV}(z)\rangle &= \sum_{\alpha} (A_{\alpha}^{IV} e^{iq_z^{\alpha}(z-\varphi_b)} - B_{\alpha}^{IV} e^{-iq_z^{\alpha}(z-\varphi_b)}) |\alpha\rangle, \end{aligned} \quad (5.4)$$

with $\varphi_b = h_m^1 + h_g$. In the wave emerging region, we straightforwardly can write the transmitted waves as a sum over Bloch-modes:

$$\begin{aligned} |p^V(z)\rangle &= \sum_{\beta=-\infty}^{\infty} T_{\beta} Y_{k_z^{\beta}}^V |\mathbf{k}_{\parallel}^{\beta}\rangle e^{ik_z^{\beta}(z-\varphi_c)} \\ |v_z^V(z)\rangle &= \sum_{\beta=-\infty}^{\infty} T_{\beta} |\mathbf{k}_{\parallel}^{\beta}\rangle e^{ik_z^{\beta}(z-\varphi_c)}, \end{aligned} \quad (5.5)$$

with phase constant $\varphi_c = h_m^1 + h_g + h_m^2$. In order simplify the modelling approach and to gain physical insight into this problem, it is worth developing a minimal model in which only the first eigenmode $\alpha = 0$ inside the holes is introduced in the modal expansion. This mode does not present cutoff and hence its propagation constant coincides with the free space wavenumber, $k_0 = 2\pi/\lambda$. We have checked that this single mode approach is a very good approximation when $\lambda > \Lambda \gg a$. Also for this system, at all interfaces as it has been extensively elaborated in Chapter 2, we impose continuity of the appropriate fields while matching the modes at their respective spatial locations. With the indices 1, wave coupling, bouncing and radiation is linked to the hole array facing the incident radiation, whereas 2 relates to the structure at wave emerging side. In the absence of a prime, the modal velocity v is represented at the input side, either at plate 1 or 2, where the primed velocity v' is devoted to

the output side. Hence, the system of equations read as follows:

$$\begin{array}{l} (G_1 - \epsilon_1)v_1 - G_1^V v_1' = I^0 \\ (\Psi + \epsilon_1)v_1' + \Phi v_2 + G_1^V v_1 = 0 \\ (\Psi + \epsilon_2)v_2 + \Phi v_1' + G_2^V v_2' = 0 \\ (G_2 - \epsilon_2)v_2' - G_2^V v_2 = 0 \end{array}, \quad (5.6)$$

with the illumination term representing sound irradiation via the fundamental waveguide mode

$$I^0 = 2iY_{k_z^0}^I S_{00}, \quad (5.7)$$

such as the interface coupling functions at a given hole array, 1 or 2

$$G_1^V = \frac{Y_{q_z^0}^{II}}{\sin q_z^0 h_m^1}, \quad G_2^V = \frac{Y_{q_z^0}^{IV}}{\sin q_z^0 h_m^2}. \quad (5.8)$$

The bidirectional bouncing back-and-forth terms with respect to the appropriate hole arrays read:

$$\epsilon_1 = \frac{Y_{q_z^0}^{II}}{\tan q_z^0 h_m^1}, \quad \epsilon_2 = \frac{Y_{q_z^0}^{IV}}{\tan q_z^0 h_m^2}, \quad (5.9)$$

whereas the coupling functions, linking diffracted waves to the waveguide modes are nothing but:

$$G_1 = i \sum_{\beta=-\infty}^{\infty} Y_{k_z^\beta}^I |S_{\beta 0}|^2, \quad G_2 = i \sum_{\beta=-\infty}^{\infty} Y_{k_z^\beta}^V |S_{\beta 0}|^2. \quad (5.10)$$

The scattering which is taking place inside the fluid gap, that is linking the entire incident acoustic field to the wave emerging side, is governed by the two functions:

$$\Psi = \sum_{\beta=-\infty}^{\infty} \frac{Y_{k_z^\beta}^{III}}{\tan k_z^\beta h_g} |S_{\beta 0}|^2 \quad (5.11)$$

and

$$\Phi = \sum_{\beta=-\infty}^{\infty} \frac{Y_{k_z^\beta}^{III}}{\sin k_z^\beta h_g} |S_{\beta 0}|^2. \quad (5.12)$$

Eqs. (5.6) with the constituting functions Eqs. (5.7-5.12) unifies the entire wave interaction process under the same umbrella, when sound in the long wavelength limit is funnelled through a stack of two hole arrays. We could extend this concept to fishnet structures of n layers as this only would imply an increased number of interfaces that would be needed to be matched and add slight additional costs in terms of computation. In order to conquer physical insight into this new acoustical waveguide, we focus the study on two adjacent hole arrays, making it the simplest version of a double-fishnet structure for sound waves. The unknown modal velocity fields from the system of linear equations, Eqs. (5.6), have been defined in the following way:

$$v_1 = A_0^{II} - B_0^{II} \quad (5.13)$$

$$v'_1 = -(A_0^{II} e^{iq_z^0 h_m^1} - B_0^{II} e^{-iq_z^0 h_m^1}) \quad (5.14)$$

$$v_2 = A_0^{IV} - B_0^{IV} \quad (5.15)$$

$$v'_2 = -(A_0^{IV} e^{iq_z^0 h_m^2} - B_0^{IV} e^{-iq_z^0 h_m^2}). \quad (5.16)$$

5.2 Transmission study

Single holey plates have been examined mainly in connection with the emergence of the phenomenon of extraordinary wave transmission through subwavelength apertures in acoustic systems, as we elaborated in Chapter 2. In that chapter we referred to configurations employed in recent experiments containing plates made of steel, brass (sound-hard materials) or aluminum (sound-soft), which were perforated with holes forming a square lattice with periods in the range of 2 - 7 mm, supporting transmission resonances that range from the kHz to the MHz frequency regimes [94, 97]. In single holey plates, two resonant transmission mechanisms coexist. One

is associated with the excitation of FP modes inside the holes whose spectral locations are then controlled by the thickness of the plate. The other mechanism relies on the coupling between the incident sound wave and acoustic surface waves confined at the horizontal surfaces of the plate (Chapter 2).

A sketch of an acoustic double-fishnet (ADF) structure is depicted in Fig. 5.1. Two plates of equal thickness $h_m = h_m^1 = h_m^2$ are perforated with a square array (period $\Lambda = \Lambda_x = \Lambda_y$) of square holes of side $a = a_x = a_y$. These two holey plates are separated by a thin layer of thickness h_g filled with a fluid characterized by a sound velocity c_g and mass density ρ_g . As we have mentioned in section 5.1, in our calculations we assume that the surrounding medium is air (sound velocity, c_0) and that the plates are made of steel or brass in which the perfect rigid body approximation is very accurate. Within this approach, the same scattering properties are obtained in different frequency regimes by properly scaling all the geometrical parameters with the same factor. Due to that, in our calculations, we will use Λ as the unit length defining the structure. In Fig. 5.2 we render the normally-incident transmis-

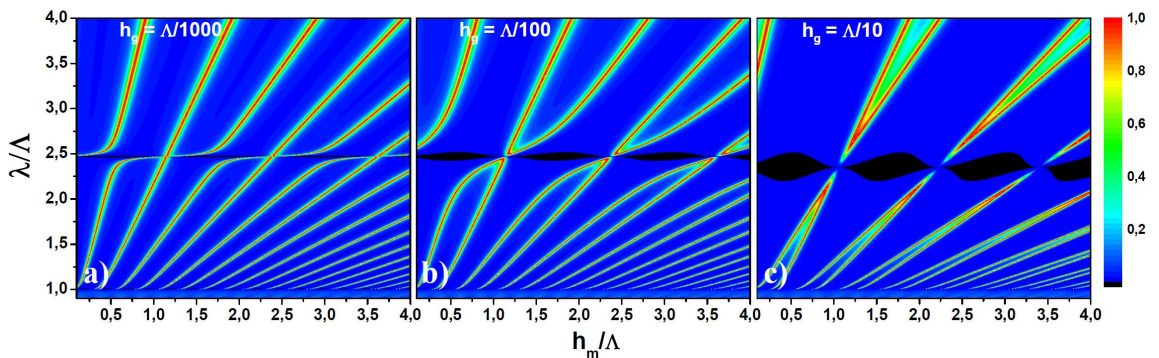


Figure 5.2: Normalized-to-unit cell transmittance spectra as a function of λ and h_m , both in units of Λ . In the three panels, $a = \Lambda/3.75$ and three different values of h_g are studied: $h_g = \Lambda/1000$, $\Lambda/100$ and $\Lambda/10$. The incident sound plane wave is impinging at the normal direction.

sion spectra for three different values of the gap thickness, $h_g = \Lambda/1000$, $\Lambda/100$ and $\Lambda/10$. The side of the square holes is fixed at $a = \Lambda/3.75$ and the gap material is

assumed to be air. In the three panels, the dependence of the transmittance with wavelength and plates' thickness, h_m , is displayed. In the case of an extremely thin gap layer (Fig. 5.2a), the transmission spectra almost resemble those corresponding to holey plates of total thickness $2h_m$, see, e.g., Fig. 2.16 from Chapter 2 (though with other geometries). In this case, FP resonant modes appear at wavelengths close to $\lambda = 4h_m/m$, with m an integer. In addition to these transmission resonances, a new resonant feature leading to an anticrossing emerges at around $\lambda = 2.45\Lambda$. An inspection of the pressure field distribution associated with this new resonance reveals that this mode is strongly localized at the gap region. Importantly, this gap mode seems to couple only with the odd FP modes ($m = 1, 3, 5\dots$). When h_g is increased, the coupling between the odd FP modes and the gap mode is enlarged and the spectral locations of these hybridized modes tend to merge with those of the even FP modes that remain almost unaltered as a function of h_g . The coupling between the FP modes and the gap resonance as observed in Fig. 5.2 can be explained by looking at the symmetry of the non-trivial solutions of the homogeneous version of the system of Eqs. (5.6). In other words, in order to seek bound mode solutions of definite symmetry, the system is now driven by an evanescent wave. The modal solutions that display a symmetric (even) distribution correspond to $v_1 = -v'_2$ and $v'_1 = -v_2$, which is in accordance to the definitions given previously. This yields the following condition for a zero in the real part of the determinant:

$$(\text{Re}(G) - \epsilon)(\Psi - \Phi + \epsilon) + (G^V)^2 = 0. \quad (5.17)$$

All the magnitudes appearing in Eq. (5.17) are real quantities except G , whose imaginary part measures the coupling of the waveguide mode inside the holes with the radiative mode in Region I and V . In the limit of a very thin gap layer, $h_g \rightarrow 0$, $\Psi \approx \Phi$ (see Eq. (5.11) and Eq. (5.12)) and the resonant condition reads:

$$\text{Re}(G) = -\frac{1}{\epsilon}, \quad (5.18)$$

which is independent of h_g . As $\text{Re}(G)$ scales as $(a/\Lambda)^2$, in the limit of small holes this condition reads $1/\epsilon = 0$, which is fulfilled for

$$\lambda = \frac{2h_m}{l} = \frac{4h_m}{m} \quad (5.19)$$

with l integer. As expected, these resonant wavelengths correspond to the even solutions for the FP modes of a holey plate of total thickness $2h_m$, explaining why the even FP modes do not couple with the gap resonance, as observed in Fig. 5.2.

When searching for anti-symmetric (odd) solutions ($v_1 = v'_2$ and $v'_1 = v_2$), the condition for a zero-determinant is now:

$$(\text{Re}(G) - \epsilon)(\Psi + \Phi + \epsilon) + (G^V)^2 = 0, \quad (5.20)$$

that can be rewritten as:

$$\text{Re}(G) = \epsilon - \frac{(G^V)^2}{\Psi + \Phi + \epsilon}. \quad (5.21)$$

The important point to notice is that, in the limit $h_g \rightarrow 0$, $\Psi + \Phi \approx 2\Psi$ is proportional to $1/h_g$. Therefore, in most of the spectral range for very small gap separations h_g , $\Psi + \Phi \rightarrow \infty$. Physically, this means that there is no space available in the ultra-thin gap layer to accommodate a change of sign in the pressure field. The resonant condition for odd solutions reads:

$$\text{Re}(G) = \epsilon, \quad (5.22)$$

that is fulfilled when:

$$\lambda = \frac{4h_m}{2l + 1}, \quad (5.23)$$

l integer, for very small holes. This is exactly the condition for odd FP modes $(2l+1)$ of a holey plate of total thickness $2h_m$. However, in Eq. (5.21), there is an additional resonant condition associated with a zero in the denominator, $\Psi + \Phi = -\epsilon$. This corresponds to a solution in which $v_1 = v'_2 = 0$, i.e., an odd mode that is confined at the gap region between the two holey plates. Importantly, as it can be worked out within the minimal model, its spectral linewidth enlarges for increasing h_g , this being

responsible for the enhancement in the coupling between the gap and the odd FP resonances when the hole pates separate. The interplay between this gap mode and the odd FP modes leads to the complex behaviour of the transmittance observed in Fig. 5.2. Furthermore, when the odd FP modes and the gap mode hybridize,

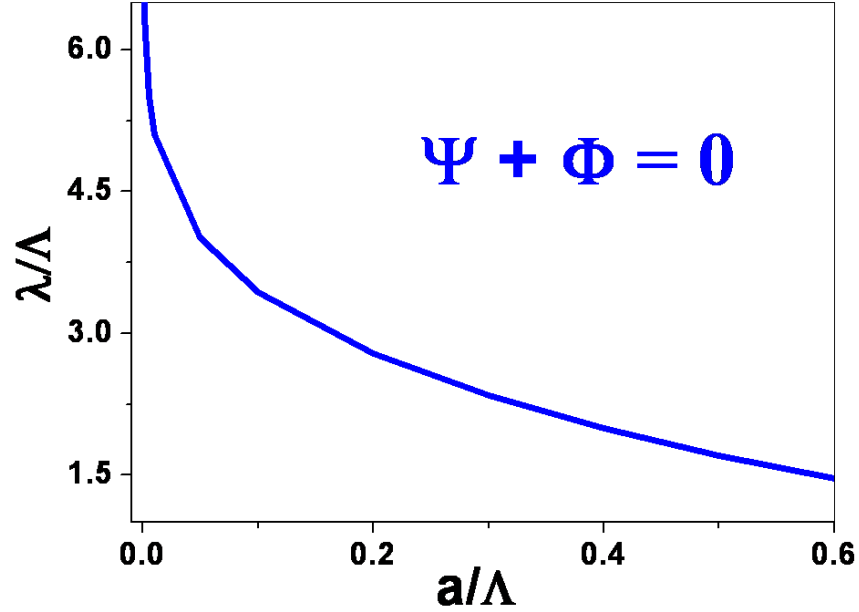


Figure 5.3: The evolution of the gap resonance at normal incidence, $\Psi + \Phi = 0$, is displayed as a function of the wavelength λ and the square aperture size $a = a_x = a_y$.

one obtains the condition $(\Psi + \Phi) = 0$, which isolates the resonance supported by the gap. This equation which we have plotted in Fig. 5.3 shows how the resonant location of the gap mode, subtle can be tuned by the size of the holes.

5.3 Negative effective bulk modulus and its angular sensitivity

In the following we shall apply a retrieval technique, to determine the effective acoustical constitutive parameters for the designated structure. We have employed the

method from D. R. Smith et al. and slightly modified for the use of sound waves [138]. For a wave to exhibit full attenuation inside a material, the structure can be made out of a SNG-metamaterial which gives rise to a imaginary propagation constant. Passivity in the ADF requires positive imaginary constant in both the effective mass density ρ such as the bulk modulus $1/\kappa$. We have checked that for this present structure the real part of the effective mass density is always positive, making the structure, unlike for its EM counterpart, impossible for the emergence of a negative refraction. This can be ascribed to the lack of cutoff for sound propagation inside the holes, whereas the existence of a cutoff for EM waves leads to a Drude behaviour for the electric permittivity [28].

In order to analyse the link between transmission resonances and the effective $1/\kappa$, we have fixed the plates' thickness at $h_m = \Lambda/1.875$, in this case, the spectral location of the gap mode lies exactly within the $m = 1$ odd FP resonance (see Fig. 5.2a). As in Fig. 5.2, three different values of h_g are studied and rendered in Fig. 5.4: $h_g = \Lambda/1000$, $\Lambda/100$ and $\Lambda/10$. Regarding the effective ρ , as mentioned this magnitude is always positive and does not present any resonant feature. However, for a very thin gap layer, a region of negative $1/\kappa$ emerges and its location coincides with the transmission dip originated by the weak coupling between the gap mode and the first odd FP mode. The consequence of a negative compressibility in the fluid element comprised by the unit cell (hole perforation plus gap), is the overall expansion as a reaction to a positive external pressure (compression). This type of negative response has been demonstrated in a recent experiment for a 1D structure [62]. As h_g is increased, the region of negative $1/\kappa$ is greatly enlarged as a result of a stronger coupling between the two modes, which can be seen in Fig. 5.4c. Therefore, our results suggest that in an ADF metamaterial the spectral linewidth of the attenuation band can be easily tuned by varying the separation between the two holey plates. In the spectral regimes of vanishing transmittance, as seen in Fig. 5.4, unambiguously the suppression of sound radiation is caused by the fact that the ADF

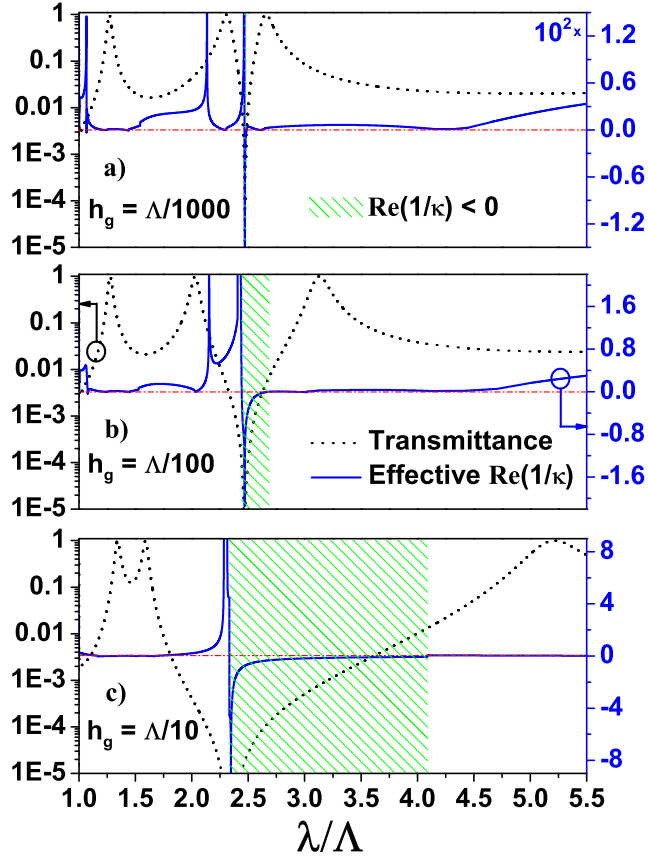


Figure 5.4: Normalized-to-unit-cell transmittance for normal incidence (black dotted lines) and real effective bulk modulus, $\text{Re}(1/\kappa)$, (blue curves) for an ADF structure of square holes $a = \Lambda/3.75$ and gap separations $h_g = \Lambda/1000$, $\Lambda/100$ and $\Lambda/10$, respectively. In the three cases, the plates' thickness is fixed at $h_m = \Lambda/1.875$. The green shaded area highlights the area of negative $\text{Re}(1/\kappa)$.

structure constitutes a SNG metamaterial, devoted to the real part of the effective bulk modulus being less than zero, $\text{Re}(\frac{1}{\kappa}) < 0$.

When thinking in possible applications of ADFs for sound blockage, the dispersion of its attenuation band with the angle of incidence is valuable studying. Moreover, this type of analysis is mandatory for measuring the validity of the effective medium approach. First though, we choose to plot the transmittance dispersion relation that maps all possible solutions on a contour for different parallel momenta, see Fig. 5.5. It is important to notice that the wide band gap (black zone) between the first two

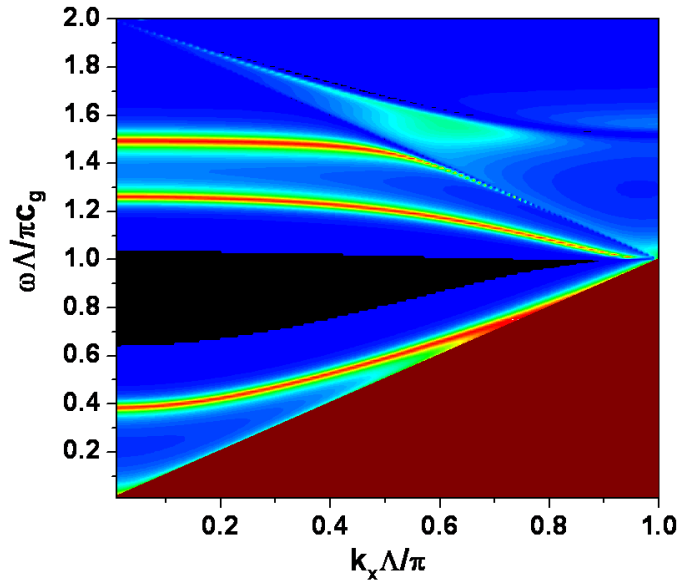


Figure 5.5: Transmittance dispersion with respect to the parallel momentum containing all solutions supported by the ADF structure. The geometrical parameters are: $a = \Lambda/3.75$, $h_m = \Lambda/1.875$ and $h_g = \Lambda/10$, as in Fig. 5.4c.

lowest modes, does not stem from Bragg scattering. This flat dispersion-less zone rather originates from a negative effective bulk modulus resonance, entrained in the excitation of a gap mode. As shown in Fig. 5.6a, the width of the forbidden band, Δ in wavelength units, is greatly enlarged for increasing h_g as a result of a stronger coupling between the modes as we explained above. With Fig. 5.6b we plot the evolution of the spectral locations of the symmetric and asymmetric modes, along with the region of negative $1/\kappa$ as a function of the angle of incidence, for the case depicted in Fig. 5.4c ($h_m = \Lambda/1.875$ and $h_g = \Lambda/10$). The symmetric (even FP modes) dispersion band is calculated with Eq. (5.17) whereas the asymmetric ones (odd FP and gap modes) originates from Eq. (5.20). As a difference with its optical counterpart [137], all the resonant modes and, consequently, the region of negative bulk modulus show very little dispersion with parallel momentum. The region of negative $1/\kappa$ is maintained for angles of incidence as large as 80° , although its bandwidth is reduced

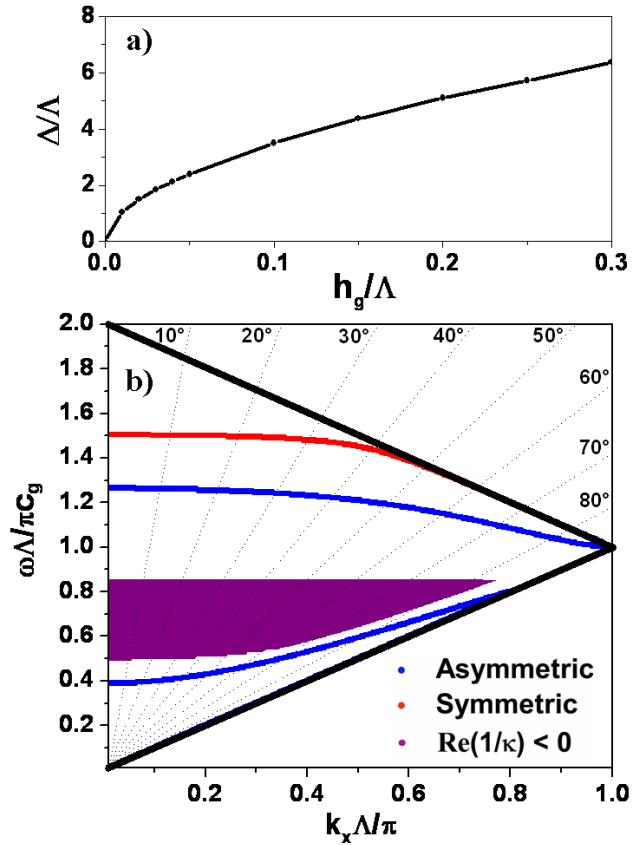


Figure 5.6: (a) Dependence of the wavelength width of the attenuation band, Δ , with the gap thickness, h_g , for normal incidence. (b) Dispersion with respect to the parallel momentum of the symmetric (red curve, from Eq. (5.17)) and asymmetric (blue lines, from Eq. (5.20)) modes and the region of negative $\text{Re}(1/\kappa) < 0$ (purple area). The geometrical parameters are: $a = \Lambda/3.75$, $h_m = \Lambda/1.875$ and $h_g = \Lambda/10$, as in Fig. 5.4c. Dotted lines show the dispersion of incoming plane waves for different angles of incidence.

with respect to the normal incident case. This result validates the use of an effective medium approach for describing the scattering properties of an ADF metamaterial. From the practical point of view, our finding reinforces our claim that an ADF can operate as a tunable acoustical device presenting a broadband, all angle attenuation of sound. Importantly, the spectral location of this forbidden band and its linewidth can be engineered by changing the period of the hole array and the thickness of the gap layer placed between the two holey plates. In that same respect, the location of the resonance can be tuned with an gap-filling fluid different from the one in the

holes and the background.

5.4 Fano resonance interpretation

In the following section, we wish to introduce another interpretation of the resonance mechanism involved, which is giving rise to the forbidden bands of complete sound attenuation as we saw before. We will take a close look at an example, which

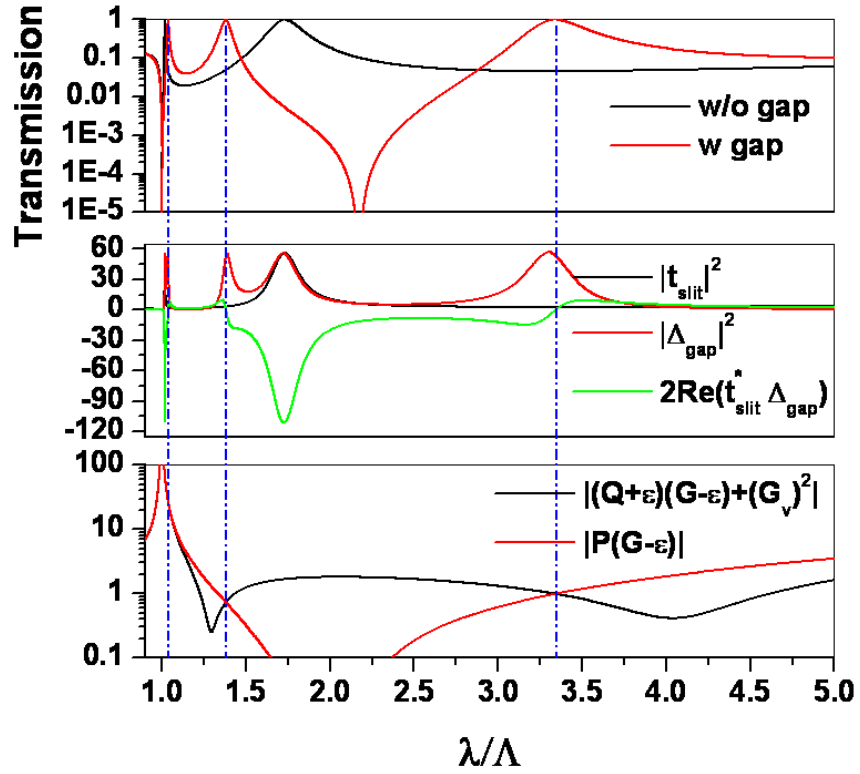


Figure 5.7: Transmittance and determinant spectra such as a Fano resonance interpretation for an ADF structure of geometries: $h_m^2 = h_m^1 = a_x = a_y = \Lambda_x/3 = \Lambda_y/3 = \Lambda/3$ such as $h_g = 0.07\Lambda$. The blue vertical dash-dotted lines match all allowed solutions.

corresponds to an ADF metamaterial of geometries $h_m^2 = h_m^1 = a_x = a_y = \Lambda_x/3 = \Lambda_y/3 = \Lambda/3$ such as $h_g = 0.07\Lambda$. In the upper panel of Fig. 5.7 we have mapped the transmittance spectra in the presence ($h_g \neq 0$) and the absence ($h_g = 0$) of a gap.

In here the logarithmic scale is chosen to demonstrate the opaque nature associated to the transmission minima. From Eqs. (5.6), one easily can derive an analytical expression for the determinant, which helps seeking for the non-trivial solutions giving rise to full transmission, that agree very well as illustrated in the lower and the upper panel of Fig. 5.7. We have seen (section 5.3) that the transmittance dip is related to an exotic acoustical property embedded in the ADF structure, which we have attributed to a single negativity, as of the real effective bulk modulus having a value less than zero. In here, we want to obtain full understanding of the transmission maxima that can be understood in a different way, compared to the previous symmetry study. To this, we shall derive a minimal-model which basically adds the contribution from the array of holes t_{hArr} and the plate separation (gap) Δ_{gap} to the overall transmittance: $t = t_{hArr} + \Delta_{gap}$. The absolute value of this transmission is of particular interest, which reads:

$$|t|^2 = |t_{hArr}|^2 + |\Delta_{gap}|^2 + 2\text{Re}(t_{hArr}^* \Delta_{gap}). \quad (5.24)$$

The decomposition of Eq. (5.24), allows to separate explicitly the resonant and nonresonant parts of t . It is important to note that this expression closely resembles a Fano-type formula, in which two different mechanisms (resonant and nonresonant channels) interplay in the final transmission process. The nonresonant part can be regarded as the first term in Eq. (5.24), which simply is the transmission data originated from a hole array, $h_g = 0$. The resonant channel in the Fano picture, is provided by the second term, which is the resonant contribution of sound wave encompassing the gap spacing between the hole arrays. The interference between the resonant and nonresonant channel in the Fano approach, is explained by the last term in Eq. (5.24). The contribution of those channels given with Eq. (5.24), can clearly be seen in the middle panel of Fig. 5.7. The resonant and nonresonant channels coincides very well with the transmission spectra for the ADF structure and the hole array respectively. It is also very interesting to see how the interference term, $2\text{Re}(t_{hArr}^* \Delta_{gap})$, changes its sign as in typical resonance phenomena, which

in this particular case takes place at all transmission maxima in the spectrum for the ADF structure. The narrower the transmission peak is, the faster the sign change in the interaction term appears. Note also how the spectral location of this interaction agrees with the non-trivial solution plotted in the lower panel of Fig. 5.7 (blue vertical dash-dotted lines). Henceforth, it is interesting to notice how the transmission process through ADF structures, either can be explained in the framework of a Fano type resonance, but also in terms of studying the modal velocity symmetry.

5.5 Conclusion and future work

Analytically and numerically we have presented a new acoustical device for efficient sound blockage. The ADF structure, which can be fabricated out of two holey steel or brass plates separated with a gap, can be tuned to give rise to a wide band of low sound transmission, due to a resonant negative bulk modulus. We have calculated how to determine the spectral location of the resonance dependent on the hole size, and also shown how to tune the size of the bandgap for different gap separations, h_g . Moreover, in this context, by means of analytical formulas we have predicted that externally irradiated sound can excite gap modes that are responsible for the appearance of negative $\text{Re}(1/\kappa)$. Different from Bragg-scattering based crystals, the ADF metamaterial is a very thin composite that does not rely on periodic material modulation. Therefore we expect that the use for applications will be very important, in the design of novel acoustical devices for sound sealing and attenuation in automotive and environmental developments.

It is well known that spoof SPPs, induced by holes pierced into a PEC, will support the formation of bound modes, that are controlled by the cutoff inside those holes [28]. Remarkably, this cutoff determines the electrical resonance of the double-fishnet structure for EM waves [137]. Due to the absence of a cutoff frequency in holey

acoustic structures as of no polarization in air-borne sound, we showed that the acoustic analogy of the double-fishnet structure is a SNG metamaterial suitable for the resonant blockage of sound. In other words, only the acoustic analogy of the magnetic resonance prevails, when modes are excited in the intermediate gap, separating the adjacent hole arrays. We foresee experiments to come soon because both the device itself, and the measurement procedure will not differ much from what have been employed to observe EAT [90, 97]. However, an important advancement of the current ADF structure would be the introduction of another resonant mechanism (coated sphere, membrane etc. [65]) for tuning the effective mass density to negative values. Effectively combining those two resonances could give rise to a band of negative refraction, with the possibility of perfect lensing, i.e., amplifying evanescent waves.

Chapter 6

Conclusion

English

This thesis has been concerned with a theoretical study on acoustic wave phenomena in relation with structured metallic systems for enhanced transmission of sound, shielding and imaging. The main focus has been on the development of a modal expansion technique and the consequential analytical problem treatment, although numerical results have also been presented and discussed. The thesis consists of four parts, extraordinary transmission, guiding of sound along a wire, metamaterial based imaging and sound blockage by means of an acoustic double-fishnet structure. In the following an outline of the results obtained from the different parts will be presented.

6.1 Summary

In the first part, study on the extraordinary acoustical transmission, we developed a general model based on the mode matching technique for perforated systems. This model is based on assuming that no wave energy is penetrating into the plates in which apertures are carved, and that all fluids are inviscid, hence dissipative losses

are disregarded. Firstly, we have taken finite structures under investigation and calculated how sound is able to penetrate single isolated apertures such as slits and holes. In both cases we find that the dominant geometrical parameter, which controls the spectral locations of the resonances and consequently the locations of high transmittance efficiency, is the thickness of the plate. However, the main difference between those two configurations is the growing transmittance as a function of the wavelength: for slits it is a linear dependence whereas holes contain a quadratic dependence. Within the same formalism a modification has been introduced to account for periodic slit and hole arrays. Apart from the resonance governed by the structure thickness (Fabry-Perot) giving rise to full transmittance, a new resonance appears that stems from the excitation of an acoustic guided wave running along the surface of the plate. This acoustic surface wave hybridizes strongly with the Fabry-Perot resonances in single apertures, and is tunable with the height and width of the perforations. We found that the comparison of 1D structures for sound and light (p-polarized) is very similar, but that 2D structures differ significantly, which originates in the absence of a cutoff for the fundamental cavity mode in sonic waveguides.

In the second part we studied the existence of acoustic bound modes by a corrugated sound-hard wire. The advantage of the modal expansion technique used in the previous part is shown by its flexibility also to handle cylindrical structures, such as the present wire. In that respect we have shown that within the long wavelength limit, the surface states supported by the wire approach the same modes from a groove grating, which also holds for spoof surface plasmons along a corrugated perfect conducting wire. The model created has also been used to study the geometrical influence on the bands, in which we found that the pressure field confinement grows with increasing ring depths. With FEM analysis, numerical calculations have been conducted to study finite structures. The advantage of the slow modes (flat bands) has led to the design of a conical corrugated structure, by which subwavelength focusing of sound is achieved.

In the third part, acoustic deep subwavelength imaging, we developed an effective medium approach by employing a multiple scattering formalism in the long wavelength limit. We show that within the perfect rigid body assumption and at some resonant frequencies, holey metal blocks make a robust imaging device. It is presented that the transmission coefficient for sound through those holey metamaterials is unity for all parallel momenta. Unlike perfect lensing which amplifies evanescent waves, a standing wave of constant phase within the metamaterial is built up that can be excited from various angles of incident sound. In this respect, we show how those DC (direct current) modes can transfer a complex 3D object with all its propagating and evanescent (near-field) field components to an image plane, which makes sonic scanning feasible beyond the diffraction limit. Our theoretical results are in good agreement with experiments performed.

In the fourth part, blockage by means of an acoustic double-fishnet structure, we have extended the single plate model to two adjacent holey perfect rigid plates. The acoustic coupling between holes in the gap region is measured by simple trigonometric functions summed over diffraction orders, hence not adding additional demands in terms of computation. We have shown that apart from the Fabry-Perot and acoustic surface modes supported by a single plate, gap modes resonances emerge in the intermediate plate separation. By studying the symmetry of all resonances supported by the structure, we obtained analytical insight into the problem, such that only odd Fabry-Perot resonances couple to those gap modes, whereas the even Fabry-Perot modes almost remain unaltered as a function of the gap width. Moreover, we have found out that, due to the lack of cutoff for sound propagating inside holes, the acoustic structure exhibits no negative refraction. Instead, our model has enabled us to demonstrate that the current acoustic double-fishnet structure can operate as a tunable device presenting a broadband, all angle blockage of sound due to a negative effective bulk modulus, containing little dispersion with parallel momentum.

Español

Esta disertación doctoral se ha enfocado sobre fenómenos acústicos ondulatorios, en relación con sistemas metálicos estructurados y sus propiedades de intensificación de la transmisión de sonido, opacidad y proyección de imágenes. El principal enfoque es el desarrollo de una técnica de expansión modal y su consecuente tratamiento analítico con resultados numéricos que han sido presentados y discutidos. Esta tesis consiste de 4 partes: transmisión extraordinaria, guiado de ondas a lo largo de un alambre rígido, metamateriales para obtención de imágenes y bloqueo de sonido por medio de una estructura acústica tipo *double-fishnet*. A continuación será presentado un resumen de los resultados obtenidos.

En la primera parte, estudio sobre la transmisión extraordinaria de sonido, desarrollamos un modelo general basado en la técnica de expansión modal para sistemas perforados. Este modelo se desarrolla bajo el supuesto de que no hay penetración de energía de las ondas en la lámina sobre la cual se perforan los agujeros y que los fluidos son viscosos, por lo tanto las pérdidas por disipación no son consideradas dentro del modelo. Primero hemos tomado estructuras que están bajo investigación y se ha calculado como el sonido es capaz de penetrar por aperturas únicas aislada tales como rendijas y agujeros. En ambos casos encontramos que el parámetro geométrico dominante, el cual controla la localización espectral de las resonancias y consecuentemente la localización de la alta eficiencia de transmisión, es el grosor de la lámina. Sin embargo, la diferencia entre estas dos configuraciones es el incremento de la transmitancia como función de la longitud de onda: para la rendija es una dependencia lineal mientras que para el agujero presenta una dependencia cuadrática. En el mismo formalismo se ha introducido modificaciones para tomar en cuenta rendijas periódicas y *array* de agujeros. Una parte de la resonancia (tipo Fabry-Perot) es gobernada por el grosor de la estructura dando una transmisión completa, y surge una nueva resonancia derivada de la excitación de una onda acústica guiada corriendo a lo largo de la superficie de la lámina. Esta onda superficial acústica se hibridiza

fuertemente con la resonancia Fabry-Perot en una única apertura, y está relacionada con la altura y el ancho de la perforación. Nosotros encontramos que la comparación de las estructuras unidimensionales 1D para sonido y luz (con polarización P) son muy similares, pero las estructuras bidimensionales 2D difieren significativamente, lo cual tiene su origen en la ausencia de *cutoff* para el modo de cavidad fundamental en la guía de onda.

En la segunda parte estudiamos la existencia de modos acústicos ligados para una guía de onda sonora consistente en un alambre rígido. La ventaja de la técnica de expansión modal usada en la parte anterior es mostrada aquí dada su capacidad para describir estructuras cilíndricas tales como el alambre usado en esta disertación. Con respecto a este, hemos demostrado que en el límite de longitud de onda grande, los estados superficiales soportados por el alambre se aproximan a los mismos modos de una rejilla de ranuras, la cual también soporta plasmones superficiales inducidos a lo largo de un alambre conductor perfecto corrugado. El modelo creado también ha sido usado para estudiar la influencia geométrica sobre las bandas, en la cual hemos encontrado que el campo de presión confinado crece con el incremento de la profundidad de los anillos. Con un análisis FEM, se han realizado cálculos numéricos para estudiar estructuras finitas. La ventaja de los modos suaves (bandas planas) ha llevado al diseño de una estructura corrugada cónica, por medio de la cual se consigue un enfoque de ondas acústicas sub-longitudes de onda.

En la tercera parte, en la proyección de imágenes acústicas en régimen sub-longitud de onda, fue desarrollado un medio efectivo aproximado empleando un formalismo de *scattering* múltiple en el límite de longitud de onda. Nosotros mostramos que asumiendo un cuerpo rígido perfecto y en algunas frecuencias resonantes, bloques de metales agujereados constituyen un robusto dispositivo de proyección de imágenes. Se observa que el coeficiente de transmisión de sonido a través de estos metamateriales agujereados es unitario para todos los momentos paralelos. A diferencia de la lente perfecta la cual amplifica ondas evanescentes, una onda estacionaria con

fase constante en un metamaterial es construida tal que puede ser excitada desde varios ángulos de incidencia del sonido. Al respecto, mostramos como estos modos DC (corriente directa) pueden transferir objetos complejos tridimensionales 3D con todas sus componentes propagantes y evanescentes de campo (campo cercano) para una imagen plana, la cual hace posible exploración sónica más allá del límite de difracción. Nuestros resultados teóricos están en muy buen acuerdo con diseños experimentales.

En la cuarta parte, usando una estructura tipo *double-fishnet*, nosotros extendimos el modelo para una lámina a dos láminas adyacentes agujereadas y perfectamente rígidas. El acople acústico entre agujeros en la región del *gap* es medido por funciones trigonométricas simples sumadas sobre los órdenes de difracción, por lo tanto no adiciona complicaciones en términos de computo. Nosotros mostramos que aparte de modos tipo Fabry-Perot y modos acústicos superficiales soportados por una simple lamina, modos *gap* resonantes emergen del lugar intermedio de separación de las láminas. Estudiando la simetría de todas las resonancias soportadas por la estructura, obtuvimos conocimientos analíticos acerca del problema, tales como que solo resonancias tipo Fabry-Perot pares se acoplan a estos modos *gap*, mientras los modos tipo Fabry-Perot impares prácticamente se mantienen inalterados como una función de el ancho del *gap*. Más aun, nosotros encontramos que debido a la ausencia de *cutoff* para sonido propagante dentro del agujero, la estructura acústica no exhibe refracción negativa. En lugar de ello, nuestro modelo nos ha permitido demostrar que la corriente acústica de la estructura *double-fishnet* puede operar como un dispositivo ajustable presentando un ensanchamiento de banda, todos los ángulos bloqueados debido a módulos negativos de compresibilidad tienen pequeña dispersión con momento paralelo.

6.2 List of Publications

- J. Christensen, A. I. Fernandez-Dominguez, F. de Leon-Perez, L. Martin-Moreno, and F. J. Garcia-Vidal, *Collimation of sound assisted by acoustic surface waves*, Nature Physics **3**, 851 (2007).
- J. Christensen, L. Martin-Moreno, and F. J. Garcia-Vidal, *Theory of resonant acoustic transmission through subwavelength apertures*, Physical Review Letters **101**, 014301 (2008).
- J. Christensen, P. A. Huidobro, L. Martin-Moreno, and F. J. Garcia-Vidal, *Confining and slowing airborne sound with a corrugated metawire*, Applied Physics Letters, **93**, 083502 (2008).
- J. Christensen, L. Martin-Moreno, and F. J. Garcia-Vidal, *Enhanced acoustical transmission and beaming effect through a single aperture*, accepted for publication in Physical Review B 2010.
- J. Christensen, L. Martin-Moreno, and F. J. Garcia-Vidal, *Collimation of horizontally polarized shear waves by means of ridge grating supported Love modes*, accepted for publication in Applied Physics Letters 2010.
- J. Christensen, L. Martin-Moreno, and F. J. Garcia-Vidal, *Broadband all-angle blockage of sound by an acoustic double-fishnet metamaterial*, submitted 2010.
- J. Zhu, J. Christensen, J. Jung, L. Martin-Moreno, X. Yin, L. Fok, X. Zhang and F. J. Garcia-Vidal, *A holey structured metamaterial for acoustic deep sub-wavelength imaging*, submitted 2010.

Appendix A

In this appendix, extensive derivations devoted to Chapter 2 of the thesis are given. These derivations are the overlapping integrals between Bloch waves and rectangular hole and slit waveguide modes, such as the expansion coefficients and approximations for the Greens functions.

A.1 Overlap functions for a slit array

For the slit array, the overlap function is defined in the following way:

$$S_{\gamma m} = \langle k_x^\gamma | q_x^m \rangle = \int \langle k_x^\gamma | x \rangle \langle x | q_x^m \rangle dx \quad (\text{A.1})$$

where we shall introduce three solutions, related to the presence of all waveguide modes $m \neq 0$, the fundamental mode approximation $m = 0$ and the one where diffraction safely can be neglected together with the fundamental waveguide mode $m = \gamma = 0$:

For $m \neq 0$:

$$\begin{aligned} S_{\gamma m} &= \sqrt{\frac{2 - \delta_{0m}}{a\Lambda}} \int_{-\frac{a}{2}}^{\frac{a}{2}} \cos \frac{m\pi}{a} \left(x + \frac{a}{2}\right) e^{-ik_x^\gamma x} dx = \\ &= \sqrt{\frac{2 - \delta_{0m}}{a\Lambda}} \frac{ik_x^\gamma}{(k_x^\gamma)^2 - \left(\frac{m\pi}{a}\right)^2} \left((-1)^m e^{-ik_x^\gamma \frac{a}{2}} - e^{ik_x^\gamma \frac{a}{2}} \right). \end{aligned} \quad (\text{A.2})$$

For $m = 0$:

$$S_{\gamma 0} = \sqrt{\frac{a}{\Lambda}} \operatorname{sinc} \frac{k_x^\gamma a}{2}. \quad (\text{A.3})$$

For $m = \gamma = 0$:

$$S_{00} = \sqrt{\frac{a}{\Lambda}}. \quad (\text{A.4})$$

A.2 Overlap functions for a hole array

In here the overlap function for hole arrays are derived, which straightforwardly can be written in terms of the slit overlaps from section A.1:

$$S_{\beta\alpha} = \langle \mathbf{k}_{\parallel}^{\beta} | \mathbf{q}_{\parallel}^{\alpha} \rangle = \int \langle \mathbf{k}_{\parallel}^{\beta} | \mathbf{r}_{\parallel} \rangle \langle \mathbf{r}_{\parallel} | \mathbf{q}_{\parallel}^{\alpha} \rangle d\mathbf{r}_{\parallel} \quad (\text{A.5})$$

where $(\mathbf{k}_{\parallel}^{\beta})^2 = (\mathbf{k}_{\parallel}^{\gamma n})^2 = (k_x^n)^2 + (k_y^\gamma)^2$ and $(\mathbf{q}_{\parallel}^{\alpha})^2 = (\mathbf{q}_{\parallel}^{ml})^2 = (q_x^m)^2 + (q_y^l)^2$. Hence, when applying Eq. (A.2) the two dimensional overlap reads:

$$S_{\beta\alpha} = S_{\gamma m} S_{nl}. \quad (\text{A.6})$$

E.g. for the fundamental mode approximation Eq. (A.6) is restated according to the respective definitions in section A.1.

A.3 Overlap and Greens functions for isolated apertures containing indentations

For the single slit surrounded by corrugations, the Greens function is similar to Eq. (2.30) from section 2.4, though with the difference containing a phase with respect

to the groove locations $x_\sigma = \sigma\Lambda$:

$$G_{slit} \rightarrow G_{x,x'} = \langle x|\tilde{G}|x'\rangle = \frac{i\pi}{\lambda} \int_{x_\sigma-a/2}^{x_\sigma+a/2} \int_{x_{\sigma'}-a/2}^{x_{\sigma'}+a/2} H_0^{(1)}(k_0|x-x'|) dx dx'. \quad (\text{A.7})$$

The overlap function in the illumination term I_σ^0 , which is not a function of diffracted waves, is nothing but:

$$S_{00} = \sqrt{\frac{a}{\Lambda}} \text{sinc} \frac{k_x^0 a}{2} e^{-ik_x^0 x_\sigma}. \quad (\text{A.8})$$

A.4 Expansion coefficients

The expansion coefficients A_m, B_m such as the modal fields v_m, v'_m can be stated into the following expressions:

$$A_m = -\frac{v'_m + v_m e^{iq_z^m h}}{e^{iq_z^m h} - e^{-iq_z^m h}} \quad (\text{A.9})$$

$$B_m = -\frac{v'_m + v_m e^{-iq_z^m h}}{e^{iq_z^m h} - e^{-iq_z^m h}} \quad (\text{A.10})$$

$$v_0 = \frac{I^0(G - \epsilon)}{(G - \epsilon)^2 - (G^V)^2} \quad (\text{A.11})$$

$$v'_0 = \frac{I^0 G^V}{(G - \epsilon)^2 - (G^V)^2}. \quad (\text{A.12})$$

Appendix B

In this appendix we demonstrate the full derivation of the resonant unity-transmission, for a hole array structure, acting as a imaging device.

B.1 Transmission coefficient for a holey metamaterial

We begin to express the transmission coefficient for a hole array, with the use of Eq. (2.16) from section 2.3 and rewrite it into a 2D problem:

$$T_\beta = (A_0 e^{iq_z^0 h} - B_0 e^{-iq_z^0 h}) S_{\beta 0}^*. \quad (\text{B.1})$$

Eq. (B.1) can be simplified with the definition Eq. (2.18), the modal output velocity:

$$T_\beta = -v' S_{\beta 0}^*, \quad (\text{B.2})$$

and entirely be generalized with the expressions, Eq. (A.12), contained in the system of equations:

$$T_\beta = -\frac{I^0 G^V}{(G - \epsilon)^2 - (G^V)^2} S_{\beta 0}^*. \quad (\text{B.3})$$

Substituting the corresponding functions yields

$$T_\beta = \frac{k_0}{k_z^0} \frac{4}{e^{iq_z^0 h} - e^{-iq_z^0 h}} \frac{S_{00} S_{\beta 0}^*}{(G - \epsilon)^2 - (G^V)^2}, \quad (\text{B.4})$$

and after further straight forward algebra:

$$T_\beta = \frac{k_0}{k_z^0} \frac{4}{2i \sin q_z^0 h} \frac{S_{00} S_{\beta 0}^*}{G^2 + \frac{\cos^2 q_z^0 h - 1}{\sin^2 q_z^0 h} - 2G \frac{\cos q_z^0 h}{\sin q_z^0 h}}, \quad (\text{B.5})$$

and

$$T_\beta = \frac{4 \frac{k_0}{k_z^0} S_{00} S_{\beta 0}^*}{2iG^2 \sin q_z^0 h - 2i \sin q_z^0 h - 4iG \cos q_z^0 h} \quad (\text{B.6})$$

such as:

$$T_\beta = \frac{4 \frac{k_0}{k_z^0} S_{00} S_{\beta 0}^*}{G^2 (e^{iq_z^0 h} - e^{-iq_z^0 h}) - (e^{iq_z^0 h} - e^{-iq_z^0 h}) - 2iG (e^{iq_z^0 h} + e^{-iq_z^0 h})}, \quad (\text{B.7})$$

$$T_\beta = \frac{4 \frac{k_0}{k_z^0} S_{00} S_{\beta 0}^*}{e^{iq_z^0 h} (G - i)^2 - e^{-iq_z^0 h} (G + i)^2}. \quad (\text{B.8})$$

If we impose $S_{\beta 0} S_{\beta 0}^* = |S_{\beta 0}|^2$ into Eq. (B.8) it further simplifies into:

$$T_\beta = \frac{4 \frac{k_0}{k_z^0} |S_{\beta 0}|^2 e^{iq_z^0 h}}{e^{2iq_z^0 h} (i \frac{k_0}{k_z^0} |S_{\beta 0}|^2 - i)^2 - (i \frac{k_0}{k_z^0} |S_{\beta 0}|^2 + i)^2}, \quad (\text{B.9})$$

and if we now neglect diffraction for very subwavelength geometries given as $a = a_x = a_y$ such as $\Lambda = \Lambda_x = \Lambda_y$:

$$T_0 = \frac{4 \frac{k_0}{k_z^0} \left| \frac{a}{\Lambda} \right|^2 e^{iq_z^0 h}}{\left(\frac{k_0}{k_z^0} \left| \frac{a}{\Lambda} \right|^2 + 1 \right)^2 - e^{2iq_z^0 h} \left(\frac{k_0}{k_z^0} \left| \frac{a}{\Lambda} \right|^2 - 1 \right)^2}. \quad (\text{B.10})$$

Eq. (B.10) resembles a very general expression for the transmission coefficient due to a multiple scattering event. If a Fabry Perot resonance of order m is introduced, $q_z^0 h = m\pi$, we have:

$$T_0 = \frac{4 \frac{k_0}{k_z^0} \frac{a^2}{\Lambda^2} (-1)^m}{\left(\frac{k_0}{k_z^0} \frac{a^2}{\Lambda^2} + 1 \right)^2 - \left(\frac{k_0}{k_z^0} \frac{a^2}{\Lambda^2} - 1 \right)^2}, \quad (\text{B.11})$$

which is nothing but:

$$\boxed{T_0 = (-1)^m} \quad (\text{B.12})$$

Bibliography

- [1] Lord Rayleigh. *Philos. Trans.*, 161:77, 1871.
- [2] Suxia Yang, J. H. Page, Zhengyou Liu, M. L. Cowan, C. T. Chan, and Ping Sheng. *Phys. Rev. Lett.*, 93:024301, 2004.
- [3] Zhengyou Liu, Xixiang Zhang, Yiwei Mao, Y. Y. Zhu, Zhiyu Yang, C. T. Chan, and Ping Sheng. *Science*, 289:1734, 2000.
- [4] J. E. Kennedy. *Nat. Rev. Cancer*, 5:321, 2005.
- [5] M. Fink. *Sci. Am.*, 281:91, 1999.
- [6] M. Fink, D. Cassereau, A. Derode, C. Prad, P. Roux, M. Tanter, J. Thomas, and F. Wu. *Rep. Prog. Phys.*, 63:1933, 2000.
- [7] W. L. Barnes, A. Dereux, and T. M. Ebbesen. *Nature*, 424:824, 2003.
- [8] C. Genet and T. W. Ebbesen. *Nature*, 445:39, 2007.
- [9] T. M. Ebbesen, C. Genet, and S. I. Bozhevolnyi. *Physics Today*, 61:44, 2008.
- [10] A. Sommerfeld. *Ann. Phys. und Chemie*, 303:233, 1899.
- [11] J. Zenneck. *Ann. Phys.*, 23:846, 1907.
- [12] U. Leonhardt. *Nature Photonics*, 1:207, 2007.
- [13] R. W. Wood. *Proc. Phys. Soc. London*, 18:269, 1902.

- [14] Lord Rayleigh. *Proc. Roy. Soc. London*, A79:399, 1907.
- [15] U. Fano. *J. Opt. Soc. Am.*, 31:213, 1941.
- [16] R. H. Ritchie. *Phys. Rev.*, 106:874, 1957.
- [17] A. Otto. *Z. Phys*, 216:398, 1968.
- [18] E. Kretschmann and H. Raether. *Z. Naturforschung*, 23A:2135, 1968.
- [19] T. W. Ebbesen, H. J. Lezec, H. F. Ghaemi, T. Thio, and P. A. Wolff. *Nature*, 391:667, 1998.
- [20] H. Bethe. *Phys. Rev.*, 66:163, 1944.
- [21] C. J. Bouwkamp. *Rep. Prog. Phys.*, 17:35, 1954.
- [22] F. J. Garcia-Vidal, L. Martin-Moreno, T. W. Ebbesen, and L. Kuipers. Light passing through subwavelength structures. *Rev. Mod. Phys.*, 82:729, 2010.
- [23] F. Yang and J. R. Sambles. *Phys. Rev. Lett.*, 89:063901, 2002.
- [24] D. Qu, D. Grischkowsky, and W. Zhang. *Opt. Lett.*, 29:896, 2004.
- [25] Y. H. Ye and J. Y. Zhang. *Appl. Phys. Lett.*, 84:2977, 2004.
- [26] H. Cao and A. Nahata. *Opt. Express*, 12:1004, 2004.
- [27] M. Beruete, M. Sorolla, I. Campillo, J. S. Dolado, L. Martin-Moreno, J. Bravo-Abad, and F. J. Garcia-Vidal. *Opt. Lett.*, 29:2500, 2004.
- [28] J. B. Pendry, L. Martín-Moreno, and F. J. García-Vidal. *Science*, 305:847, 2004.
- [29] A. P. Hibbins, B. R. Evans, and J. R. Sambles. *Science*, 308:670, 2005.
- [30] S. A. Maier, S. R. Andrews, L. Martín-Moreno, and F. J. García-Vidal. *Phys. Rev. Lett.*, 97:176805, 2006.

- [31] J.-C. Weeber, J. R. Krenn, A. Dereux, B. Lamprecht, Y. Lacroute, and J. P. Goudonnet. *Phys. Rev. B*, 64:045411, 2001.
- [32] D. Sarid. *Phys. Rev. Lett.*, 47:1927, 1981.
- [33] J. R. Krenn and J. C. Weeber. *Phylos. Trans. R. Soc. London Ser. A*, 362:739, 2004.
- [34] S. A. Maier, P. G. Kik, H. A. Atwater, S. Meltzer, E. Harel, B. E. Koel, and A. A. G. Requicha. *Nature Materials*, 2:229, 2003.
- [35] S. I. Bozhevolnyi, V. S. Volkov, E. Devaux, J.-Y. Laluet, and T. W. Ebbesen. *Nature*, 440:508, 2006.
- [36] E. Moreno, S. G. Rodrigo, S. I. Bozhevolnyi, L. Martín-Moreno, and F. J. García-Vidal. *Phys. Rev. Lett.*, 100:023901, 2008.
- [37] E. Ozbay. *Science*, 311:189, 2006.
- [38] H. Lamb. *Proc. London Math. Soc.*, 1:473, 1904.
- [39] D. V. Sivukhin. *Opt. Spektrosk.*, 3:308, 1957.
- [40] V. G. Veselago. *Sov. Phys. Usp.*, 10:509, 1967.
- [41] W. E. Kock. *Proc. IRE*, 34:828, 1946.
- [42] W. E. Kock. *Proc. IRE*, 27:58, 1948.
- [43] S. B. Cohn. *J. Appl. Phys.*, 20:257, 1949.
- [44] S. B. Cohn. *J. Appl. Phys.*, 24:7, 1953.
- [45] W. Rotman. *IRE Trans. Antennas Propagat.*, 10:82, 1962.
- [46] S. Schelkunoff and H. Friss. *Antenas: Theory and practice*. John Wiley Sons, New York, 1952.

- [47] H. J. Schneider and P. Dullenkopf. *Rev. Sci. Instrum.*, 48:68, 1977.
- [48] W. H. Hardy and L. A. Whitehead. *Rev. Sci. Instrum.*, 52:213, 1981.
- [49] J. B. Pendry, A. J. Holden, W. J. Stewart, and I. Youngs. *Phys. Rev. Lett.*, 76:4773, 1996.
- [50] J. B. Pendry, A. J. Holden, D. J. Robbins, and W. J. Stewart. *IEEE Microwav. Theory and Tech.*, 47:2075, 1999.
- [51] D. R. Smith, W. J. Padilla, D. C. Vier, S. C. Nemat-Nasser, and S. Schultz. *Phys. Rev. Lett.*, 84:4184, 2000.
- [52] R. A. Schelby, D. R. Smith, and S. Schultz. *Science*, 292:77, 2001.
- [53] J. B. Pendry. *Phys. Rev. Lett.*, 85:3966, 2000.
- [54] T. J. Yen, W. J. Padilla, N. Fang, D. C. Vier, D. R. Smith, J. B. Pendry, D. N. Basov, and X. Zhang. *Science*, 303:1494, 2004.
- [55] G. Dolling, C. Enkrich, M. Wegener, C. M. Soukoulis, and S. Linden. *Science*, 312:892, 2006.
- [56] J. Yao, Z. Liu, Y. Liu, Y. Wang, C. Sun, G. Bartal, A. Stacy, and X. Zhang. *Science*, 321:930, 2008.
- [57] J. Christensen, A. I. Fernández-Domínguez, F. de Leon-Pérez, L. Martín-Moreno, and F. J. García-Vidal. *Nature Physics*, 3:851, 2007.
- [58] X. Zhang. *Phys. Rev. B*, 71:241102, 2005.
- [59] L. Zhou and G. A. Kriegsmann. *J. Acoust. Soc. Am*, 121:3288, 2007.
- [60] J. Li and C. T. Chan. *Phys. Rev. E*, 70:055602(R), 2004.
- [61] Y. Ding, Z. Liu, C. Qiu, and J. Shi. *Phys. Rev. Lett.*, 99:093904, 2007.

- [62] N. Fang, D. Xi, J. Xu, M. Ambati, W. Srituravanich, and X. Zhang. *Nat. Mat.*, 5:452, 2006.
- [63] G. W. Stewart. *Phys. Rev.*, 20:528, 1922.
- [64] D. Zhao, Z. Liu, C. Qiu, Z. He, F. Cai, and M. Ke. *Phys. Rev. B*, 76:144301, 2007.
- [65] L. Fok, M. Ambati, and X. Zhang. *MRS Bulletin*, 33:931, 2008.
- [66] F. Liu, S. Peng, H. Jia, M. Ke, and Z. Liu. *Appl. Phys. Lett.*, 94:023505, 2009.
- [67] Lord Rayleigh. *Proc. London Math. Soc.*, 1:4, 1855.
- [68] R. M. White and F. W. Voltmer. *Appl. Phys. Lett.*, 7:314, 1965.
- [69] J. M. Shilton, V. I. Talyanskii, M. Pepper, D. A. Ritchie, J. E. F. Frost, C. J. B. Ford, C. G. Smith, and G. A. C. Jones. *J. of Phys.: Cond. Matt.*, 8:953, 1996.
- [70] L. D. Landau and E. M. Lifshitz. *Fluid Mechanics, Third Edition: Volume 6*. Butterworth-Heinemann; 3 edition, Oxford, 2000.
- [71] M. Willatzen. *Journ. of Sound and Vibr.*, 247:719, 2001.
- [72] L. D. Landau and E. M. Lifshitz. *Theory of Elasticity, Third Edition: Volume 7*. Butterworth-Heinemann; 3 edition, Oxford, 2000.
- [73] J. Christensen, L. Martín-Moreno, and F. J. García-Vidal. *Phys. Rev. Lett.*, 101:014301, 2008.
- [74] L. Martin-Moreno and F. J. Garcia-Vidal. *J. Phys: Condens. Matt.*, 20:304215, 2008.
- [75] L. E. Kinsler, A. R. Frey, A. B. Coppens, and J. V. Sanders. *Fundamentals of Acoustics, Fourth Edition*. Wiley, Danvers, 1982.

- [76] Cremer and M. Heckl. *Körperschall, 2nd edition*. Springer Verlag, Berlin/Heidelberg, 1996.
- [77] J. D. Jackson. *Classical electrodynamics*. John Wiley & Sons, New York, 3rd edition, 1999.
- [78] J. A. Porto, F. J. García-Vidal, and J. B. Pendry. *Phys. Rev. Lett.*, 83:2845, 1999.
- [79] H. E. Went, A. P. Hibbins, J. R. Sambles, C. R. Lawrence, and A. P. Crick. *Appl. Phys. Lett.*, 77:2789, 2000.
- [80] Y. Takakura. *Phys. Rev. Lett.*, 86:5601, 2001.
- [81] J. Bravo-Abad, L. Martín-Moreno, and F. J. García-Vidal. *Phys. Rev. E*, 69:26601, 2004.
- [82] J. M. A. Smits and C. W. Kosten. *Acustica*, 1:114, 1951.
- [83] M. C. Gomperts. *Acustica*, 14:1, 1964.
- [84] M. C. Gomperts and T. Kihlman. *Acustica*, 18:144, 1967.
- [85] C. L. Mofrey. *J. Sound Vib.*, 9:357, 1969.
- [86] D. J. Oldham and X. Zhao. *J. Sound Vib.*, 161:119, 1993.
- [87] A. Degiron, H. J. Lezec, N. Yamamoto, and T. W. Ebbesen. *Opt. Commun.*, 239:61, 2004.
- [88] F. J. García-Vidal, E. Moreno, J. A. Porto, and L. Martín-Moreno. *Phys. Rev. Lett.*, 95:103901, 2005.
- [89] F. J. García de Abajo. *Opt. Express*, 10:1475, 2002.
- [90] B. Hou, J. Mei, M. Ke, W. Wen, Z. Liu, J. Shi, and P. Sheng. *Phys. Rev. B*, 76:054303, 2007.

- [91] G.P. Wilson and W.W. Soroka. *J. Acoust. Soc. Am*, 37:286, 1965.
- [92] G.P. Wilson and W.W. Soroka. *J. Acoust. Soc. Am*, 37:286, 1965.
- [93] K. A. Mulholland and H. D. Parbrook. *J. Sound Vib.*, 5:499, 1967.
- [94] M.-H. Lu, X.-K. Liu, L. Feng, J. Li, C.-P. Huang, Y.-F. Chen, Y.-Y. Zhu, S.-N. Zhu, and N.-B. Ming. *Phys. Rev. Lett.*, 99:174301, 2007.
- [95] L. Kelders, J.F. Allard, and W. Lauriks. *J. Acoust. Soc. Am*, 103:2730, 1998.
- [96] L. Kelders, W. Lauriks, and J.F. Allard. *J. Acoust. Soc. Am*, 104:2882, 1998.
- [97] H. Estrada, P. Candelas, A. Uris, F. Belmar, F. J. G. de Abajo, and F. Meseguer. *Phys. Rev. Lett.*, 101:084302, 2008.
- [98] H. Estrada, P. Candelas, A. Uris, F. Belmar, F. J. G. de Abajo, and F. Meseguer. *Phys. Rev. Lett.*, 102:144301, 2009.
- [99] H. J. Lezec, A. Degiron, E. Deveux, R. A. Linke, L. Martín-Moreno, F. J. García-Vidal, and T. W. Ebbesen. *Science*, 297:820, 2002.
- [100] L. Martín-Moreno, F. J. García-Vidal, H. J. Lezec, A. Degiron, and T. W. Ebbesen. *Phys. Rev. Lett.*, 90:167401, 2003.
- [101] F. J. García-Vidal, H. J. Lezec, T. W. Ebbesen, and L. Martín-Moreno. *Phys. Rev. Lett.*, 90:213901, 2003.
- [102] F. J. Garcia-Vidal, L. Martin-Moreno, H. J. Lezec, and T. W. Ebbesen. *Appl. Phys. Lett.*, 83:4500, 2003.
- [103] G. Gay, O. Alloschery, B. Viars De Lesegno, C. O'Dwyer, J. Weiner, and H. J. Lezec. *Nature Photonics*, 2:262, 2006.
- [104] L. Martín-Moreno, F. J. García-Vidal, H. J. Lezec, K. M. Pellerin, T. Thio, J. B. Pendry, and T. W. Ebbesen. *Phys. Rev. Lett.*, 86:1114, 2001.

- [105] J. Mei, B. Hou, M. Ke, W. Wen, Z. Liu, J. Shi, and P. Sheng. *Appl. Phys. Lett.*, 92:124106, 2008.
- [106] Z. F. Liu and G. J. Jin. *J. Phys: Condens. Matt.*, 21:445401, 2009.
- [107] R. N. Thurston. *J. Acoust. Soc. Am*, 64:1, 1978.
- [108] J. W. Strutt and Baron Rayleigh. *The theory of sound, Vol. I*. Macmillan and Co, London, 1877.
- [109] J. W. Strutt and Baron Rayleigh. *The theory of sound, Vol. II*. Macmillan and Co, London, 1878.
- [110] Y. V. Gulyaev and V. P. Plesskii. *Sov. Tech. Phys. Lett.*, 3:87, 1977.
- [111] H. Levine and J. Schwinger. *Phys. Rev.*, 73:383, 1948.
- [112] M. K. Miller. *J. Acoust. Soc. Am*, 36:2143, 1964.
- [113] C. W. Horton and J. D. Jones. *J. Acoust. Soc. Am*, 52:1456, 1972.
- [114] L. Lundqvist. *J. Acoust. Soc. Am*, 80:1423, 1986.
- [115] L. Lundqvist and A. Boström. *J. Sound Vib.*, 112:111, 1987.
- [116] O. R. Asfar and M. A. Hawwa. *J. Acoust. Soc. Am*, 93:2468, 1993.
- [117] H. Kamath, M. Willatzen, and R. V. N. Melnik. *Ultrasonics*, 44:64, 2006.
- [118] J. Li, L. Fok, X. Yin, G. Bartal, and X. Zhang. *Nat. Mat*, 8:931, 2009.
- [119] Xiangdong Zhang and Z. Liu. *Appl. Phys. Lett.*, 85:341, 2004.
- [120] A. Sukhovich, B. Merheb, K. Muralidharan, J. O. Vasseur, Y. Pennec, P. A. Deymier, and J. H. Page. *Phys. Rev. Lett.*, 102:4154301, 2009.
- [121] N. Fang, H. Lee, C. Sung, and X. Zhang. *Science*, 308:534, 2005.

- [122] P. A. Belov and Y. Hao. *Phys. Rev. B.*, 73:113110, 2006.
- [123] B. Wood, J. B. Pendry, and D. P. Tsai. *Phys. Rev. B.*, 74:115116, 2006.
- [124] F. Miyamaru and M. Hangyo. *Appl. Phys. Lett.*, 84:2742, 2004.
- [125] P. A. Belov, Y. Hao, and S. Sudhakaran. *Phys. Rev. B.*, 73:033108, 2006.
- [126] G. Shvets, S. Trendafilov, J. B. Pendry, and A. Sarychev. *Phys. Rev. Lett.*, 99:053903, 2007.
- [127] S. Kawata, A. Ono, and P. Verma. *Nature Photonics*, 2:438, 2008.
- [128] J. Jung, F. J. Garcia-Vidal, L. Martin-Moreno, and J. B. Pendry. *Phys. Rev. B.*, 79:153407, 2009.
- [129] M. Ambati, N. Fang, C. Sun, and X. Zhang. *Phys. Rev. B*, 75:195447, 2007.
- [130] X. Ao and C. T. Chan. *Phys. Rev. E*, 77:025601(R), 2008.
- [131] T. Koschny, M. Kafesaki, E. N. Economou, and C. M. Soukoulis. *Phys. Rev. Lett.*, 93:107402, 2004.
- [132] S. Zhang, Wenjun Fan, N. C. Panoiu, K. J. Malloy, R. M. Osgood, and S. R. J. Brueck. *Phys. Rev. Lett.*, 95:137404, 2005.
- [133] V. M. Shalaev. *Nature Photonics*, 1:41, 2006.
- [134] C. M. Soukoulis, S. Linden, and M. Wegener. *Science*, 315:47, 2007.
- [135] J. Valentine, S. Zhang, T. Zentgraf, E. Ulin-Avila, D. A. Genov, G. Bartal, and X. Zhang. *Nature*, 455:376, 2008.
- [136] M. Kafesaki, I. Tsiapa, N. Katsarakis, T. Koschny, and C. M. Soukoulis and E. N. Economou. *Phys. Rev. B*, 75:235114, 2007.

- [137] A. Mary, S. G. Rodrigo, F. J. García-Vidal, and L. Martín-Moreno. *Phys. Rev. Lett.*, 101:103902, 2008.
- [138] D. R. Smith, S. Schultz, P. Markos, and C. M. Soukoulis. *Phys. Rev. B*, 65:195104, 2002.